DESIGN OF LOW-LOSS ONE-POLE SYNCHRONOUS $LINBO_3$ SURFACE ACOUSTIC WAVE RESONATORS FOR SENSING APPLICATIONS

By Hsu-Cheng Ou

B.S. in Electrical Engineering, May 2000, Chang Gung University, Tao-Yuan, Taiwan
M.S. in Electrical and Computer Engineering, May 2004, The George Washington University

A Dissertation submitted to

The Faculty of
The School of Engineering and Applied Science
of The George Washington University
in partial satisfaction of the requirements
for the degree of Doctor of Science

August 31, 2010

Dissertation directed by

Mona E. Zaghloul
Professor of Engineering and Applied Science

The School of Engineering and Applied Science of The George Washington University certifies that Hsu-Cheng Ou has passed the Final Examination for the degree of Doctor of Philosophy as of April 20th, 2010. This is the final and approved form of the dissertation.

DESIGN OF LOW-LOSS ONE-POLE SYNCHRONOUS $LINBO_3$ SURFACE ACOUSTIC WAVE RESONATORS FOR SENSING APPLICATIONS

Hsu-Cheng Ou

Dissertation Research Committee:

Mona E. Zaghloul, Professor of Engineering and Applied Science, Dissertation Director

Can E. Korman, Professor of Engineering and Applied Science, Committee Member

Shahrokh Ahmadi, Professor of Engineering and Applied Science, Committee Member

David Nagel, Professor of Engineering and Applied Science, Committee Member

Jerry Wu, U.S. Patent and Trademark Office, Committee Member

Dedication

To my parents,

To my wife, Catherine Liu

I would like to thank you for all your supports, advices, and encourages.

Acknowledgement

The following groups and individuals were instrumental to this dissertation.

My research committees at the George Washington University: Prof. Mona E. Zaghloul (Advisor/Chairman), Prof. Can E. Korman, Prof. Shahrokh Ahmadi, Dr. David Nagel, and Dr. Jerry Wu;

Dr. Jerry Wu of the U.S. Patent and Trademark Office who provided expertise, insight, and inspiration throughout the years of classes and research;

Dr. David Nagel and Chia-pin Chang who provided expertise, insight, patience, and friendship;

John Abraham and Jon Hummel of University of Maryland, College Park who provided expertise, insight, and technical support;

James Griffin of the Howard University who provided expertise, insight, and technical support;

Irven Liu of the Formosa Plastic who provided inspiration, insight, and chemical-related materials;

the many colleagues of the MEMS lab of the George Washington University, Ritu Baipai, Chia-pin Chang, Tom Farmer, Mazdak Taghioskoui, Bowei Zheng, and etc who provided inspiration, insight, and encouragement;

and finally, but most importantly of all, my wonderful wife, Catherine Liu and my parents, who not only cheered me on, but provided ultimate safety net – their enthusiastic and unconditional love.

Abstract

DESIGN OF LOW-LOSS ONE-POLE SYNCHRONOUS LINBO3 SURFACE ACOUSTIC WAVE RESONATORS FOR SENSING APPLICATIONS

The surface acoustic wave (SAW) device has been used in many applications, such as using as resonators, to replace the inductance-capacitance (LC) filters, chemical or gas sensors. Our objectives in this work are to increase insertion loss (IL) and Q factor. The new improved device has applications in RF engineering as well as in sensors. They are used to sense the additional particles on the surface, which have a good potential for biological sensors.

In this work, a synchronous low-loss one-pole SAW resonator is designed to improve the existing SAW filter design. The mass-sensing applications of SAW resonators indicate the different potential for applications in biosensors. There are three objectives studied in this work. The first objective is to develop a low-loss and one-pole frequency response for SAW resonators. The insertion loss, which is the receiving power in the output transducer, is typically smaller than -6dB. Our goal is to achieve a low-loss response (>-3dB), and then it is necessary to improve the performance of SAW as a filter and as a biosensor. The bidirectional SAW resonator on the $LiNbO_3$ piezoelectric substrate have two-pole frequency response and low a Q factor. An improved frequency response with high Q factor is introduced in this work. The second objective in this research is to develop a SAW mass sensor on the $LiNbO_3$ substrate. When the additional mass is deposited on the surface, it results in a decrease in velocity and center frequency of acoustic waves. This decrease of the center frequency, or frequency shift, is linearly related to the additional mass. A frequency shift, due to the additional mass, can be observed by the low-loss and one-pole response in the output. This mechanism allows a

synchronous low-loss one-pole SAW resonator to have potential application in sensors; however, it is easier to determine the frequency shifts if the SAW resonator has a one-pole response in the output interdigital transducer (IDT). The mass sensitivity in this work is $8.23e^{12}$ $Hz \cdot mm^2/g$ for 978MHz SAW mass sensor. The third objective in this work is to use the SAW mass sensor operational in a liquid-phase environment for mass detection. The acoustic waves are excited by conductive electrodes on the piezoelectric surface; the signal on these electrodes becomes shorted when the SAW device is in liquid. In order to protect the electrodes, a polymer coating is applied to the surface in order to avoid the short circuit. This polymer-coated SAW mass sensor makes it possible to sense antibody-antigen reactions in liquid.

Table of Contents

Dedication ..... **iii**

Acknowledgement ..... **iv**

Abstract ..... **v**

Table of Contents ..... **vii**

List of Figures ..... **x**

List of Tables ..... **xviii**

Chapter 1 - Introduction **1**

1.1. Motivation 1

1.2. Research Objectives 1

1.3. Outline 4

Chapter 2 - Technical Background and Literature Review **6**

2.1. The Development of Surface Acoustic Wave (SAW) Devices 6

2.2. Applications of SAW Devices 7

2.3. Using SAW Devices as Sensors 11

Chapter 3 - Modeling and Analysis of SAW Resonators on the 128^{o} YX $LiNbO_3$ Substrate **14**

3.1. Analytic Models for a Single-Phase Bidirectional SAW Resonator 18

3.1.1. Geometry of Bidirectional SAW Resonator 19

3.1.2. The Crossed-Field Model of Bidirectional Devices 21

3.1.3. The Equivalent Circuit and Insertion Loss 25

3.1.4. The S_{21} Simulation in MATLAB 27

3.2. The Properties of the 128^{o} YX $LiNbO_3$ 29

3.2.1. Characteristics of SAW and Leaky-SAW (LSAW) Devices 29

3.2.2. Electromechanical Coupling Coefficient K^2 and Velocity..... 30

3.2.3. Temperature Coefficient 33

3.3. Proposed One-Pole Synchronous SAW Resonators..... 34

3.3.1. Geometry of the One-Pole Synchronous SAW Resonator with Shorted Reflectors 34

3.3.2. The Y Admittance and IL Modeling for the Proposed One-Pole Synchronous SAW Resonators 37

3.3.3. The S_{21} and Maximum IL in MATLAB Simulations of the Proposed One-Pole Synchronous SAW Resonators..... 40

3.3.4..... 40

3.4. Simulation of One-Pole Synchronous SAW Resonators by Using the Finite Element Method to Analyze 41

3.4.1. The Simulations of LiNbO3 Crystal Structures in COMSOL 42

3.4.2. The FEM Simulations of Acoustic Waves in Coventorware 44

Chapter 4 - Fabrications and Measurement of One-Pole Synchronous SAW Resonators……51

4.1. Microfabrication Processes on the Piezoelectric Wafers 52

4.2. S_{21} Measurement of 121MHz and 978MHz Resonators 59

Chapter 5 - The Application of One-Pole Synchronous SAW Resonators for Mass Sensors……..68

5.1. The Structure of One-pole Synchronous SAW Mass Sensors 69

5.2. The Velocity and Frequency Shifts of Mass Sensors..... 73

5.3. Simulation of the Mass on the Surface 80

5.4. The Measurement of Frequency Shifts and Mass Sensitivities 82

Chapter 6 - Polymer-coated SAW Mass Sensors for the Liquid-phase Environment……90

6.1. The Synthesis of the Polyvinyl Chloride Layer 92

6.2. The Velocity and Frequency shifts 95

6.3. Experimental Results 97

Chapter 7 - Conclusion and Future Research Opportunity 101

7.1. Conclusion 101

7.2. Future Research Opportunity 103

References 106

List of Figures

Figure 1: Research Topology including of simulations, fabrications and measurements. 4

Figure 2: Example of SAW RF and IF filter in the block diagram of a GSM transceiver. 9

Figure 3: Example of SAW RF and IF filter in the block diagram of a wireless receiver. 9

Figure 4: Example of SAW convolver in the block diagram of a spread spectrum system. 10

Figure 5: The biocoating configuration on the two-port SAW resonator. 10

Figure 6: The recent IEEE journals on SAW devices from 2000 to 2010. There are 1762 papers in the bioengineering field. 13

Figure 7: The structure and distance parameters of bidirectional SAW filter 14

Figure 8: The structure and distance parameters of the one-pole loss synchronous SAW resonator 16

Figure 9: The propagation of Rayleigh waves on the piezoelectric surface. Different Harmonic Frequencies will be excited between the electrodes. 17

Figure 10: The frequency response of two harmonic frequencies on the 128^0 Y-Z rotated $LiNbO_3$ Substrate. 18

Figure 11: Elementary structures and distance parameters of the single-track and dual-track bidirectional SAW resonator. It has the uniform IDTs in the input and output. 20

Figure 12: Matrix blocks of bidirectional SAW resonators. The IDT can be translated into a three-port network. Port 3 is electrical port. Port 1 and Port 2 are acoustic ports. The acoustic waves excited from port 2 propagate away from output IDT. These escaped acoustic waves in port 2 cause the power loss to the output IDT. 21

Figure 13: Three-port equivalent Y admittance network of IDT. G_o is the equivalent electrical conductance and C_T is the total capacitance of electrodes. 22

Figure 14: The three-port network of input/output IDTs. V_a and V_b are electrical port of input and output respectively which can be translate into a two-port equivalent circuit. 24

Figure 15: The equivalent circuit for a bidirectional SAW resonator. The three-port networks of input and output IDTs are translated into two port circuit. R_s and R_L are source and load resistances. The current source which is proportional to the amplitude excites the output IDT..... 26

Figure 16: The MATLAB simulation of the bidirectional SAW resonators on the LiNbO3 substrate. The maximum insertion loss of S21 response is -14.3124 dB in 121MHz when the finger pairs in the input and output IDT are 30..... 28

Figure 17: The pattern of acoustic waves on the free space of SAW and LSAW devices. (a) Surface acoustic waves (Rayleigh waves) (b) Rayleigh waves and bulk waves in the LSAW devices. 30

Figure 18: The maximum insertion loss of bidirectional SAW resonators versus finger pairs. According to the equivalent circuit in the previous section, the insertion loss is relative to the finger pairs in the input and output IDTs. The high K^2 material, like $LiNbO_3$, has higher insertion loss in comparison with the low K^2 material. 32

Figure 19 The maximum insertion loss of bidirectional SAW resonators on the 128° YX $LiNbO_3$ substrates. 33

Figure 20: The Single-Track and Dual-Track SAW resonators with synchronously shorted Reflectors. The reflecting acoustic waves results in an asymmetric resonance with ±90° phase shift superimposed in the center frequency. 36

Figure 21: The ratio of power reflection from the electrodes of reflectors on the 128° YX $LiNbO_3$ and ST Quartz. The metallization η is 0.5. The power reflected by 10 electrodes on the YX $LiNbO_3$ is equal to the same power reflected by 100 electrodes on ST Quartz [34][35]. 37

Figure 22: Matrix blocks of a two-port one-pole SAW resonator. There are two transitions of acoustic waves propagating to the output IDT. The first transition of acoustic waves propagates to the output IDT directly. The second transition of acoustic waves are the reflecting waves in the output IDT reflected by reflectors. ... 38

Figure 23: The MABLAB simulation of SAW resonator with shorted reflectors symmetrically placed after input and output IDTs. An asymmetric resonance is superimposed in the center frequency. The maximum insertion loss is -4.86dB in 121 MHz, which is higher than the bidirectional SAW resonator. 41

Figure 24: The cross view of the $LiNbO_3$ crystal structures. The crystal structure is disturbed by the surface acoustic waves. 43

Figure 25: The transit simulation in Coventorware. The acoustic waves propagate gradually from input IDT to output IDT. (a) T = 3.1 e^{-8} s (b) T = 3.5 e^{-8} s (c) T = 3.9 e^{-8} s 45

Figure 26: The maximum displacement of the 121MHz resonator increases gradually in the transit simulation. 46

Figure 27: (a)(b)The 3D model of single-track and dual-track bidirectional SAW filters. The acoustic waves propagate between input and output IDTs. 48

Figure 28: The mash model and 3D model of the Single-Track and Dual-Track SAW resonators with synchronously shorted Reflectors: (a) The Single-Track SAW resonator (b) the Dual-Track SAW resonator. The magnitudes of displacements are shown in different colors. 48

Figure 29: The displacement in Z axis of the SAW resonator with shorted reflectors. The maximum displacement occurred in the center frequency. 49

Figure 30: The maximum displacement in the Z axis versus finger pairs in Coventorware simulation. 50

Figure 31: The processes of micro fabrication on the 4" 128^{o} YX $LiNbO_3$ wafer. The cross view of wafers are illustrated. 54

Figure 32: The layout of SAW resonators in Cadence. Different sizes of SAW resonators are designed on the 4" wafer. 56

Figure 33: (a) The 5" Mask for the Lithography of 4" wafers. (b) The SAW structures on the 4" 128^{0} YX-$LiNbO_3$ wafer. 56

Figure 34: SEM of the IDTs and reflectors on the 128^{0} YX-$LiNbO_3$ wafer. The width of electrodes is 8μm which yield a center frequency of up to 121MHz (a) Input/output IDTs with shorted reflectors (b) The minimum distance between the IDT and reflector. (c) The width of electrodes. The metallization is equal to 50%. 58

Figure 35: (a)(b)A one-pole synchronous SAW resonator with SMA connectors in the shield box. 59

Figure 36: (a) RF Microwave Probe. (b) Calibrations for Network Analyzer through RF Microwave Probe. (c) Micro Tech Probe Station 61

Figure 37: Measurement setup and calibration. The parasitic effects between the probe pads and network analyzer can be calibrated by the through circuit. The device under test (DUT) is a SAW resonator connecting to the probe pads. 62

Figure 38: The layout of probe pads for the "through" calibration. The distance between input and output pads is the same as the calibration pads. 62

Figure 39: Direct measurement of SAW filters on the $LiNbO_3$. It shows the connections between the probe station and network analyzer. The ground-signal-ground (GSG) probe tips connect to the metal pads directly. 64

Figure 40: Probe tips on the $LiNbO_3$ wafer. 65

Figure 41: Frequency response of 121MHz SAW resonators. The single-track SAW resonator without shorted reflectors has a two-pole response. With shorted reflectors included, a one-pole resonance with 90^o phase shift is superimposed in the center frequency..... 66

Figure 42: Frequency response of 978MHz SAW resonators. The dual-track SAW resonator has -2.8 dB insertion loss. The dual-track IDT with shorted reflectors has a better stop band rejection than the single-track IDT..... 67

Figure 43: (a) The geometry of single-track and dual -track SAW resonators. The synchronous shorted reflection gratings are placed $1/2\lambda$ out from the IDTs

symmetrically. The sensing area includes input /output IDTs and reflectors. (b) Sensing Area and metalized region of the SAW mass sensor. 71
Figure 44: The configuration and measurement of mass sensors. The sensing area covers the input /output IDTs and reflectors..... 72
Figure 45: Material properties of Potassium Chloride (KCL). 72
Figure 46: The frequency shift versus different thickness of the mass on the electrodes. Base on Equation 26, the frequency shifts are linear to the thickness of mass approximately when the film-thickness ratio h/λ is less than 0.01. (a) 122MHz SAW mass sensor (b) 978MHz SAW mass sensor 79
Figure 47: The 3D model of the SAW resonator in Coventorware . The displacements are shown when the acoustic waves propagate from input IDT to output IDT. The center frequency f_o changes with the different thicknesses of KCL (h_{KCL}). 81
Figure 48: The Coventorware simulation of frequency shifts when the different thicknesses of KCL are deposited on the surface. It shows the linear region when the thickness of KCL is less than 0.3μm. 82
Figure 49: The measurement setup include the heating plate and fan. The heating plate and fan are used to keep temperature stable. The temperature is monitored by the IR thermometer. 84
Figure 50: The 121 MHz center frequency of the dual-track SAW resonator shifts due to the KCL film on the electrodes. The center frequency decreases when the additional mass of KCL film is deposited..... 85
Figure 51: The frequency shifts versus the mass densities of the KCL films. According to the results of Aglient 8722D Network Analyzer, the mass sensitivities

are 1.315×10^{11} Hz·mm^2/g and 8.23×10^{12} Hz·mm^2/g for 121MHz and 978 MHz SAW resonators respectively. 86

Figure 52: The illustration of a SAW mass sensor covered by a plastic well. The radius of sensing area is 3.4mm. 87

Figure 53: (a) the dual-track one-pole synchronous SAW sensor. The sensing area of the 121 MHz SAW resonator is 1.6 mm x 2.0 mm and the sensing area of the 978 MHz SAW resonator is 0.4 mm x 0.2 mm. (b) Its input and output IDTs have 12 finger pairs (N=12). The length of apertures is equal to 50λ. (c) The KCL drops on the sensing area. The plastic well is used to define the sensing area, which has a radius of 1.7mm. (d) The KCL film (mass density=9.73ng/mm^2) remained on the surface when the solvent is evaporated. 88

Figure 54: The configuration of the SAW mass sensor and measurement. The plastic well is placed on the mass sensor to define the sensing area. The portable SAW mass sensor is on the microscope slide and connected to Network Analyzer by the sensor housing. 92

Figure 55: the THF solvent and PVC solution. The concentration of PVC solution is 1g/L. 94

Figure 56: The PVC layer under Microscope. PVC polymer layer can be synthesized in few seconds, after THF is evaporated. It shows smooth and uniform surface under microscope. 95

Figure 57: The polymer-coated SAW mass sensor and sensor housing device. 98

Figure 58: The 3/16” plastic well on the 121MHz SAW mass sensor. The 18ul KCL solution is dropped into the well and covered with the whole sensor. The KCL remains on the surface of the polymer layer after the solvent evaporates. 99
Figure 59: The mass sensitivity of SAW Mass Sensors. The 121MHz polymer-coated SAW mass sensor has slightly less sensitivity than the SAW mass sensor. 100
Figure 60: The illustration of the antibody-antigen reactions on the polymer-coated SAW mass sensor. The polymer layer can prevent the short circuit of electrodes in the liquid-phase environment. The antibodies are attached on the surface of polymer to catch the antigen. 105

List of Tables

Table 1: The applications of SAW devices for wireless communication 8

Table 2: The properties of common piezoelectric substrates for SAW resonators. 128^{o} YX LiNbO3 has a high electromechanical coupling coefficient K2 and acoustic velocity. 31

Table 3: The matrixes of the stiffness and piezoelectric strain of 128^{o} YX $LiNbO_3$. They define the properties of 128^{o} YX $LiNbO_3$ in COMSOL and CoventorWare Simulations [1][2]. 43

Table 4: The depositing and etching processes in Coventorware 44

Table 5: The recipes of processes in the microfabrication 55

Table 6: The temperature sensitivity of $LiNbO_3$ substrate 55

Table 7: The parameters of piezoelectric substrates based on the 50% Aluminum metallization and shorted reflectors. h is the thickness of electrodes and λ is the wavelength of acoustic waves. 80

Table 8: Theoretical Calculation of Mass Sensitivities (Smf) of 121MHz and 978MHz SAW mass sensors. 80

Table 9: The mass density versus frequency of 121M Hz SAW mass sensors 84

Table 10: The properties of Polyvinyl Chloride (PVC) and Tetrahydrofuran (THF). 93

Table 11: The frequency shifts when 20 pg/mm^2 mass is on the electrodes. The smaller width of electrodes yields to the higher frequency shift and mass sensitivity. 104

Chapter 1 - Introduction

In this work, a synchronous low-loss one-pole surface acoustic wave (SAW) resonator is designed to improve the existing SAW filter design. The mass-sensing applications of SAW resonators indicate the different potential for applications in biosensors. In this chapter, the research objectives and approaches are discussed. The detailed steps, including simulations, fabrications and measurements are presented in the following chapters.

1.1. Motivation

The SAW device [1]-[15] has been used in many applications, such as using as resonators, to replace the inductance-capacitance (LC) filters, chemical or gas sensors. Its operating frequencies depend on the width of electrodes, however the low insertion loss (<-6dB) of common existing SAW filter [4]-[6] designs limits them to being suitable only as RF or narrowband filters. Our objectives in this work are to increase insertion loss (IL) and Q factor. The new improved device has applications in RF engineering as well as in sensors. They are used to sense the additional particles on the surface, which have a good potential for biological sensors.

1.2. Research Objectives

There are three objectives of this research: (1) to develop a synchronous low-loss one-pole SAW resonator [23][24]; (2) to use the SAW resonator as a mass sensor to

sense the additional mass on the dry surface; (3) to improve the SAW mass sensor in the liquid by coating the surface with polymer. The first objective is to develop a low-loss and one-pole frequency response for SAW resonators. The insertion loss, which is the receiving power in the output transducer, is typically smaller than -6dB. Our goal is to achieve a low-loss response (>-3dB), and then it is necessary to improve the performance of SAW as a filter and as a biosensor. The bidirectional SAW resonator [1][15] on the $LiNbO_3$ piezoelectric substrate have two-pole frequency response and low a Q factor. An improved frequency response with high Q factor is introduced in this work.

The second objective in this research is to develop a SAW mass sensor [39]-[43] on the $LiNbO_3$ substrate. When the additional mass is deposited on the surface, it results in a decrease in velocity and center frequency of acoustic waves. This decrease of the center frequency, or frequency shift, is linearly related to the additional mass. A frequency shift, due to the additional mass, can be observed by the low-loss and one-pole response in the output. This mechanism allows a synchronous low-loss one-pole SAW resonator to have potential application in sensors; however, it is easier to determine the frequency shifts if the SAW resonator has a one-pole response in the output interdigital transducer (IDT) [15]. The mass sensitivity in this work is $8.23e^{12}$ Hz·mm^2/g for 978MHz SAW mass sensor.

The third objective in this work is to use the SAW mass sensor operational in a liquid-phase environment for mass detection. The acoustic waves are excited by conductive electrodes on the piezoelectric surface; the signal on these electrodes becomes shorted when the SAW device is in liquid. In order to protect the electrodes, a polymer coating is applied to the surface in order to avoid the short circuit. This polymer-coated

SAW mass sensor makes it possible to sense antibody-antigen reactions in liquid. To achieve these objectives, the following steps are taken as major contributions:

1. Develop an equivalent circuit and insertion loss by using sinc functions and cross-field model, which are simulated in MATLAB.
2. Simulate an accurate frequency response, 3D model, frequency shift by using Finite Element Method (FEM).
3. Optimize the insertion loss by the number of electrodes and the aperture's length.
4. Fabricate various sizes of SAW resonators on the $LiNbO_3$ substrate by MEMS microfabrication processes in the clean room.
5. Perform the repeat high-frequency measurements on the wafers and chips to prove the concepts of this research.

The research topology is shown in Fig.1 including the simulations, fabrications and measurements. The simulation results are compared with the experiment results to verify the concepts. For SAW mass sensors, the same measurements were performed at least five times on the different chips. These repeat measurements prove that the concept of this work is reproducible and valid.

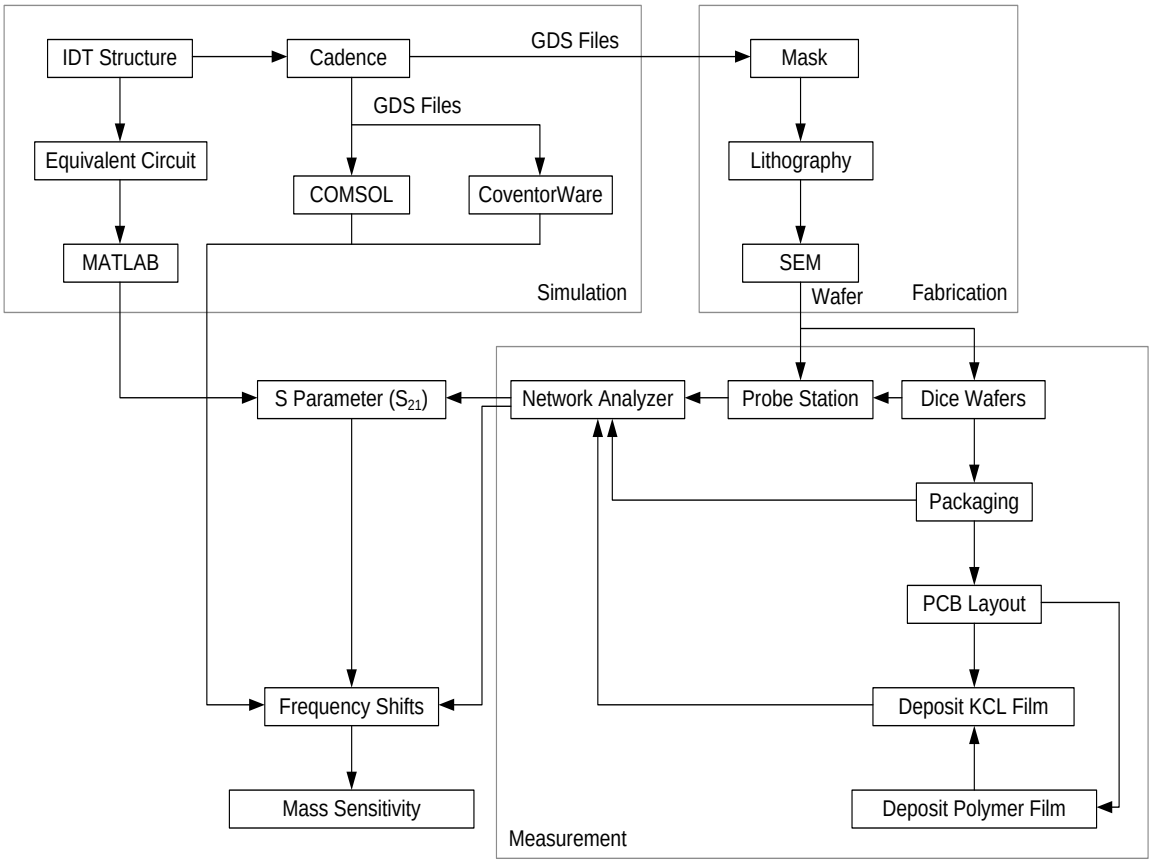

Figure 1: Research Topology including of simulations, fabrications and measurements.

1.3. Outline

The details of this work are discussed in chapters that follow. Chapter 2 includes the technical background, development and application of SAW devices. It also shows that much of the researches on SAW devices have been in the bioengineering field in recent years. The SAW device has had an important role in sensing applications in recent years.

Chapter 3 demonstrates the one-pole synchronous SAW resonators on the $LiNbO_3$ substrate, which are compared with single-phase bidirectional SAW resonators [1][23][24]. The bidirectional resonator is a conventional design of the SAW resonator,

which has a small insertion loss and Q factor. The proposed one-pole synchronous SAW resonator has a different structure, which can reduce the propagating loss and increase the insertion loss. These two resonators are simulated by FEM to verify the propagation of acoustic waves and their harmonic frequency on the surface.

Chapter 4 presents the fabrication processes to define SAW resonators on the $LiNbO_3$ wafer. The accurate measurements were made directly on the wafers and through the SMA connectors. According to the experimental results, the synchronous one-pole resonator has larger IL than the bidirectional resonator.

Chapter 5 shows how the one-pole synchronous SAW mass sensors detect the potassium chloride (KCL) thin film on the surface. The KCL thin film is additional mass, which decreases the velocity and center frequency of acoustic waves. The shift of the center frequency is proportional to the total additional mass on the surface. Based on the results, the SAW mass sensor has good linearity and high sensitivity for sensing applications.

Chapter 6 shows the mass sensitivity of the polymer-coated SAW mass sensor in the liquid-phase environment. It has slightly less sensitivity than the SAW mass sensor in the previous chapter, due to the polymer, however the polymer-coated SAW mass sensor can sense biological samples in liquid. Chapter 7 is the summary and conclusion of this work.

Chapter 2 - Technical Background and Literature Review

The development of SAW filters researched a limitation in 1980 due to the low insertion loss. Recent research has focused on developing low-loss SAW devices and the uses of SAW devices as sensors in the bioengineering field. In this chapter, the development and applications of SAW devices is reviewed. Furthermore, the recent research and development for using SAW sensors in the bioengineering field are also investigated.

2.1. The Development of Surface Acoustic Wave (SAW) Devices

SAW devices were applied to the design of analog electrical filters and used to substitute the inductance-capacitance (LC) filters in high-volume TV components in the early stage[1]. They have very competitive performance and price for intermediate-frequency (IF) circuit stages. Their operating frequency is in the range of 10MHz to 1GHz. There was intensive research done early on, due to their wide range of applications, however, the SAW technology reached the limit of its low insertion loss (IL)[1]. The IL of the existing SAW filter design is smaller than -6dB, which limits the utilization in the IF stages. For the receivers stage in telecommunications, the IF stages, which operate in millivolt signals, can tolerate the high loss of SAW filters. The RF filter circuits, which circuits which only have microvolt-level inputs, cannot use SAW filters due to the limitations of the signal-to-noise ratio and IL. In recent research, low-loss SAW (>-3dB) filters were made possible by the discovery of different piezoelectric

substrates or crystal cuts. There are wider applications of low-loss SAW filters in RF front-end filters and antenna duplexers in communications.

2.2. Applications of SAW Devices

The research and developments of SAW devices is related in the following three fields: (1) the geometry of the metal-film interdigital transducers (IDTs) (2) piezoelectric substrate, and (3) the wave propagation type. The IL and frequency response characteristics can also be improved from these three factors. In general, the various SAW devices for the communication systems can be categorized into the four types shown in Table 1[1]. The frequencies for mobile and wireless applications are ranged from 800MHz to 2.4GHz. The block diagram of the receiver and transmitter using SAW filters is shown in Figure 2 and Figure 3 [1][8][9][10][11]. The SAW filters are used in IF and RF stages in wireless communications. Figure 4 shows an application for convolvers by using three-port SAW devices [1]. The last example, in Figure 5, is a SAW sensor which has a biological layer in the transmission line.

Bidirectional IDTs • The delay lines for oscillators or equalizers • PN-coded trapped-delay line for CDMA-TDMA systems • Delay lines to reduce the multipath interference • Fixed frequency reference oscillators • VCOs for first- or second-mixing stages in mobile transceivers • Intermediate frequency (IF) filters for mobile receivers • Nyquist filters
Resonator/Filters • Fixed frequency and tunable oscillators • Resonators for transmitter circuits • RF front-end filters for mobile systems • RF front-end filters for wireless receivers • High-power antenna duplexers
Unidirectional IDTs • Low-loss IF filter for wireless circuits (>-3dB) • RF front-end filters for wireless communications • Multimode oscillators for spread-spectrum communications
Nonlinear Operation • Convolvers for spread-spectrum communications

Table 1: The applications of SAW devices for wireless communication

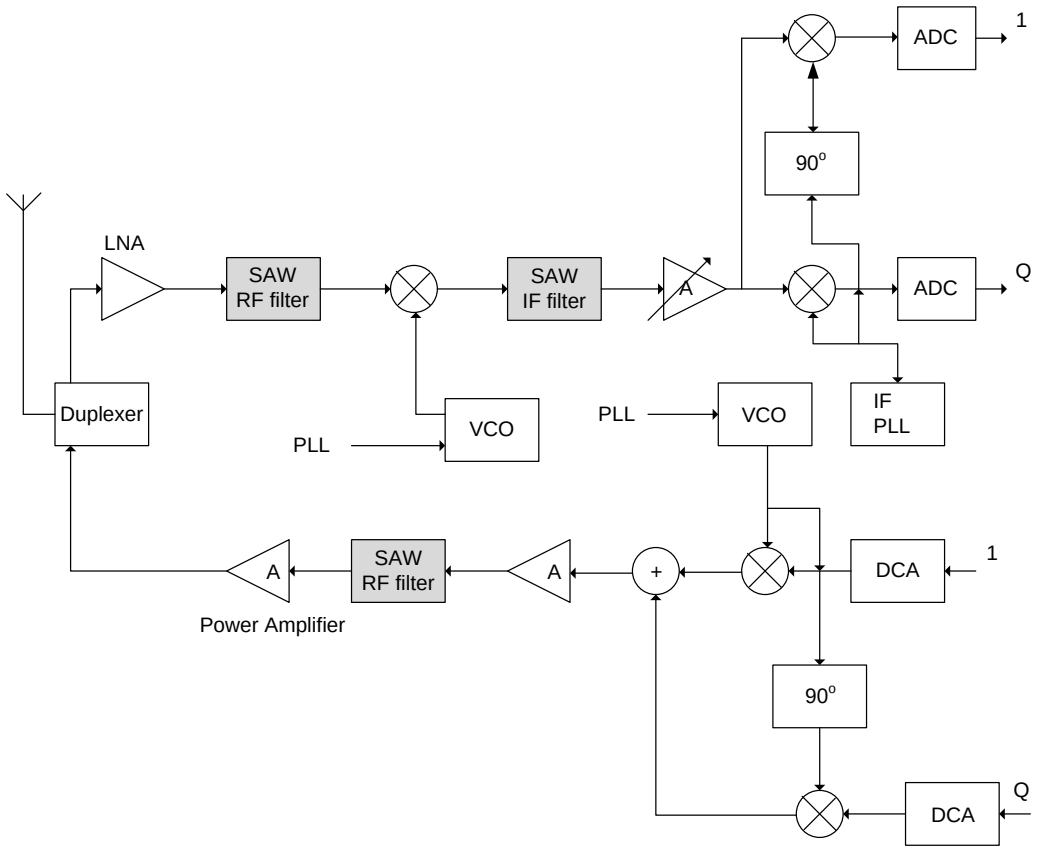

Figure 2: Example of SAW RF and IF filter in the block diagram of a GSM transceiver.

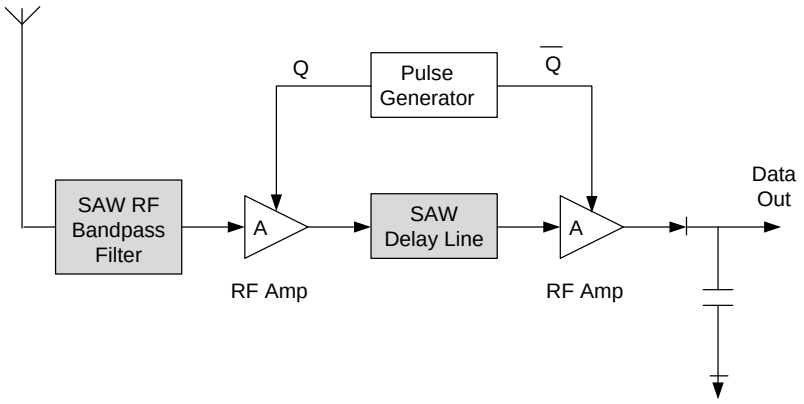

Figure 3: Example of SAW RF and IF filter in the block diagram of a wireless receiver.

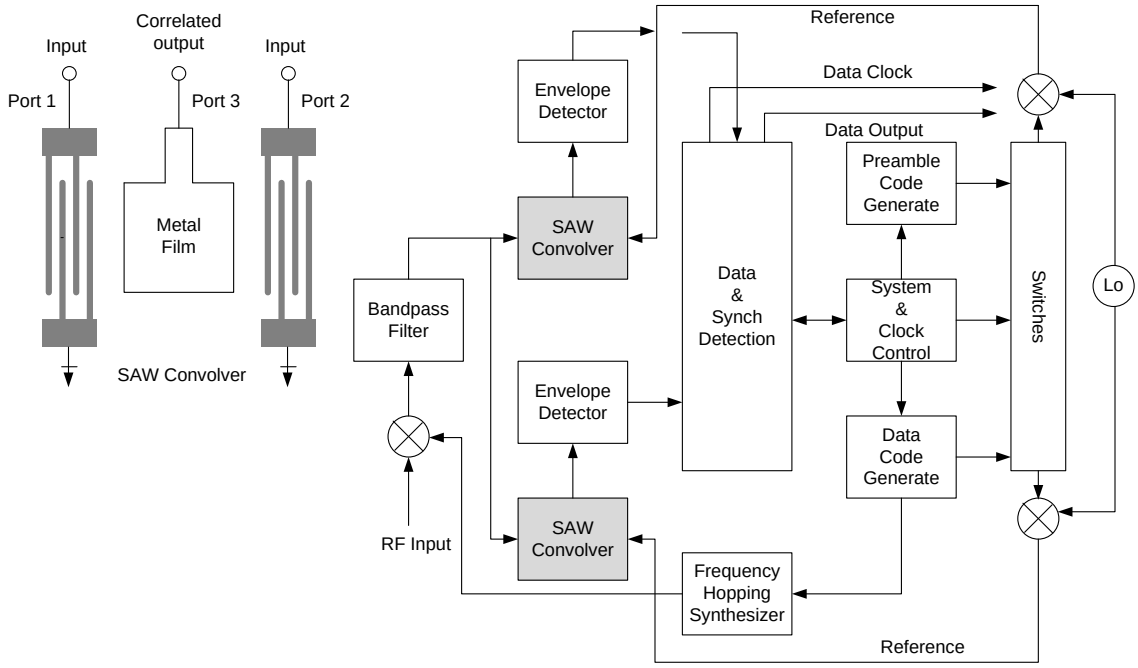

Figure 4: Example of SAW convolver in the block diagram of a spread spectrum system.

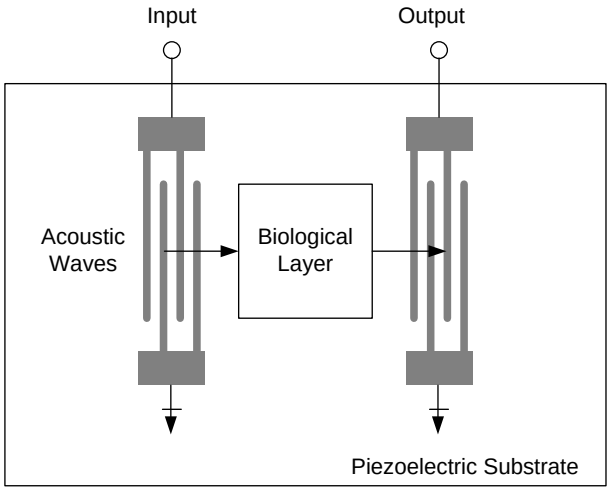

Figure 5: The biocoating configuration on the two-port SAW resonator.

2.3. Using SAW Devices as Sensors

In recent years, there has been much research in using surface acoustic wave device as sensors. The applications of SAW devices include chemical, thermal, pressure or biological areas. These devices sense differences by the interferences of acoustic waves on the piezoelectric surface. These interferences are from the change of total mass on the surface or the path of the transmission line. They cause a decrease in the velocity, center frequency or amplitude of acoustic waves. The time of acoustic waves' propagation between input and output transducers is also increased by these interferences. These changes can be sensed by the decrease of the center frequency, propagation loss or the increase of propagating time in the output transducer. A common design for a SAW sensor is shown in Figure 5. The metal layer is deposited between input and output IDT to catch the particles and change the acoustic waves. The electrical signals which are collected in the output IDT are different than the signals without particles in this metal layer.

The attention has been drawn in recent years to the use of SAW in microfluidic devices. The acoustic waves are mechanic waves, which have motions in the Z direction on the surface. These surface motions typically have approximate 10 Å displacements and allow the SAW devices to be used as microactuators. The acoustic waves can propagate into the fluid and become an inertial force. This mechanism to drive fluid actions allows the possibility for the SAW devices being used in pumping, mixing or jetting devices of microfluidic devices.

Figure 6 shows the number of articles related to SAW devices published in IEEE journals in past ten years (2000-2010). The most popular area of research relate to use

SAW devices as components or devices in circuits. Research in this are focuses on optimizing the insertion loss, Q factors or oscillations for communication systems. There is, however, a great deal of research on the use of SAW devices as sensors or actuators in the bioengineering field, that shows that SAW devices are stable, low-cost and sensitive devices for sensing applications. A well-known commercial application of SAW sensors is the touch screen display. Other area of research aim to investigate the behavior of acoustic waves, propagations or different piezoelectric materials.

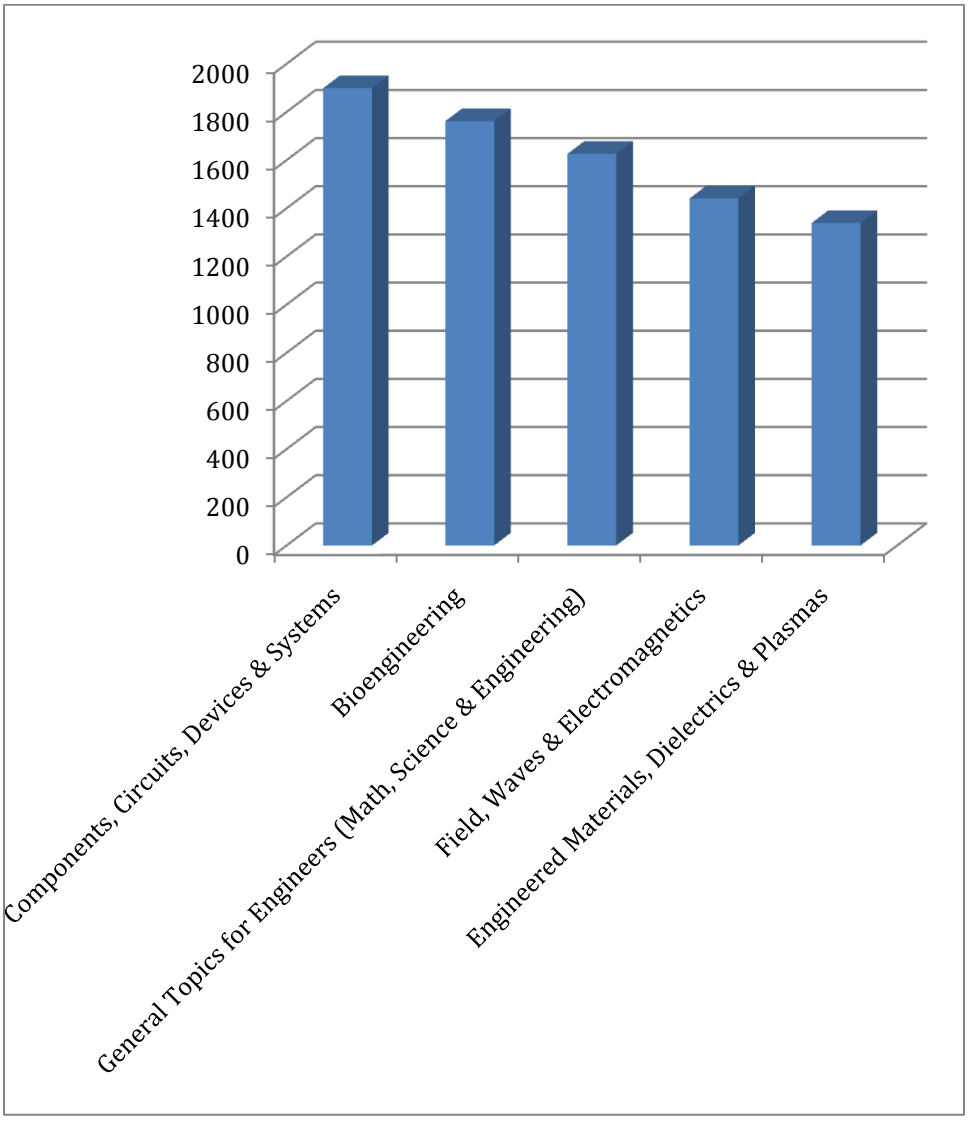

Figure 6: The recent IEEE journals on SAW devices from 2000 to 2010. There are 1762 papers in the bioengineering field.

Chapter 3 - Modeling and Analysis of SAW Resonators on the 128° YX $LiNbO_3$ Substrate

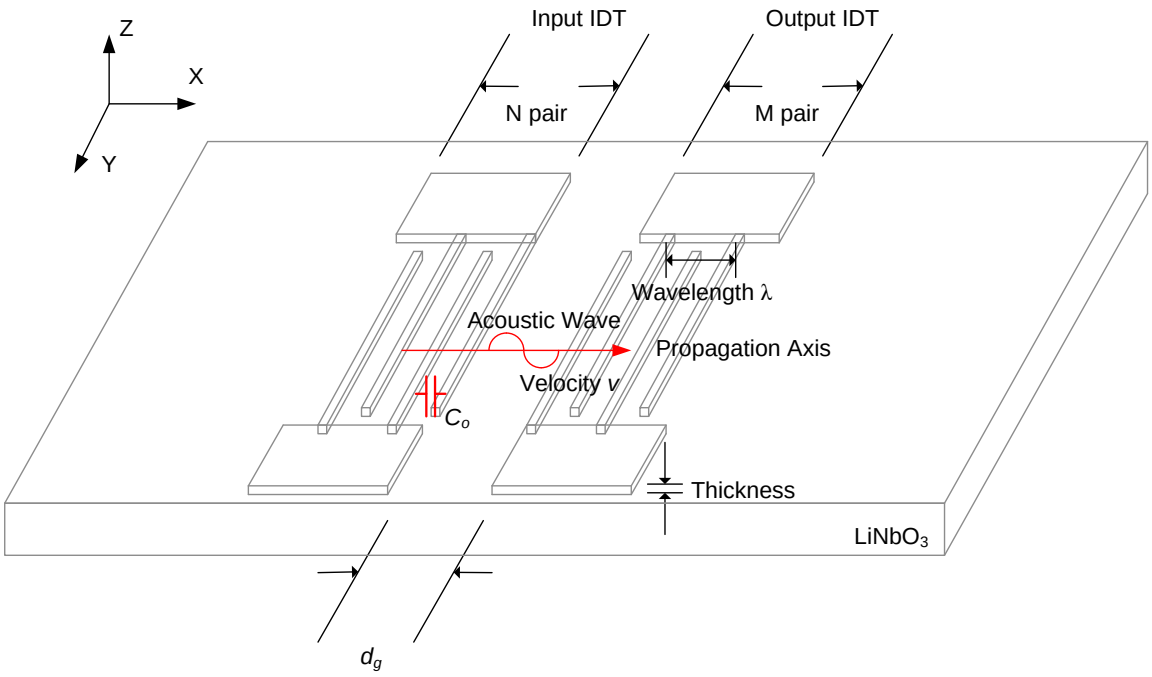

Figure 7: The structure and distance parameters of bidirectional SAW filter

In order to understand the characteristic of the SAW device on the 128° YX $LiNbO_3$ substrate, it is necessary to develop a model that can convert the energy between electric signals to mechanic waves. According to the literature review in the previous chapter, there were three common circuit-response models developed: the Delta-function model, the Crossed-field model and the Impulse-response model [1][16][17][18]. The Delta-function model uses a digital sampled-data structure to simulate an approximate frequency response of interdigital transducers (IDT). It is a fast tool, but not able to give information on impedance and insertion-loss. The Crossed-field model [1], also known as the Mason model, can obtain the radiation conductance parameters in the transmission of SAW. This yields information on the frequency response and insertion loss, including

input and output impedances. The Impulse-response [1][18] model includes the circuit impedance and yields additional information than the Delta-function model[1]. It uses Fourier transform to determine the frequency response *H(f)* of the SAW devices.

In this work, the Crossed-field model is employed for modeling SAW resonators on the 128^o YX $LiNbO_3$ substrate. The Crossed-field model yields the better agreement in the frequency response for the IDTs on the high-K^2 piezoelectric substrates. The 128^o YX $LiNbO_3$ is a piezoelectric material, which has high K^2 and velocity and thus, the Crossed-field model is used.

In this work, we used 128^o YX $LiNbO_3$ as the substrate because the coupling between the electrical and mechanical energy is the highest in Table 2. Figure 7 indicates the traditional SAW structures. In the practical design of SAW resonators, there are many factors affecting the performance. The most important parameters in SAW resonators are summarized as the following: (1) the space d_g between the adjacent IDT; (2) the space d_r between the IDT and reflector; (3) reflectivity and loss; (4) separation between IDTs and reflectors; (5) the number of IDT fingers; (6) IDT thickness and resistivity; (7) electromechanical coupling constant K^2 and the capacitance C_o value of finger pair; and (8) the operating frequency f_o. These important parameters are also investigated in the following sections.

In Figure 7, the acoustic waves are analyzed and simulated by using the Crossed-field model. The bidirectional SAW resonators are the basic structures which cause a large loss in escaped acoustic waves. In order to increase the energy transferring to the output, the reflectors are designed and placed outside of input/output IDTs as shown in Figure 8. The acoustic waves are trapped between the input and output IDTs due to the reflectors,

which results in a one-pole low-loss frequency response at the receiving IDTs. Figure 20 shows the reflection of the wave with 90^{o} phase shift which enhance the acoustic energy and create the one-pole low-loss response.

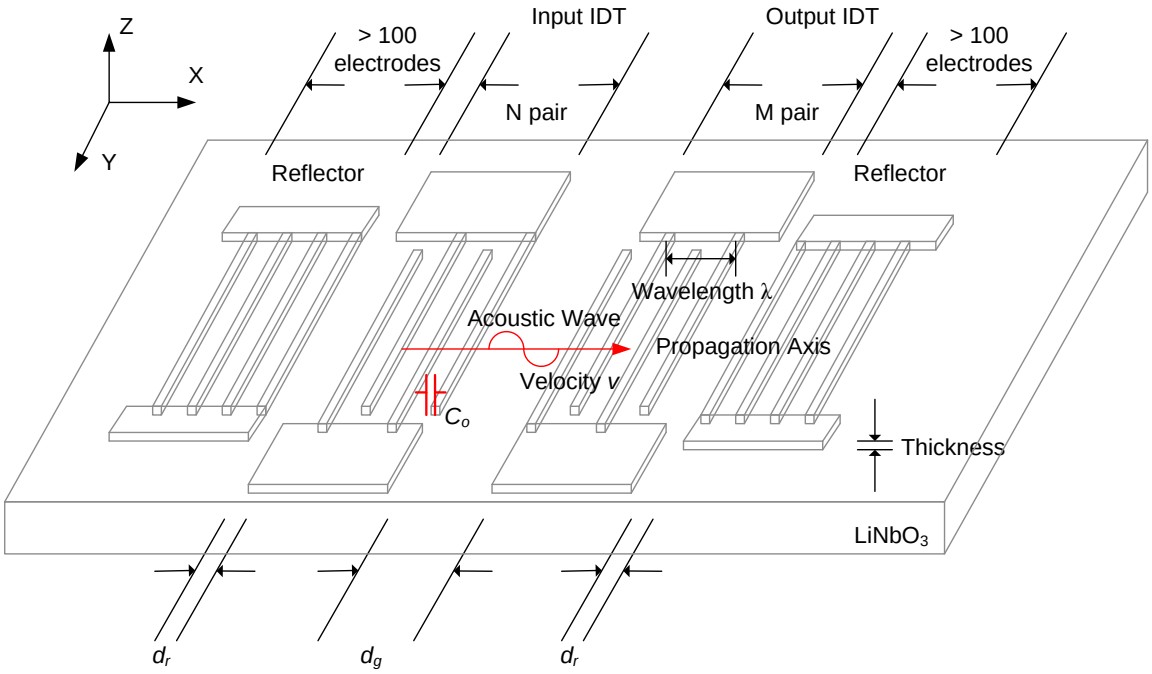

Figure 8: The structure and distance parameters of the one-pole loss synchronous SAW resonator

Figure 9 shows that the acoustic waves are excited by applying voltage on the electrodes. These acoustic waves cause displacement and a potential difference on the surface of piezoelectric material. The frequency of acoustic waves is governed by the periodic electrodes of IDT and the acoustic velocity of the piezoelectric material. The equation for velocity is shown in Equation 1.

$$v = \lambda_1 \times f_1 \qquad \text{Equation 1}$$

,where λ_1 is the wavelength in the first harmonic frequency and $f_1$is the center frequency.

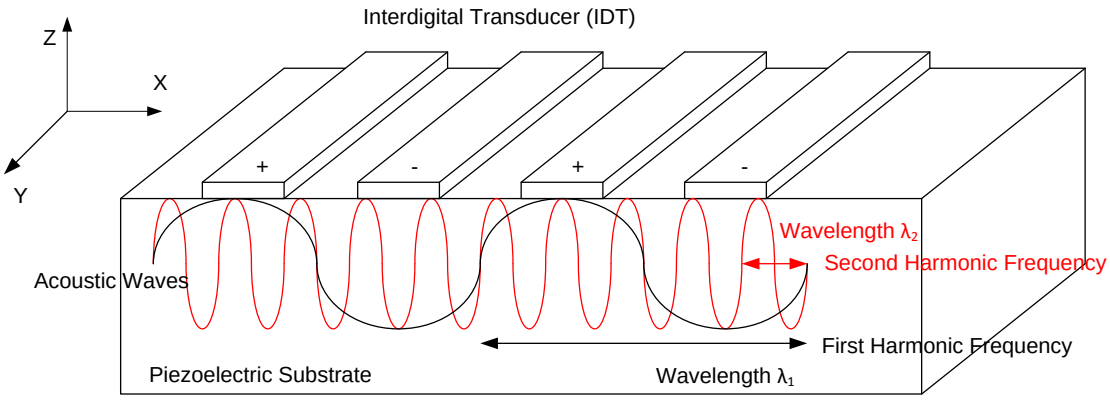

Figure 9: The propagation of Rayleigh waves on the piezoelectric surface. Different Harmonic Frequencies will be excited between the electrodes.

In Figure 9, there is more than one harmonic wave propagating along the surface between the electrodes. The wavelength of the *n* harmonic frequency is defined in terms of λ_1 in Equation 2. Figure 10 shows the first f_1 and second f_2 harmonic frequency for SAW structures shown in Figure.

For the second harmonic wavelength λ_2,

$$\frac{1}{4}\lambda_1 = \frac{1}{4}\lambda_2 + \lambda_2 \qquad \text{Equation 2}$$

For the n harmonic wave length λ_n,

$$\frac{1}{4}\lambda_1 = (n-1)\lambda_n + \frac{1}{4}\lambda_n$$

$$\lambda_n = \frac{1}{(4n-3)}\lambda_1 \qquad \text{Equation 3}$$

$$f_n = (4n-3)f_1, n > 2 \qquad \text{Equation 4}$$

, where

λ_2 The wavelength of the second harmonic frequency

f_2 The frequency of the second harmonic frequency

λ_n The wavelength of *n* harmonic frequency

f_n The frequency of *n* harmonic frequency

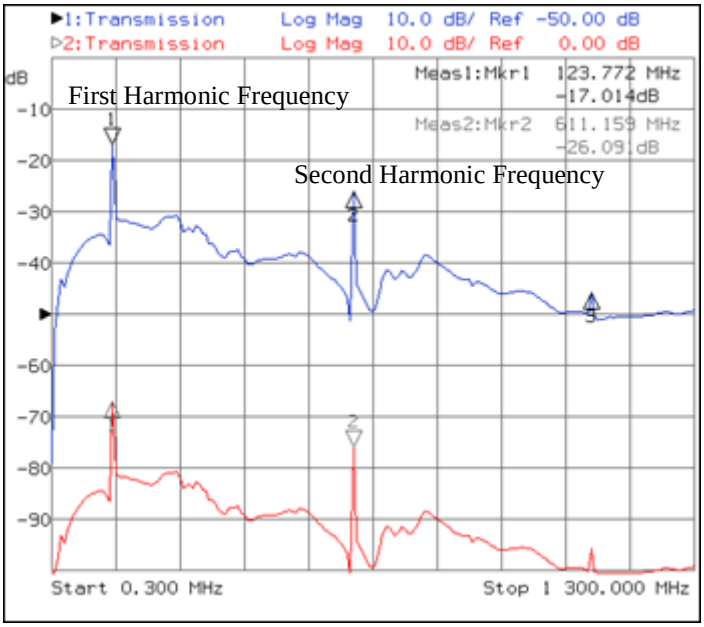

Figure 10: The frequency response of two harmonic frequencies on the 128^0 Y-Z rotated $LiNbO_3$ Substrate.

3.1. Analytic Models for a Single-Phase Bidirectional SAW Resonator

The single-phase bidirectional SAW [23][24] resonator is a basic design for a SAW devices as shown in Figure 11. Its elements are uniform finger spaces and constant finger overlap employed in the input and output IDT. The electric energy from the input is converted into mechanical energy and transferred in the stress-strain filed on the solid

surface. These processes cannot be modeled by passive LC circuit techniques. A different approach, the Crossed-Field Model, the analysis of SAW resonators, is employed to describe the energy transferring between the input and output. The frequency responses are based on the Crossed-Field Model and its simulations are discussed in the following sections.

3.1.1. Geometry of Bidirectional SAW Resonator

A SAW device consists of input and output IDT on the piezoelectric material. The bidirectional SAW resonators shown in Figure 11 have uniform finger spacing and constant finger overlap in the input/output IDTs. When the input IDT is stimulated by AC signals in its frequency range, the surface acoustic waves propagate outward in two directions along the propagation axis. The acoustic waves propagating toward the output IDT generate the electric charge distribution at the output IDT, however, only half of the power in maximum received by the output IDT. The other half power from the input IDT becomes a power loss due to the escaped acoustic waves. These escaped acoustic waves cause a frequency response with a low insertion loss (< -6dB or < 20log0.5).

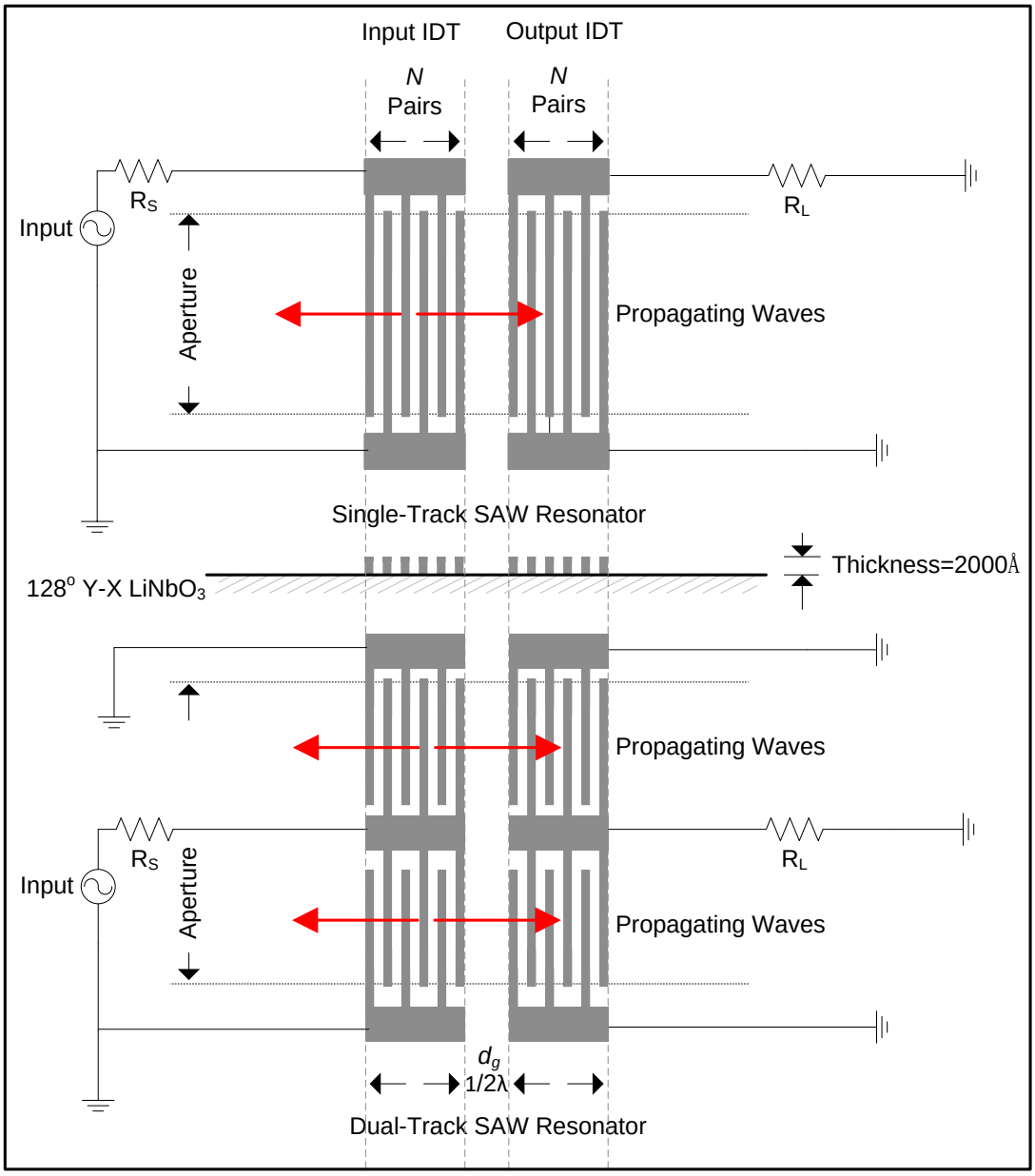

Figure 11: Elementary structures and distance parameters of the single-track and dual-track bidirectional SAW resonator. It has the uniform IDTs in the input and output.

3.1.2. The Crossed-Field Model of Bidirectional Devices

In order to model the bidirectional SAW resonator, the Crossed-Field Model [1] is employed to translate the SAW device into a two port equivalent circuit. The crossed-field model yields a better agreement for the SAW device on the high-K^2 piezoelectric material, such as 128^o YX $LiNbO_3$. In the adaption of crossed-field model, the input /output IDTs can be represented three-port networks. In Figure 12, Ports 1 and 2 are acoustic ports which generate the acoustic waves along the opposite propagation axis. Port 3 is an electrical port of input or output signals. When the input and output IDTs are placed next to each other, the acoustic waves from the Port 2 of the input IDT propagate into the Port 1of the output IDT. The acoustic signals are transmitted in the transmission line between input/output IDTs as shown in Figure 12. In order to reduce the loss in the transmission line, the separation between input/output IDTs is equal to the minimum distance ($d_g=1/2\lambda$). The fingers in the output IDT are also placed synchronously on the maximum displacement in the Z axis of the acoustic waves.

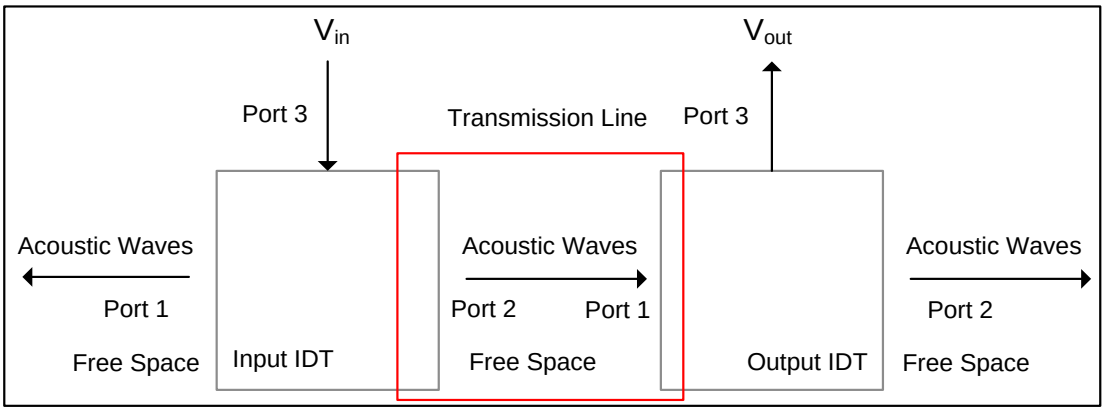

Figure 12: Matrix blocks of bidirectional SAW resonators. The IDT can be translated into a three-port network. Port 3 is electrical port. Port 1 and Port 2 are acoustic ports. The

acoustic waves excited from port 2 propagate away from output IDT. These escaped acoustic waves in port 2 cause the power loss to the output IDT.

In the Crossed-Field Model, the acoustic waves in Port 1 and Port 2 are converted into the equivalent electrical parameters. The three-port network of a single IDT is translated to an admittance matrix. As shown in Figure 13, the R_S represents input resistors. G_o is the equivalent electrical characteristic conductance in the transmission line. C_T is the total capacitance between fingers in the IDT. The three-port network is expressed as a 3x3 admittance matrix [Y].

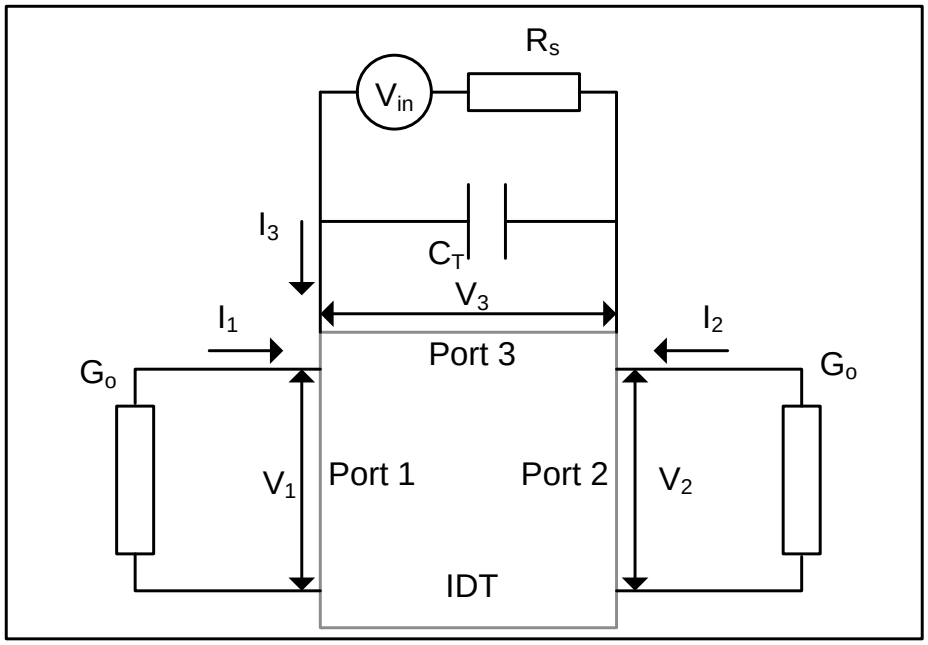

Figure 13: Three-port equivalent Y admittance network of IDT. G_o is the equivalent electrical conductance and C_T is the total capacitance of electrodes.

The current-voltage relations $\begin{bmatrix} I_1 \\ I_2 \\ I_3 \end{bmatrix} = [Y] \begin{bmatrix} V_1 \\ V_2 \\ V_3 \end{bmatrix} = \begin{bmatrix} Y_{11} & Y_{12} & Y_{13} \\ Y_{12} & Y_{11} & -Y_{13} \\ Y_{13} & -Y_{13} & Y_{33} \end{bmatrix} \begin{bmatrix} V_1 \\ V_2 \\ V_3 \end{bmatrix}$ Equation 5

,where the admittance matrix Y is explained as $\begin{bmatrix} Y_{11} & Y_{12} & Y_{13} \\ Y_{12} & Y_{11} & -Y_{13} \\ Y_{13} & -Y_{13} & Y_{33} \end{bmatrix}$.

$$Y_{11}(f) = -jG_0 \cot(N\theta) = -jK^2 f_0 C_s \cot\left(N \cdot 2\pi\left(\frac{f}{f_0}\right)\right)$$ Equation 6

$$Y_{12}(f) = jG_0 \csc(N\theta) = jK^2 f_0 C_s \csc\left(N \cdot 2\pi\left(\frac{f}{f_0}\right)\right)$$ Equation 7

$$Y_{13}(f) = -jG_0 \tan\left(\frac{\theta}{4}\right) = -jK^2 f_0 C_s \tan\left(\frac{2\pi\left(\frac{f}{f_0}\right)}{4}\right)$$ Equation 8

$$Y_{33}(f) = j4NG_0 \tan\left(\frac{\theta}{4}\right) + j\omega C_T = j4NK^2 f_0 C_s \tan\left(\frac{2\pi\left(\frac{f}{f_0}\right)}{4}\right) + j2\pi f_0 C_T$$ Equation 9

, where

K^2	electromechanical coupling constant
f_o	IDT center frequency
C_s	static capacitance of one periodic section
C_T	the total IDT capacitance
G_o	the equivalent characteristic admittance
θ	electrical transit angle
N	total number of fingers

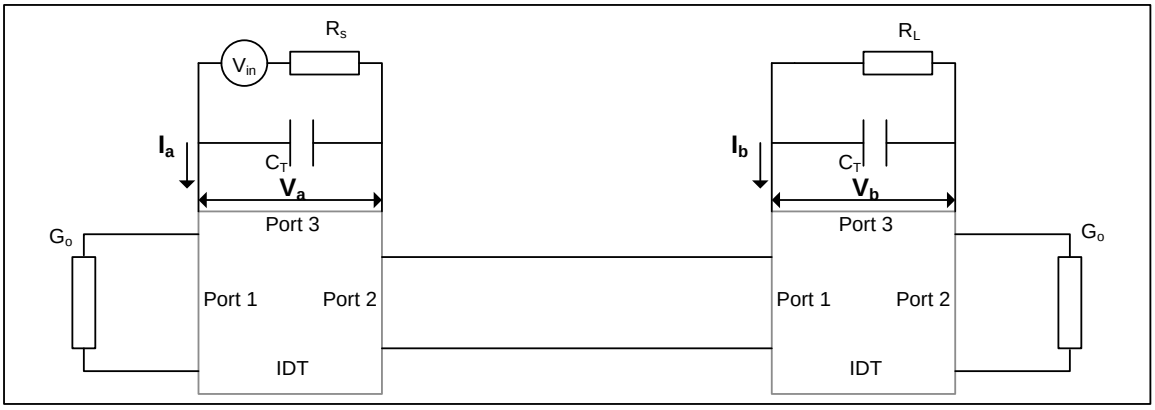

Figure 14: The three-port network of input/output IDTs. V_a and V_b are electrical port of input and output respectively which can be translate into a two-port equivalent circuit.

The three-port Y admittance of the input and output IDTs are shown in Figure 14. The input voltage can be expressed as $V_{in} = V_a + I_a R_s$, where R_s is the source resistance. The output voltage V_L can be expressed as $V_L = V_b$. The currents of I_a and I_b are shown in Equation 10. From Equation 10 and Equation 11, the transfer function *H(f)* of input and output voltage are obtained in Equation 12.

The current-voltage relation $\begin{cases} I_a = y_{aa}V_a + y_{ab}V_b \ (at\ input) \\ I_b = y_{ba}V_a + y_{bb}V_b \ (at\ output) \end{cases}$ Equation 10

The input, output and transfer admittances $\begin{cases} y_{aa} = \frac{I_a}{V_a}\Big|_{V_b=0} \ (at\ input) \\ y_{bb} = \frac{I_b}{V_b}\Big|_{V_a=0} \ (at\ output) \\ y_{ba} = \frac{I_b}{V_a}\Big|_{V_b=0} \ (input - to - output) \\ y_{ab} = \frac{I_a}{V_b}\Big|_{V_a=0} \ (output - to - input) \\ y_{ba} = y_{ab} \end{cases}$

Equation 11

The transfer function $H(f) = \frac{V_L}{V_{in}} = \frac{y_{ab}R_L}{(1+y_{aa}R_s)(1+y_{bb}R_L)-y_{ab}^2R_sR_L}$ Equation 12

3.1.3. The Equivalent Circuit and Insertion Loss

The two-port equivalent circuit can be converted from Figure 14 to Figure 15. The output IDT is excited by a high-impedance current source. The Y admittances defined in Equation 11 can be simulated by using sinc function ($\left|\frac{\sin X}{X}\right|$) instead of tan ($\frac{\theta}{4}$). So the input admittance y_{aa} of the two-port equivalent circuit is shown in Equation 14 when the output IDT is shorted circuit, and y_{bb} is the output admittance in term of *M* finger pairs in the output IDT. The third term y_{ab} in Equation 16 is transfer admittance, including input and output parameters, where ϕ is a phase parameter of the separation between the input/output IDTs' phase centers. The insertion loss (*IL*) in Equation 17, involving of Y admittances and source/load resistance is the ratio of power received at the load resistance to the maximum available power from the source.

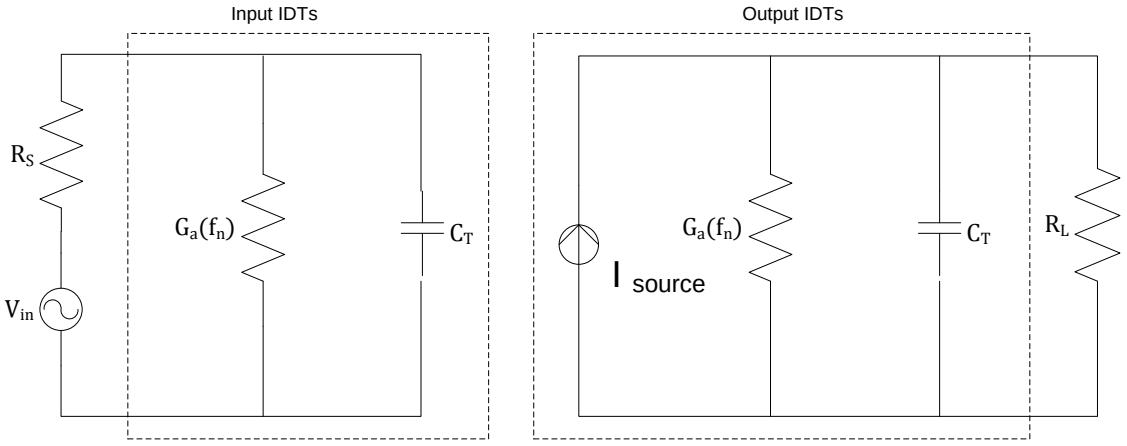

Figure 15: The equivalent circuit for a bidirectional SAW resonator. The three-port networks of input and output IDTs are translated into two port circuit. R_s and R_L are source and load resistances. The current source which is proportional to the amplitude excites the output IDT.

Radiation Conductance $G_a(f) \approx 8K^2 f_0 C_s N^2 \left| \frac{\sin\left[\frac{N\pi(f-f_0)}{f_0}\right]}{\left[\frac{N\pi(f-f_0)}{f_0}\right]} \right|^2$ Equation 13

Input admittance $y_{aa} = Y_{33}(f) \approx G_a(f) + j2\pi f_0 C_T \approx 8K^2 f_0 C_s N^2 \left| \frac{\sin\left[\frac{N\pi(f-f_0)}{f_0}\right]}{\left[\frac{N\pi(f-f_0)}{f_0}\right]} \right|^2 +$

$j2\pi f_0 C_T$ Equation 14

Output admittance $y_{bb} = Y_{33}(f) \approx G_a(f) + j2\pi f_0 C_T \approx 8K^2 f_0 C_s M^2 \left| \frac{\sin\left[\frac{M\pi(f-f_0)}{f_0}\right]}{\left[\frac{M\pi(f-f_0)}{f_0}\right]} \right|^2 +$

$j2\pi f_0 C_T$ Equation 15

Transfer admittance

$y_{ab} = Y_{13}(f)Y_{13}(f) \approx 8K^2 f_0 C_s NM \left| \frac{\sin\left[\frac{N\pi(f-f_0)}{f_0}\right]}{\left[\frac{N\pi(f-f_0)}{f_0}\right]} \right| \left| \frac{\sin\left[\frac{M\pi(f-f_0)}{f_0}\right]}{\left[\frac{M\pi(f-f_0)}{f_0}\right]} \right| e^{j[\pi(1-(N+M)(\mathrm{f}-\mathrm{f_0})/\mathrm{f_0})-\phi]}$

Equation 16

Insertion Loss $IL = 20\log_{10}\frac{\mathrm{P_{out}}}{\mathrm{P_{in}}} = -20log_{10} \times \left| \frac{\left[(1+y'_{aa}R_s)(1+y'_{bb}R_L)-{y'_{ab}}^2 R_s R_L\right]\sqrt{R_L/R_S}}{2R_L y'_{ab}} \right|$

Equation 17

, where

$G_a(f)$	radiation conductance
N	number of input IDT finger pairs
M	number of output IDT finger pairs

ϕ phase parameter of the separation between IDT phase centers

3.1.4. The S_{21} Simulation in MATLAB

The insertion loss based on Equation 17 is simulated in MATLAB as shown in Figure 16. The center frequency is 121MHz when the number of finger pairs is 30 for input and output IDTs. The maximum insertion loss is -14.3124 which occurs in the center frequency. The insertion loss is much higher than -6dB due to its bidirectional IDT structures. Half the power from the input IDT is not received by the output IDT. According to the simulation results in Figure 16, the bandwidth is 2.7MHz which results in a low Q factor (Q = 45).

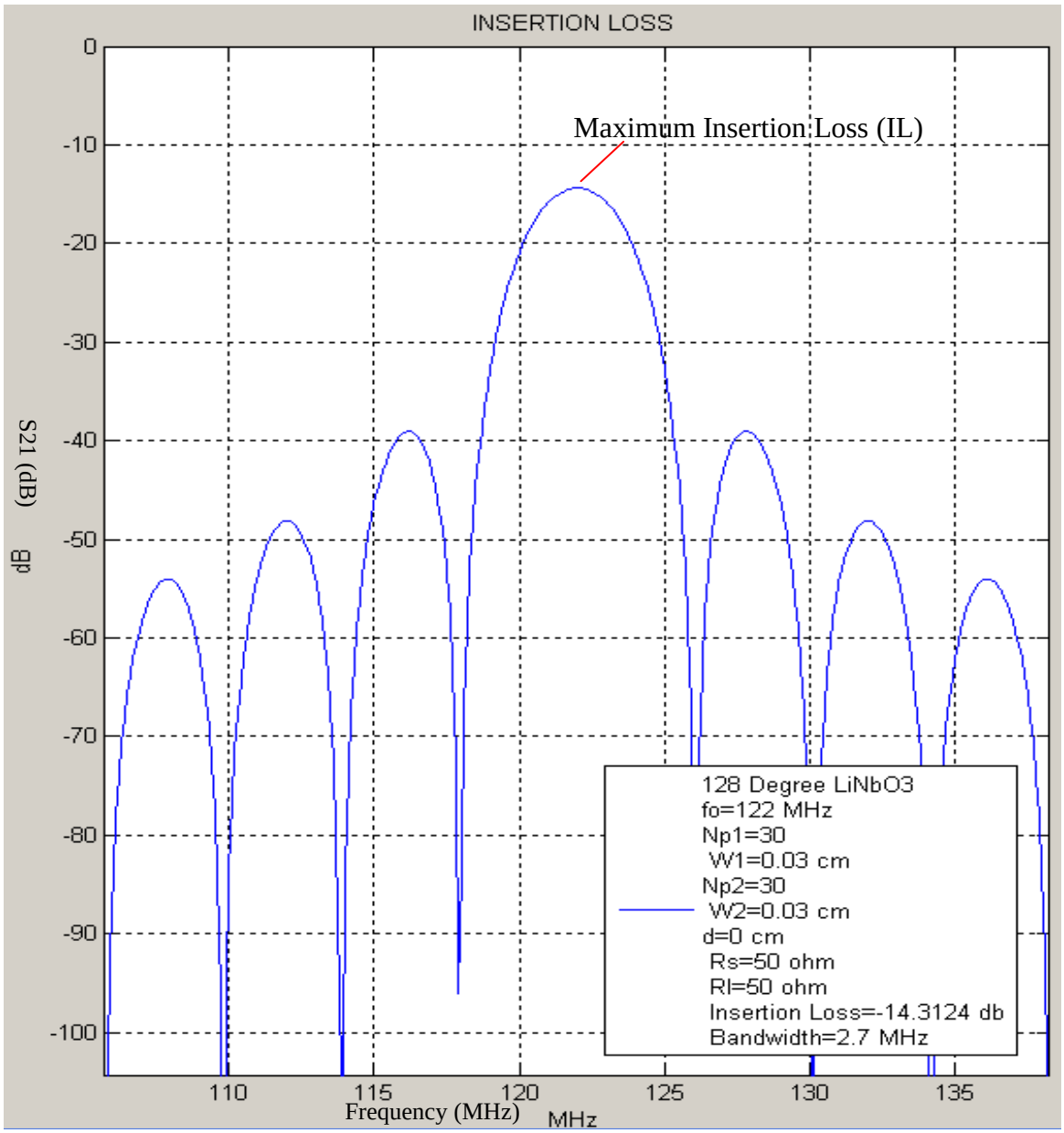

Figure 16: The MATLAB simulation of the bidirectional SAW resonators on the LiNbO3 substrate. The maximum insertion loss of S21 response is -14.3124 dB in 121MHz when the finger pairs in the input and output IDT are 30.

3.2. The Properties of the 128° YX $LiNbO_3$

The piezoelectric properties are important factors in SAW designs and the Crossed-Field Model. In this work, the 128° YX $LiNbO_3$ substrate is used as the piezoelectric medium for the acoustic waves. It is the piezoelectric crystal substrates that can generate surface acoustic waves. The high electromechanical coupling coefficient K^2 [21] of 128° YX $LiNbO_3$ can improve the efficiency in converting mechanic waves to electrical signals in the receiving IDT, however, lithium niobate crystals have a nonzero temperature coefficient. The disadvantages of temperature coefficient are also discussed in this section.

3.2.1. Characteristics of SAW and Leaky-SAW (LSAW) Devices

Leaky SAW [19][20][22] are device in which waves propagate though the bulk. Surface acoustic waves (Rayleigh waves) and Leaky-SAW are acoustic waves on the two common piezoelectric materials. The patterns of acoustic waves of SAW and LSAW devices are shown in Figure 17. The acoustic waves of SAW devices only propagate along the propagation axis on the surface. The substrate of LSAW devices, like 64° YX $LiNbO_3$ or 36° YX $LiNbO_3$, has Rayleigh and bulk wave propagation at the same time. In this work, we select the 128° YX $LiNbO_3$ as the substrate of SAW resonators. Although 64° YX $LiNbO_3$ or 36° YX $LiNbO_3$ have higher values of Electromechanical Coupling Coefficient K^2 and velocity v, the bulk waves reflecting back from the bottom interfere with the Rayleigh waves on the surface. This interference makes it complex to design LSAW devices. This implies that LSAW devices have less mass sensitivity on the surface

than SAW. This is because there are less Rayleigh waves on the surface, as compared with SAW devices. In this work, 128° YX $LiNbO_3$ was selected as the substrate for the SAW resonators. The angle of the particular crystal cut is 128°, which is rotated on the YZ counterpart. The 128° YX $LiNbO_3$ has pure acoustic waves propagating along the x axis on the surface and high sensitivities for sensing applications.

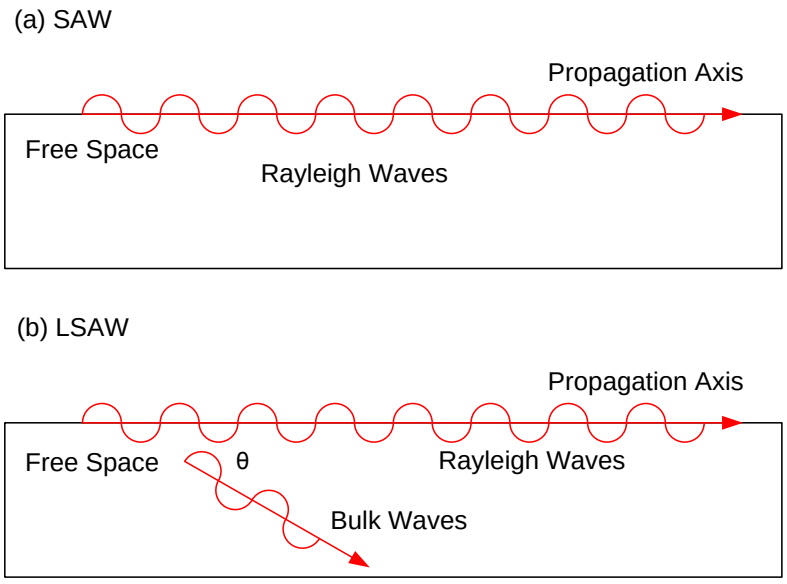

Figure 17: The pattern of acoustic waves on the free space of SAW and LSAW devices. (a) Surface acoustic waves (Rayleigh waves) (b) Rayleigh waves and bulk waves in the LSAW devices.

3.2.2. Electromechanical Coupling Coefficient K^2 and Velocity

The most practical properties related to the surface acoustic waves are the velocity v and electromechanical coupling coefficient K^2[19][20][22]. The velocity v is related to the speed of the acoustic waves and the center frequency f_o of SAW devices. The K^2 is

the efficiency in converting the applied electrical signals into the mechanical energy of the acoustic waves. It is also related to the maximum insertion loss of two-port SAW resonators. Table 2 lists the properties of common piezoelectric substrates. 128° YX $LiNbO_3$ has high velocity (3992 m/s) and K^2 (5.3%). These two properties yield to a higher center frequency and insertion loss than other piezoelectric materials. Figure 18 shows the MATLAB simulation of the insertion loss versus finger pairs. The insertion loss is given in Equation 17. This MATLAB simulation is based on the theoretic model of the bidirectional SAW resonator in the previous section for the different materials listed in Table 2. The high K^2 materials, like 128° YX $LiNbO_3$ or $LiTaO_3$, have higher insertion loss than the low K^2 materials as shown in Figure 20 [1][19][20][22].

Material	Crystal Cut	SAW Axis	Velocity (m/s)	K^2 (%)	Temp Coefficient (ppm/°C)	Capacitance/Finger Pair/Unit Length C_o (pF/cm)
Quartz	ST	X	3158	0.11	~0 near 25°C	0.55
Lithium Niobate $LiNbO_3$	Y	Z	3488	4.05	94	4.6
$LiNbO_3$	128°	X	3992	5.3	75	5.0
Bismuth Germanium Oxide $Bi_{12}GeO_{20}$	110	001	1681	1.4	120	_
Lithium tantalite $LiTaO_3$	77.1° rotated Y	Z'	3254	0.72	35	4.4
Gallium arsenide GaAs	110	<110>	<2841	<0.06	35	_

Table 2: The properties of common piezoelectric substrates for SAW resonators. 128° YX LiNbO3 has a high electromechanical coupling coefficient K2 and acoustic velocity.

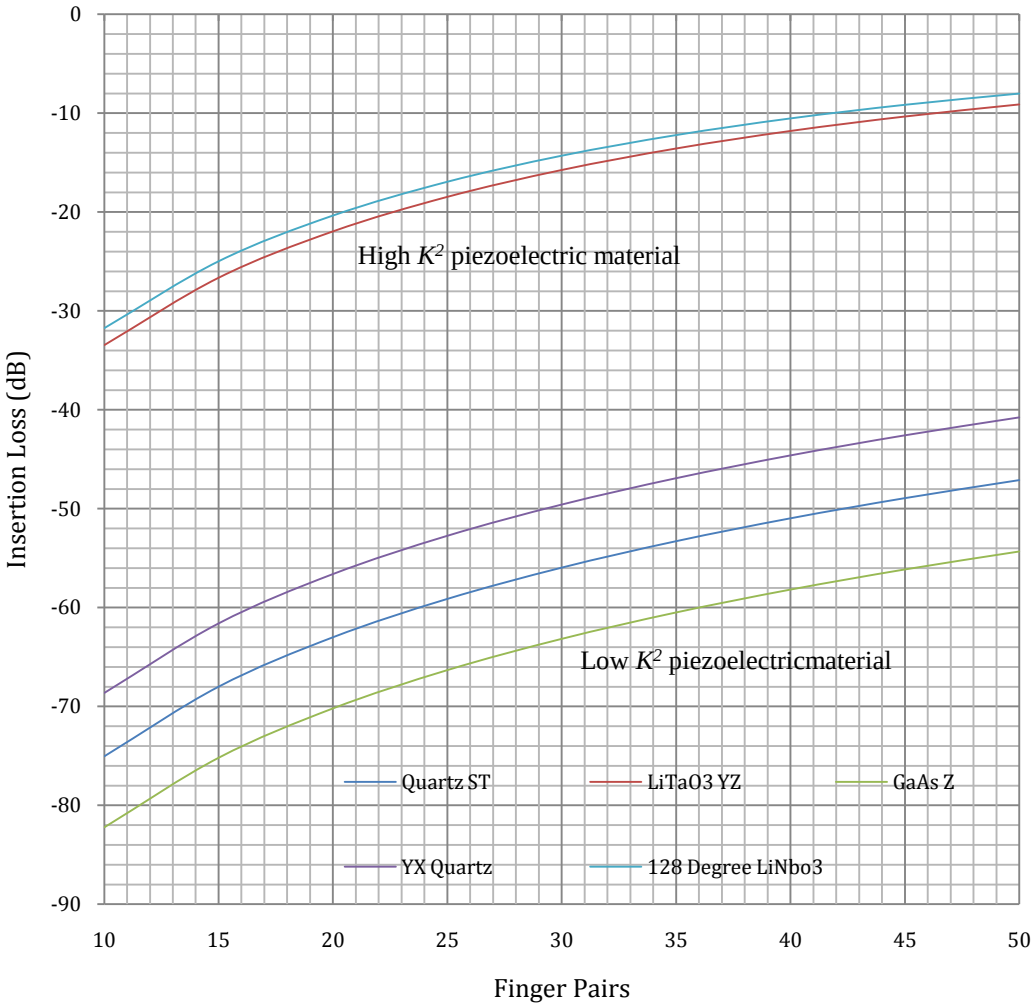

Figure 18: The maximum insertion loss of bidirectional SAW resonators versus finger pairs. According to the equivalent circuit in the previous section, the insertion loss is relative to the finger pairs in the input and output IDTs. The high K^2 material, like $LiNbO_3$, has higher insertion loss in comparison with the low K^2 material.

Figure 17 shows the relationship between the insertion loss and finger pairs on the 128^o YX $LiNbO_3$ substrate. It is simulations of bidirectional SAW filters based on the Cross-Field Model in the previous section. The maximum insertion loss increases while the number of finger pairs in the input/output IDTs increases. This increase becomes saturated after the finger pairs are greater than 20.

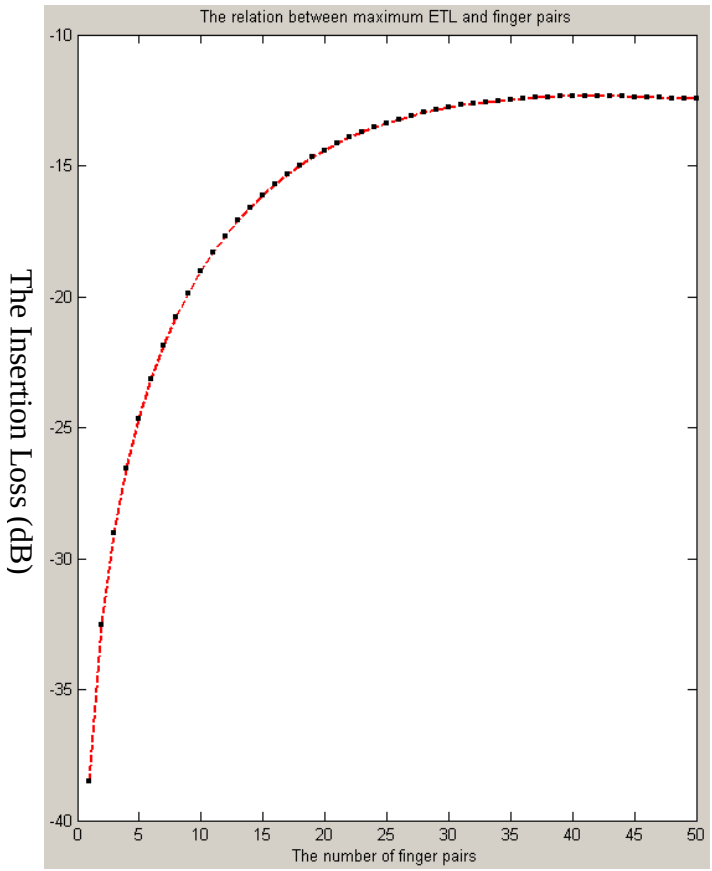

Figure 19: The maximum insertion loss of bidirectional SAW resonators on the 128^{o} YX $LiNbO_3$ substrates.

3.2.3. Temperature Coefficient

Table 2 shows that the 128^{o} YX $LiNbO_3$ substrate has a high temperature coefficient (75 ppm/ ^{o}C) which is related to the velocity of the acoustic waves [21]. With an increase in temperature, it causes the downward shift of the center frequency. If the temperature increases 1 ^{o}C, the center frequency shifts 13.3 KHz. Temperature stability is an important factor for using SAW devices as narrowband resonators and mass sensors. In this research, the SAW resonator on the 128^{o} YX $LiNbO_3$ substrate was used as a mass

sensor. The device had a frequency shifts when the mass was deposited on the electrodes. If the temperature is changing during the measurement, the factors of temperature changes have to be considered when measuring the center frequency to shift at the same time. In Chapter 5, we will discuss further how to solve this temperature effect during the measurements.

3.3. Proposed One-Pole Synchronous SAW Resonators

The 128^o YX $LiNbO_3$ substrate has properties of high velocity v and K^2, however, the bidirectional SAW resonators on the high K^2 substrate also have larger bandwidth and lower Q factors. In telecommunication, the bidirectional SAW resonators on the 128^o YX $LiNbO_3$ substrate are most often used as wideband midloss IF resonators. They generally find applications in wideband SAW filters. In order to achieve a narrow bandwidth, the one-pole synchronous SAW resonators are proposed [23][24][28][29]. The escaped acoustic waves in bidirectional SAW resonators are reflected by the shorted reflectors. It not only improves the Q factor, but also the insertion loss in the receiving output IDT.

3.3.1. Geometry of the One-Pole Synchronous SAW Resonator with Shorted Reflectors

The geometry of a one-pole synchronous resonator is illustrated in Figure 20 [27]. The separation between input and output IDTs was minimized to the shortest distance (d_g=1/2λ) so that the propagating loss and phase shift due to the free space between the

two IDTs can be minimized. Acoustic waves excited by input IDT, however, are bidirectional and half the acoustic waves propagate away from the output IDT, which causes the loss in the transmission line. In order to improve this, the shorted reflectors are employed to reflect the acoustic waves back to the output IDT [30][31][32]. Figure 21 shows the relationship between the number of single-electrode fingers and the power of reflecting waves. The reflectors were designed with 100 electrodes were designed and placed next to the input and output IDTs [34][35]. As it is shown in Figure 19, there is near 100% reflecting from 100 electrodes. The power of the propagating waves can almost be almost reflected back to the output IDT. Figure 20 shows the propagating acoustic waves and reflecting acoustic waves in the SAW resonators. There are two transitions of the acoustic waves. The first transition AW1 is the propagating acoustic waves which travel to the output IDT directly and are converted into electrical signals. The second transition AW2 is the reflecting acoustic waves which are the acoustic waves reflected from the reflectors back to the output IDT. The escaped acoustic waves AW3 from the input IDT are also reflected back to the output IDT and propagated though the input IDT. The 100 electrodes were chosen to reflect the entire wave back to the IDT according to Figure 21. This implies that these two reflecting acoustic waves in the output IDT results in an asymmetric resonance with 90^{o} phase shift in the center frequency [36][37][38]. The resonance from the second transition AW2, AW3 of acoustic waves is superimposed on the resonance from the first transition AW1. This superimposed resonance not only increases the insertion loss, but also has a one-pole response in the center frequency.

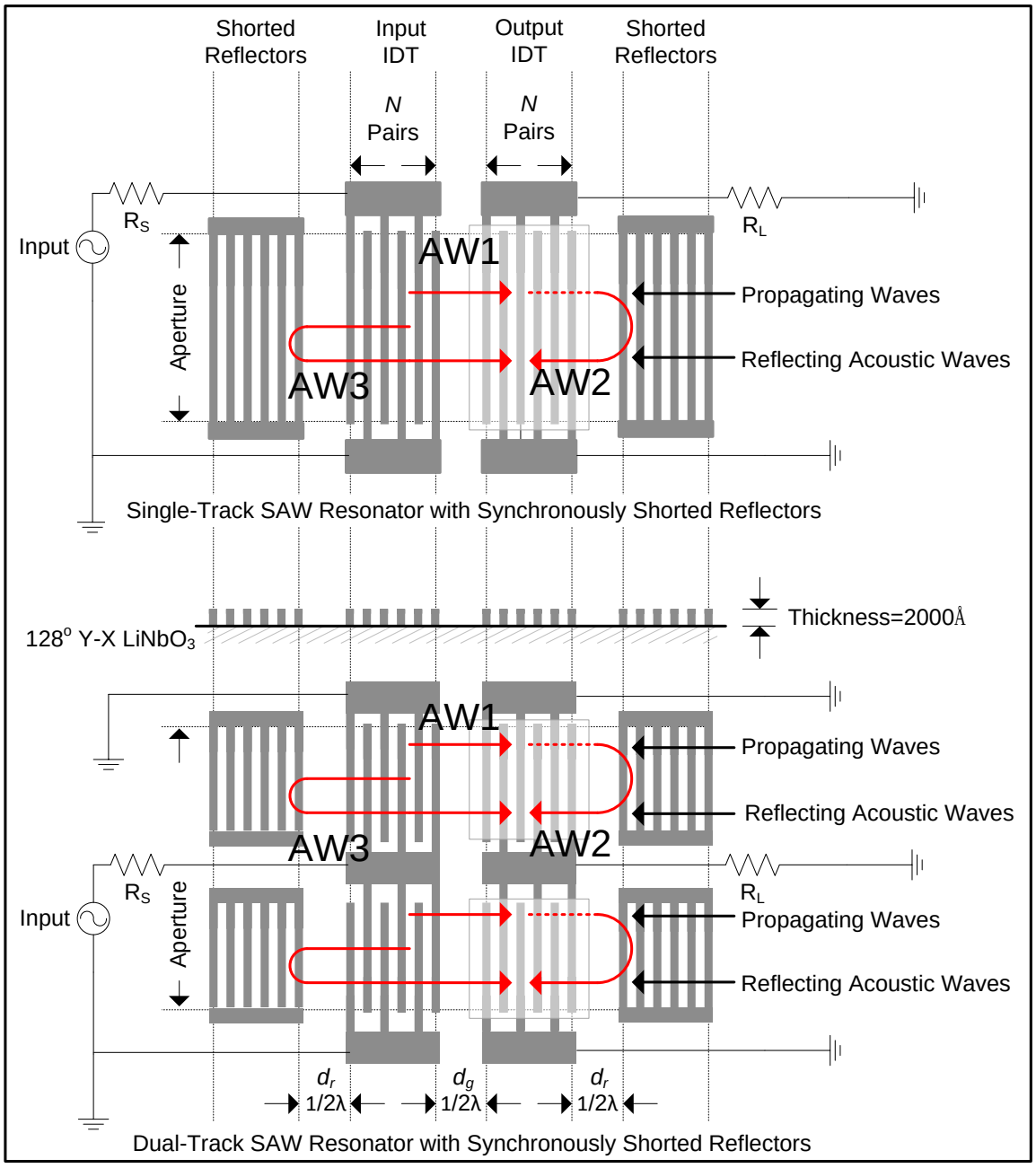

Figure 20: The Single-Track and Dual-Track SAW resonators with synchronously shorted Reflectors. The reflecting acoustic waves results in an asymmetric resonance with $\pm 90^{o}$ phase shift superimposed in the center frequency.

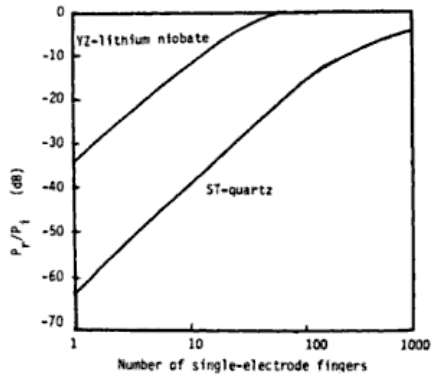

Figure 21: The ratio of power reflection from the electrodes of reflectors on the 128° YX $LiNbO_3$ and ST Quartz. The metallization η is 0.5. The power reflected by 10 electrodes on the YX $LiNbO_3$ is equal to the same power reflected by 100 electrodes on ST Quartz [34][35].

3.3.2. The Y Admittance and IL Modeling for the Proposed One-Pole Synchronous SAW Resonators

In this section, we will modify the previous Cross-Field model to include the superimposed reflecting acoustic waves [25][26][29]. This results in a new equation for the insertion loss. The radiation conductance is expressed $G_a(f)$ as sinc function in the center frequency f_a. The equivalent circuit can be expressed by the Y admittance function of $G_a(f)$ and C_T. y_{aa} is the input admittance when the output IDT is short-circuited. In the same way, the output admittance y_{bb} can be obtained when the input IDT is short-circuited. The remaining term y_{ab} is the transfer admittance involving both input and output parameters. Φ is a phase between input and output IDT. The insertion loss IL for SAW resonators can be defined based on Y admittance involving the source and load resistance R_S and R_L [33]. The one-pole synchronous resonators have another

resonance/acoustic waves superimposed in the center frequency. This superimposed resonance in the center frequency is generated by the reflecting acoustic waves in the output IDT. The propagating waves are reflected back to the output IDT by the shorted reflectors as explained in section 3.2. These reflecting waves generate the second resonance with 90^o phase shift in the center frequency as discussed above. The additional resonance results in an asymmetric frequency response due to 90^o phase shift [36][37][38], with the increase in insertion loss as well as the lower upper stop band as shown in Figure 23. This additional resonance can also have a near-match (50ohm) at center frequency. The superimposed resonance can be simulated by using another sinc function $\left|\frac{\sin(X)}{X}\right|^2$ and a phase θ as shown in Equation 21.

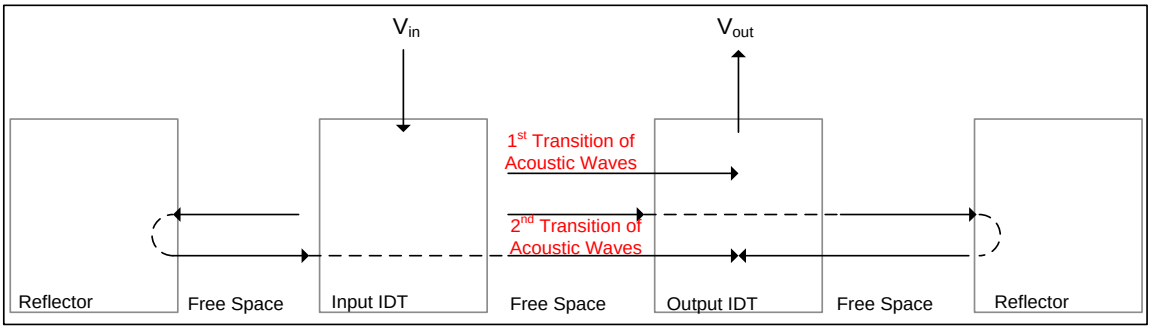

Figure 22: Matrix blocks of a two-port one-pole SAW resonator. There are two transitions of acoustic waves propagating to the output IDT. The first transition of acoustic waves propagates to the output IDT directly. The second transition of acoustic waves are the reflecting waves in the output IDT reflected by reflectors.

Input admittance

$$y_{aa} = Y_{33}(f) \approx G_a(f) + j2\pi f_0 C_T \approx 8K^2 f_0 C_s N^2 \left| \frac{\sin\left[\frac{N\pi(f-f_0)}{f_0}\right]}{\left[\frac{N\pi(f-f_0)}{f_0}\right]} \right|^2 + j2\pi f_0 C_T$$

Equation 18

Output admittance

$$y_{bb} = Y_{33}(f) \approx G_a(f) + j2\pi f_0 C_T \approx 8K^2 f_0 C_s M^2 \left| \frac{\sin\left[\frac{M\pi(f-f_0)}{f_0}\right]}{\left[\frac{M\pi(f-f_0)}{f_0}\right]} \right|^2 + j2\pi f_0 C_T$$

Equation 19

Transfer admittance

$$y_{ab} = Y_{13}(f)Y_{13}(f) \approx 8K^2 f_0 C_s NM \left| \frac{\sin\left[\frac{N\pi(f-f_0)}{f_0}\right]}{\left[\frac{N\pi(f-f_0)}{f_0}\right]} \right| \left| \frac{\sin\left[\frac{M\pi(f-f_0)}{f_0}\right]}{\left[\frac{M\pi(f-f_0)}{f_0}\right]} \right| e^{j[\pi(1-(N+M)(\mathrm{f}-\mathrm{f}_0)/\mathrm{f}_0)-\phi]}$$

Equation 20

Insertion Loss

$$IL = \left(20\log_{10}\left|\frac{[(1+y_{aa}R_s)(1+y_{bb}R_L)-y_{ab}R_sR_L]\sqrt{R_L/R_s}}{2R_L y_{ab}}\right|\right) \times \left[1 + \left(\left|\frac{\sin\left[\frac{N^2\pi(f-f_0)}{f_0}\right]}{\left[\frac{N^2\pi(f-f_0)}{f_0}\right]}\right|^2 - \right.\right.$$

$\sin N2\pi(f-f0)f0-\theta N2\pi(f-f0)f0-\theta 2$

Equation 21

, where

$G_a(f)$	radiation conductance
N	number of input IDT finger pairs
M	number of output IDT finger pairs
Φ	phase parameter of the separation between IDT's phase centers
θ	phase shift of second resonance in the center frequency

3.3.3. The S_{21} and Maximum IL in MATLAB Simulations of the Proposed One-Pole Synchronous SAW Resonators

3.3.4.

The frequency response based on the distance parameters in Figure 20 and Equation 21, is simulated in MATLAB. Figure 23 shows a one-pole resonance superimposed in the center frequency. This superimposed resonance is simulated by using sinc function $\left|\frac{\sin(X)}{X}\right|^2$ with a 90^o phase shift. It results in a symmetric response in the center frequency with increase in the maximum insertion loss and Q factor as shown in Figure 23. There is also a deep notch in the upper stop band due to the 90^o phase shift. In this simulation, the width of the electrodes is 8μm which yields a center frequency of 121MHz. There are 30 finger pairs in the input and output IDT and the separation between input/output IDTs is equal to the minimum distance ($1/2\lambda$).

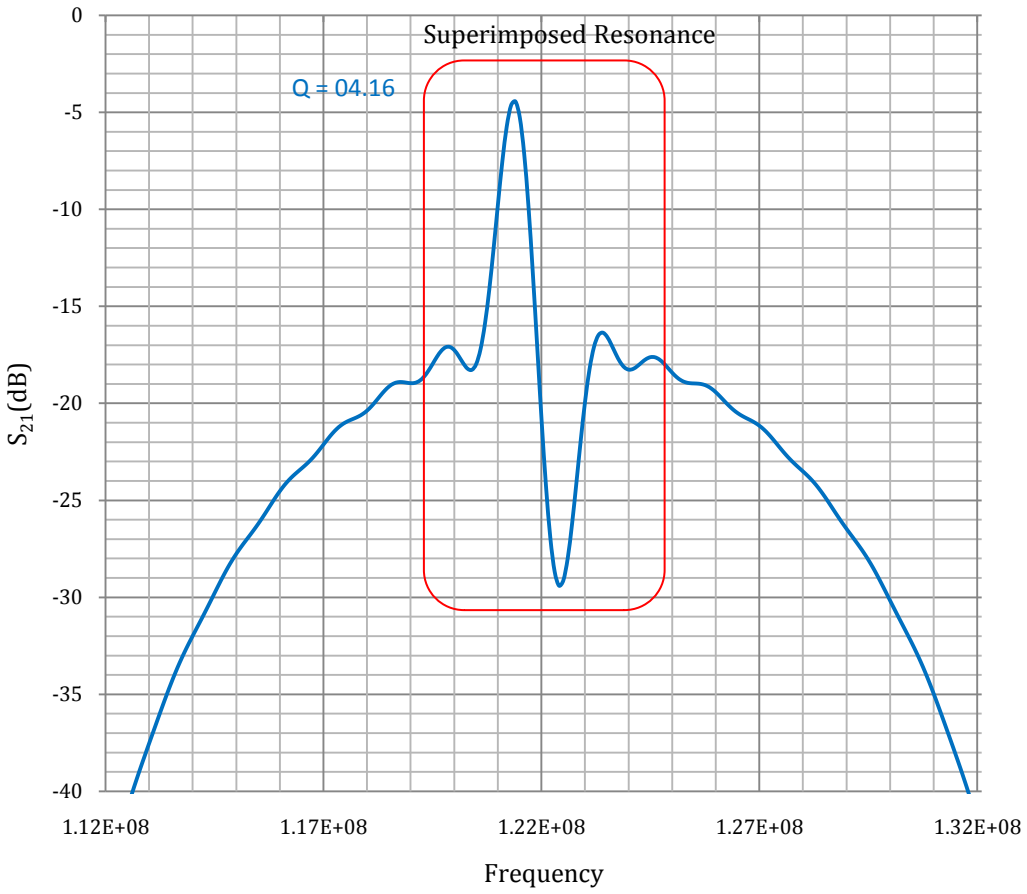

Figure 23: The MABLAB simulation of SAW resonator with shorted reflectors symmetrically placed after input and output IDTs. An asymmetric resonance is superimposed in the center frequency. The maximum insertion loss is -4.86dB in 121 MHz, which is higher than the bidirectional SAW resonator.

3.4. Simulation of One-Pole Synchronous SAW Resonators by Using the Finite Element Method to Analyze

The finite element method (FEM) is a numerical technology used to find the approximation in complicated domains. It is used to analyze the surface acoustic waves on the piezoelectric substrate. The AC electrical signals simulate the piezoelectric

substrate and generate the stress-strain distributions on the surface. The displacements of surface acoustic waves can be modeled and visualized in FEM simulations. In this work, two FEM software programs are used: COMSOL and CoventorWare. They provide the simulations of the displacements in frequency and time domains.

3.4.1. The Simulations of LiNbO3 Crystal Structures in COMSOL

The deformation of the 128^{o} YX $LiNbO_3$ substrate is simulated by COMSOL. COMSOL is commercial software that can simulate and model the physics-based system. It can simulate the conversion between electrical signals and mechanical waves on the surface. In Figure 24, the crystal structures in the 128^{o} YX $LiNbO_3$ substrate show extrusions and expansions. These deformations of the substrate show the disturbances on the surface when acoustic waves propagate. It also generates a potential charge due to its piezoelectric property. The harmonic frequency in this simulation is 121.758MHz based on the properties in Table 3.This simulation shows that the acoustic waves propagate along x axis on the surface of the $LiNbO_3$ substrate, but no vibrate in other directions.

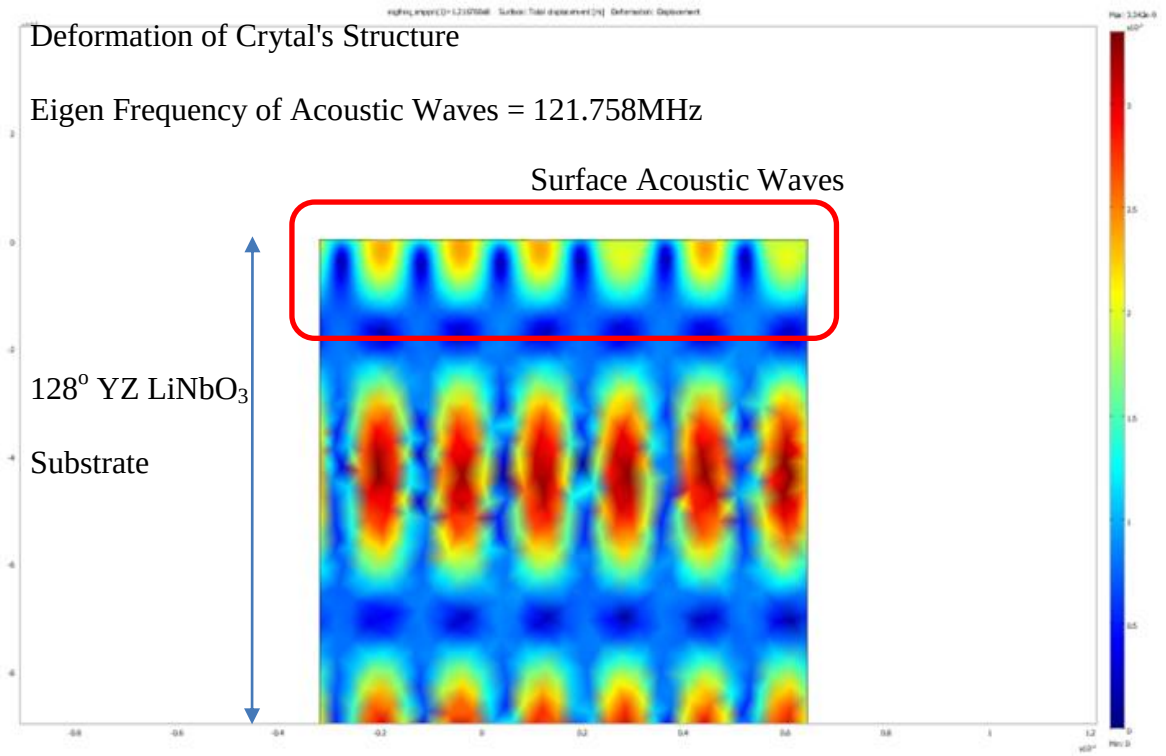

Figure 24: The cross view of the $LiNbO_3$ crystal structures. The crystal structure is disturbed by the surface acoustic waves.

Density (10^3 Kg m^{-3})	4.646
Elastic stiffness (10^{-11} Nm^{-2})	C^E_{11}=2.424 C^E_{12}=0.752 C^E_{13}=0.752 C^E_{22}=2.03 C^E_{23}=0.573 C^E_{25}=0.085 C^E_{33}=2.03 C^E_{35}=-0.085 C^E_{44}=0.752 C^E_{46}=0.085 C^E_{55}=0.595 C^E_{66}=0.595
Piezoelectric strain coefficient (10^{-12} C/N)	d_{11}=1.33 d_{12}=0.23 d_{13}=0.23 d_{24}=-2.5 d_{26}=3.7 d_{32}= -2.5 d_{33}= 2.5 d_{35}=3.7

Table 3: The matrixes of the stiffness and piezoelectric strain of 128° YX $LiNbO_3$. They define the properties of 128° YX $LiNbO_3$ in COMSOL and CoventorWare Simulations [1][2].

3.4.2. The FEM Simulations of Acoustic Waves in Coventorware

The FEM is an approximation used to solve the partial equations in the complication domains. Commercial-off-the-shelf software, Coventorware, can simulate the piezoelectric material by using FEM. The structures of the one-pole synchronous resonators are simulated by using Coventorware to examine acoustic waves on the 128^{o} YX $LiNbO_3$ substrate. The elastic stiffness and piezoelectric strain coefficients of the 128^{o} YX $LiNbO_3$ in Coventorware are shown in Table 3. The steps of fabrication in simulations are shown in Table 4 and the 3D models of SAW resonators are based on the layouts and steps in Table 4. After the 3D models are built, they are meshed by using the Manhattan brick method. The meshed model of SAW resonators are simulated in the time domain and frequency domain. The electrical signals are connected to the input IDT to generate potential differences on the surface. These potential differences excite the piezoelectric material and cause the displacements of acoustic waves in the Z direction. These acoustic waves spread out on the surface and gradually propagate toward the output IDT. Figure 25 shows the transit simulations as related to time. The displacements of acoustic waves are shown in different colors to represent the different magnitudes. They propagate along the propagation axis toward the output IDT. Figure 25 shows the maximum displacements which increase gradually on the surface as the time ranges from 0 to 40 ns.

Number	Step name	Action	Material Name	Thickness (um)	Photoresist
0	Substrate	Substrate	128^{o} YX $LiNbO_3$	50	
1	Planar Fill	Planar Fill	Al	0.2	
2	Straight Cut	Straight Cut			+

Table 4: The depositing and etching processes in Coventorware

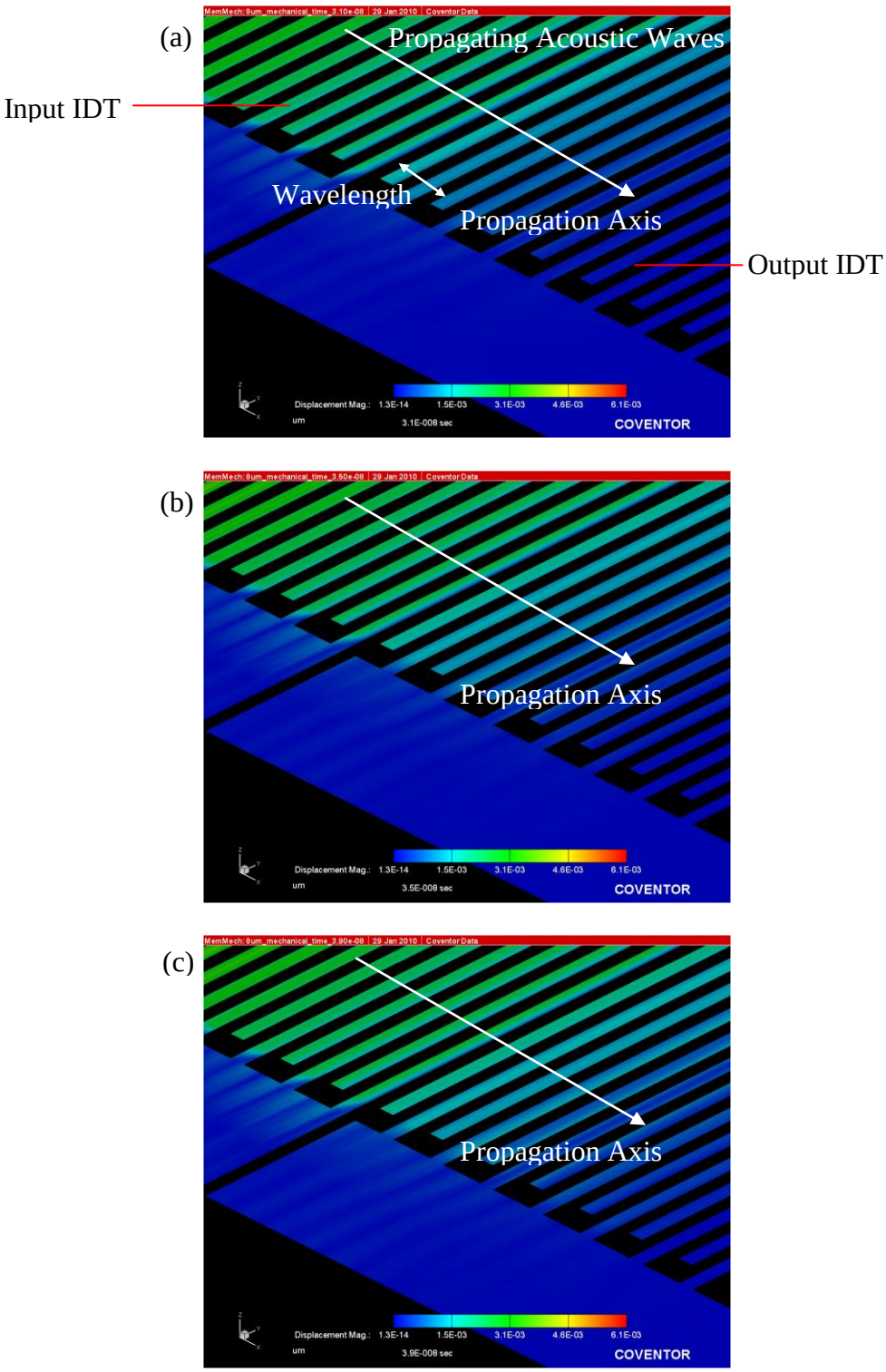

Figure 25: The transit simulation in Coventorware. The acoustic waves propagate gradually from input IDT to output IDT. (a) T = 3.1 e^{-8} s (b) T = 3.5 e^{-8} s (c) T = 3.9 e^{-8} s

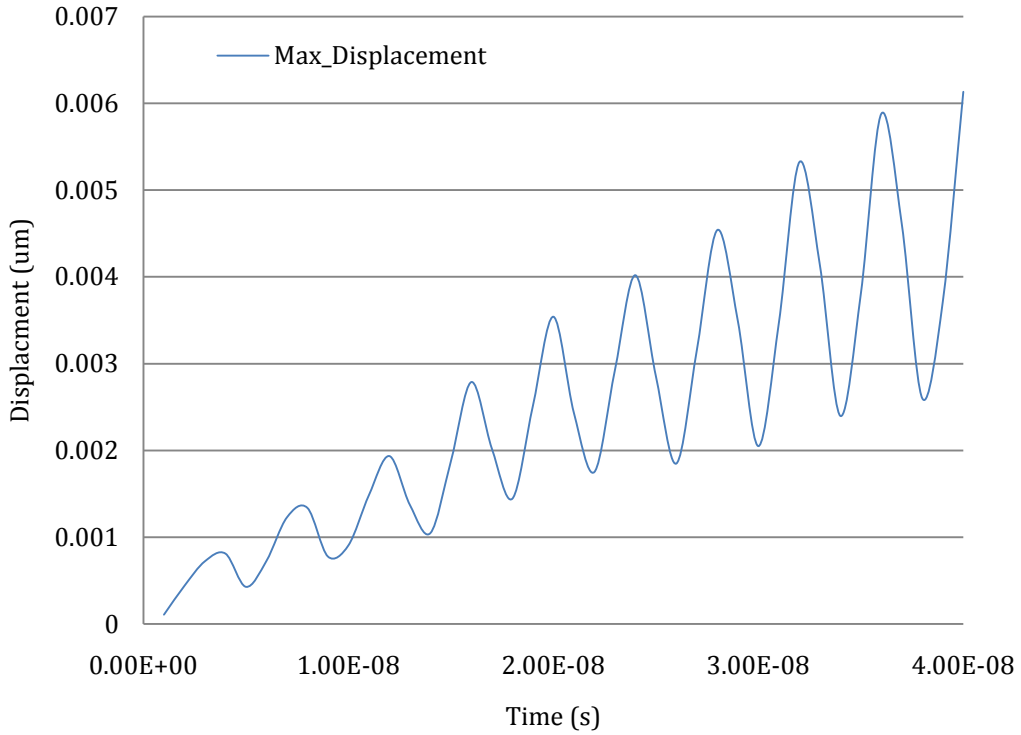

Figure 26: The maximum displacement of the 121MHz resonator increases gradually in the transit simulation.

Harmonic simulations of single-track and dual-track SAW resonators are shown in Figure 28. The width of electrodes in both resonators is 8μm and the number of finger pairs in the input/output IDTs is 10. Both SAW resonators are meshed by Manhattan Brick elements and also shown in Figure 28. Input signals (V_s = 5V) with different frequencies are applied at the input IDTs in the harmonic simulations. 3D models of resonators are established based on the previous requirements and are shown in Figure 28. The acoustic waves are traveling in the input and output IDTs. Maximum displacements occur when the frequency of input signals is equal to the frequency of acoustic waves. Displacements on the surface are translated into electrical signals in the

receiving IDT. Figure 29 shows the displacements in the frequency, which ranges from 100MHz to 150MHz. The maximum displacement occurs in the center frequency f_o, which is the frequency of the acoustic waves. According to simulation results, the center frequency is 127.27MHz with 0.026μm displacement in the Z direction. Another simulation, shown in Figure 30, is the maximum displacement with different numbers of finger pairs in the input/output IDTs. The magnitude of displacement can be increased gradually by adjusting the number of finger pairs in the input/output IDTs.

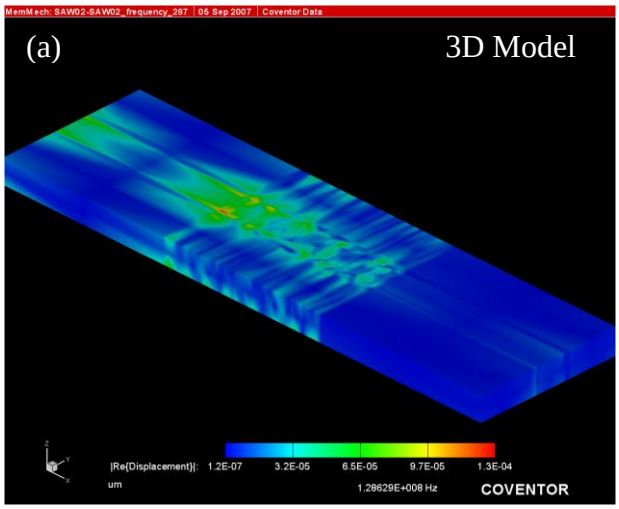

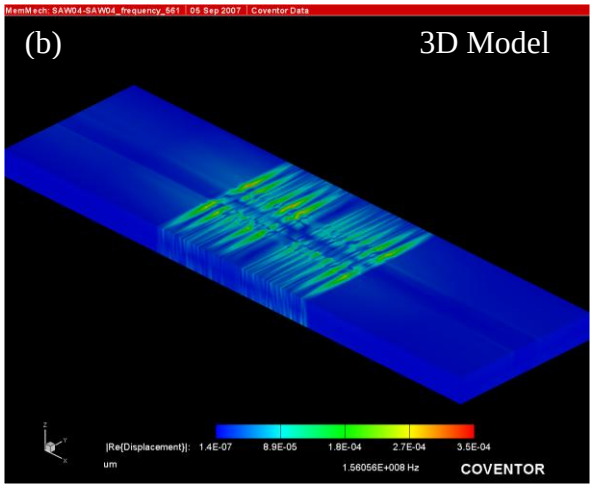

Figure 27: (a)(b)The 3D model of single-track and dual-track bidirectional SAW filters. The acoustic waves propagate between input and output IDTs.

(a)

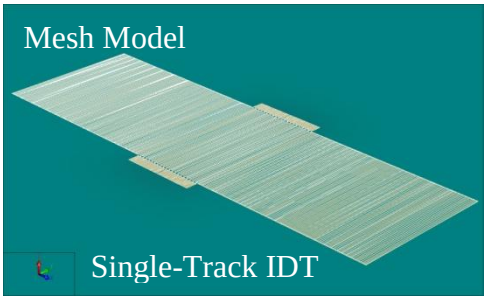

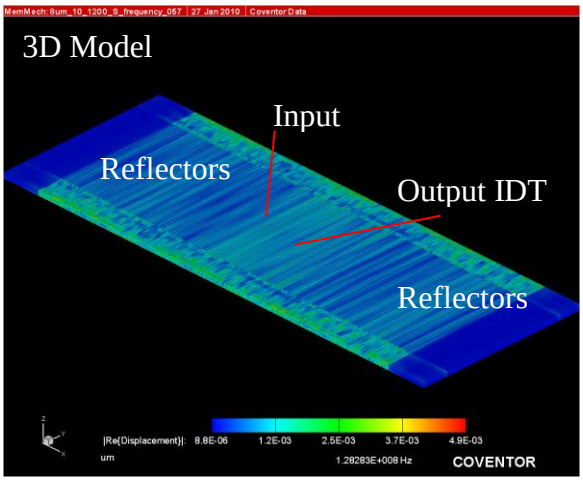

(b)

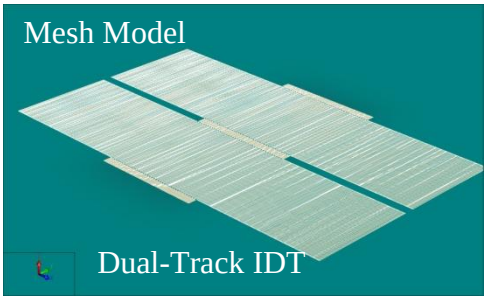

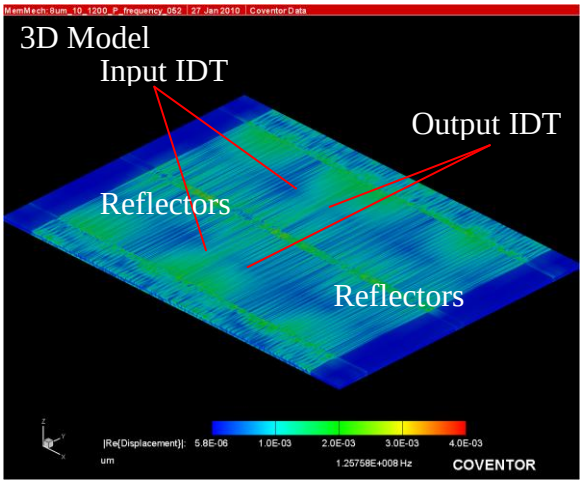

Figure 28: The mash model and 3D model of the Single-Track and Dual-Track SAW resonators with synchronously shorted Reflectors: (a) The Single-Track SAW resonator (b) the Dual-Track SAW resonator. The magnitudes of displacements are shown in different colors.

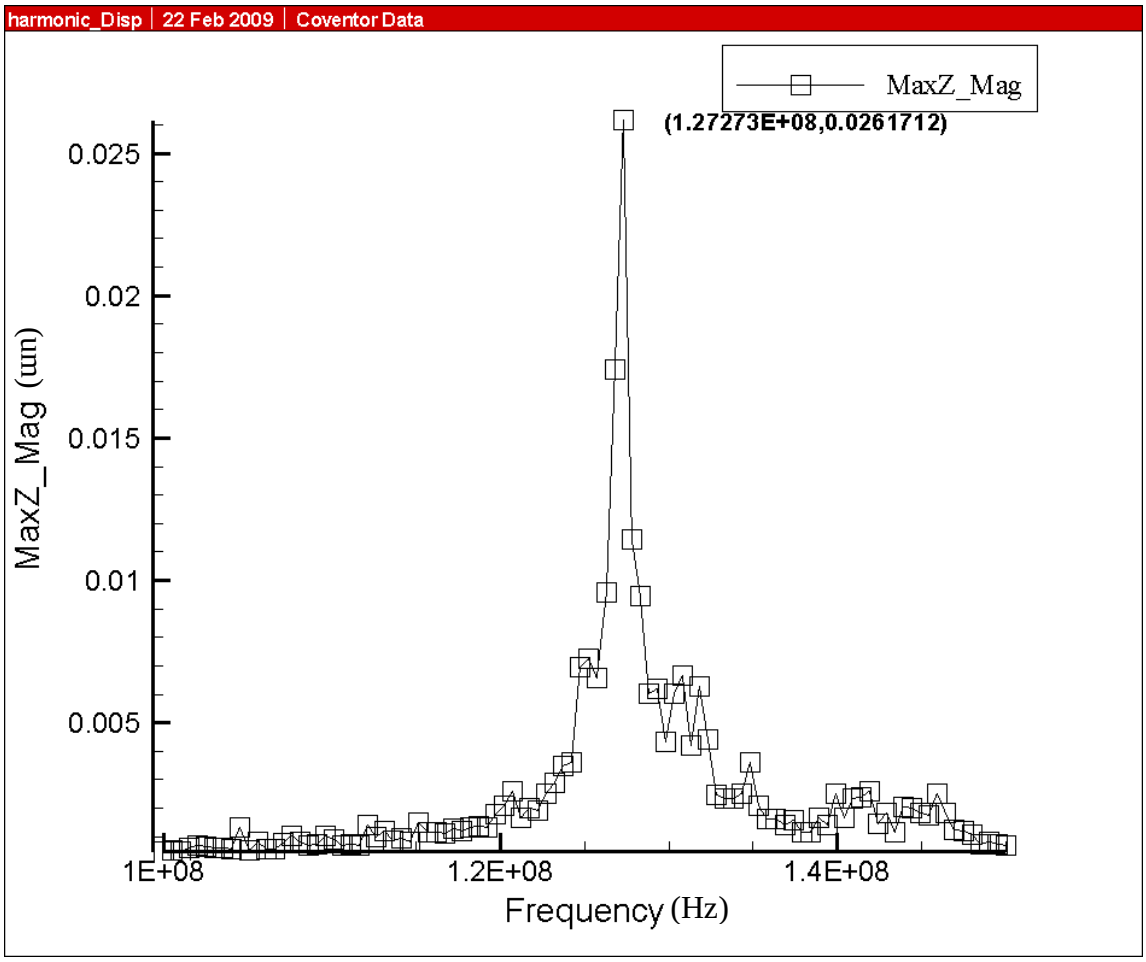

Figure 29: The displacement in Z axis of the SAW resonator with shorted reflectors. The maximum displacement occurred in the center frequency.

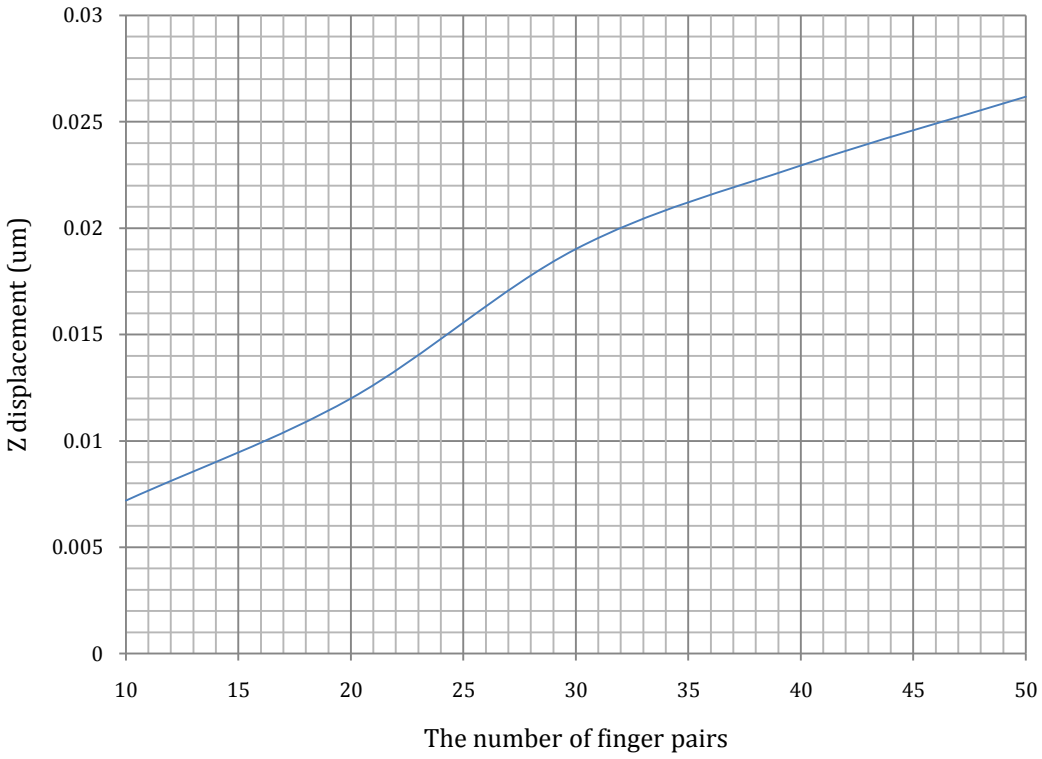

Figure 30: The maximum displacement in the Z axis versus finger pairs in Coventorware simulation.

Chapter 4 - Fabrications and Measurement of One-Pole Synchronous SAW Resonators

In this study, the SAW resonators in 121MHz and 978MHz are fabricated and measured on the 128^{o} YX $LiNbO_3$ wafers. The structures of SAW resonators, both single-track and dual-track IDTs as designed in Chapter 3 with shorted reflectors, were discussed in the previous chapter. The feature size of 121MHz and 978MHz SAW resonators are 8μm and 1μm respectively. These SAW resonators cannot be fabricated by using standard CMOS processes due to the piezoelectric substrates, and thus the microfabrication was carried out in the clean room to define the SAW resonator. The microfabrication process includes depositing, patterning and etching on the surface of substrates. The metal thin film was deposited and defined by the patterning process. The feature sizes in this work, 8μm and 1μm, are based on patterning technology, which uses a mask to define the portion that is unwanted. The detailed processes are illustrated and discussed in the following section.

After the resonators were fabricated, the measurements were performed directly on the wafer. The Vector Network Analyzer (8722D) was used to measure the frequency response at the output and was connected to the SAW resonators by the probe station. The probe station has ground-signal-ground (GSG) probe tips, which contact the metal pads on the wafer directly. The input and output of the resonators are connected to probe pads by metal traces. The measurement setup is shown in Figure 37 and discussed in the following section. The frequency responses of single-track and dual-track IDTs with shorted reflectors are measured and compared with the single-track IDT without shorted reflectors.

4.1. Microfabrication Processes on the Piezoelectric Wafers

Major process to define the SAW resonators on the 128^{o} YX $LiNbO_3$ wafers is Photolithography or optical lithography. This process transfers the pattern from the photo mask to light-sensitive photo resist by UV light. The pattern on the photo resist can be removed to expose the material underneath it. Two different etching processes, wet etching and dry etching, were adopted in fabrication. The wet etching process is easy to perform but has the disadvantage of sidewall-etching. Dry etching can remove the upper layer of the substrate in areas not covered by photo resist and is generally used to avoid undercutting beneath the photo resist pattern. All processes are illustrated in Figure 31.

Before photolithography was done, the masks were prepared according to the layouts. The layout of the SAW resonators was designed using the Cadence Design System and converting these to GDS files. The structures in the layout were covered by chrome on the quartz or soda-lime substrate. The layout of SAW resonators and 5" soda-lime mask are shown in Figure 32 and Figure 33. After the mask is prepared, an Aluminum thin film is deposited on the surface of the $LiNbO_3$ wafers. In the fabrication of SAW resonators, the thin-film was deposited on the surface and defined as interdigital transducers (IDT) structure. These IDTs provide electrical contacts of signals. These IDTs have to be light so that they do not dampen the surface acoustic wave. Aluminum has lower density than gold and is suitable metal for IDT structures. The thickness of the IDTs is usually between 500Å to 2000Å , however, the higher thickness of IDTs have lower resistance. Thus, the 2000Å aluminum thin-film is adapted in this work.

The $LiNbO_3$ wafers are very sensitive to changes in temperature. The wafer has a static charge on the surface and attaches to the metal surface when the temperature

increases to over 100^0F. Temperature differences would cause deformation and electrical charges on the wafers. It becomes a critical issue to heat the wafer in the deposition process. Denton E-beam evaporator is a tool used to deposit an Aluminum thin film constantly on the $LiNbO_3$ at room temperature. After the $LiNbO_3$ wafers were coated with a 2000 Å Aluminum thin film, they were defined the IDT structures by using the mask aligner. The mask aligner allowed UV light to shine through the photomask to expose the photo resist. The area covered by the chrome on the mask blocked the UV light and protected the photoresist from exposure. Patterns covered by chrome on the mask are translated onto the photo resist layer. Figure 31 shows the Denton E-beam evaporator and two different kinds of mask aligners. MJB-3 Mask Aligner is used for the 4-inch mask and 3-inch wafer. The resolution of the MJB-3 Mask Aligner is about 3 um in contact mode, which yields a minimum distance of 3um. Oriel Mask Aligner has a higher resolution, which can yield a feature size up to 1um. Figure 33 shows a STS dry etching system for a 4-inch wafer. In order to define 1um electrodes, the STS Etcher was adopted to avoid undercutting the photo resist pattern.

Figure 34 shows the structure for 121MHz SAW resonators where the electrodes are about 8um wide. Electrodes were slightly less than 8um and etched using a wet etching process. The error in electrodes due to the wet etching process can be tolerated, because the width of electrodes is much wider than the error of electrodes. This small difference in the width of the electrodes, however, will be relatively important if the width of the electrodes is 1um. To resolve this error, ICP system will be used to identify the electrodes producing vertical sidewall and avoiding the error in the electrodes' width.

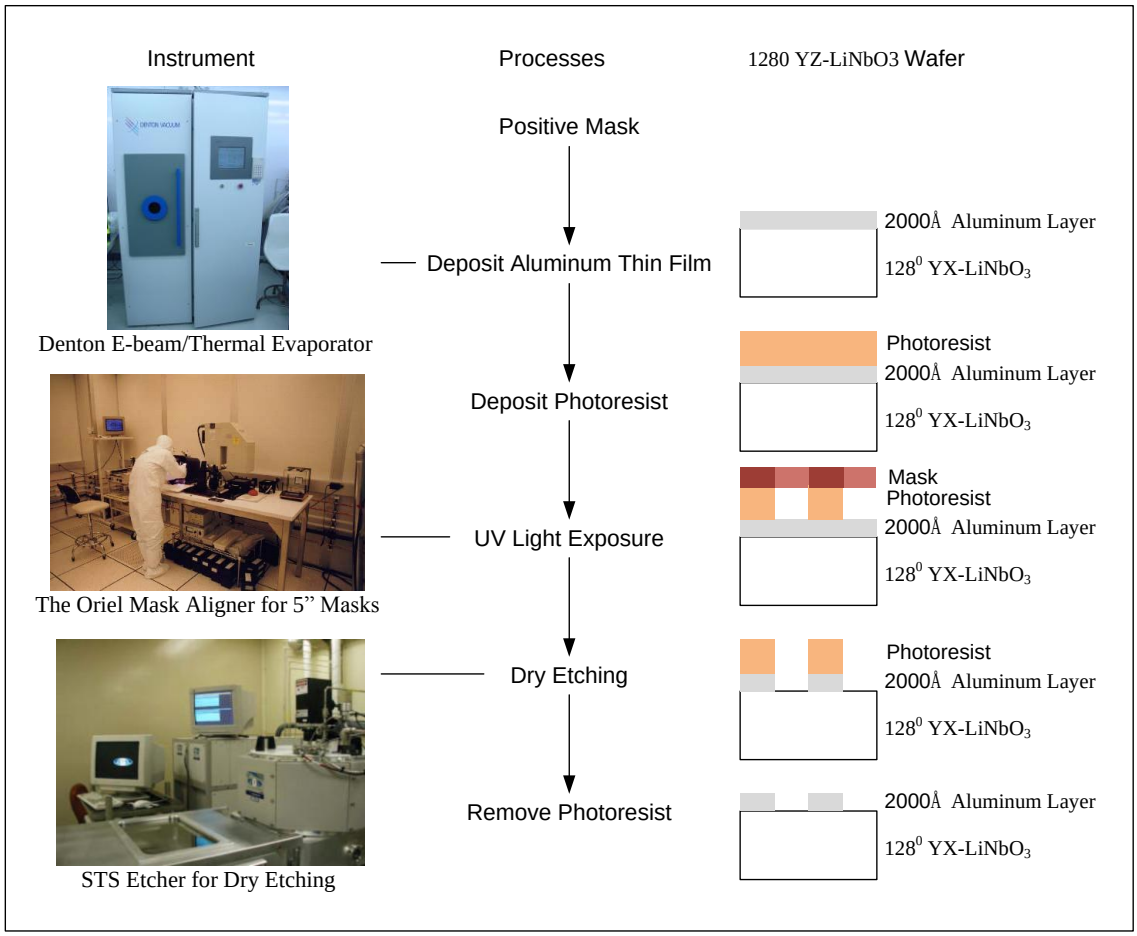

Figure 31: The processes of micro fabrication on the 4" 128° YX $LiNbO_3$ wafer. The cross view of wafers are illustrated.

The receipts and equipments of microprocesses are shown in Table 5. These receipts are not the same as standard CMOS processes. They are verified several times to define the best structure on the $LiNbO_3$ substrate; however, the $LiNbO_3$ substrate is highly sensitive to the temperature. Temperature effects are shown in Table 6. It is necessary to be careful during the processes involving the heating or cooling step.

Processes	Equipments	Recipes
Wet Etch	Etch Tunnel Acid / Solvent Bench	Heated Aluminum Etch: Phosphoric Acid/50^{o}/2 mins
Soft bake (AZ1813 Resist)	Baker	90^{o} / 1mins
E-Beam Evaporator (Aluminum Evaporation)	Denton E-beam / Thermal Evaporator	6.5 KV / 2E-6 torr / 5-20mins (depend on the current)
Dry Etch	Inductive Coupled Plasma (ICP)	Standard AlGaAs Recipe (SiCl4 and Ar at 1.5 mT and 350 watts)
UV light Exposure	EVG Mask Aligner	5 inch x 5 inch Masks plate / 4 inch Window
Remove the Resist	March Jupiter III O2 plasma system	>8 hrs

Table 5: The recipes of processes in the microfabrication

Processes	Temperature	Effects
Heating Rate	5^{o}C / minute	The electrostatics happens on the surface. The wafer might be shattered when temperature jumps too much.
Soft Bake	T≤90^{o}C	A good alternative baking processes is to bake in a convection oven for 20 minutes.
Hard Bake	T≤120^{o}C	The wafer breaks into pieces when the temperature is over 120^{o}C
Cooling		The wafer adheres to the metal. The wafer might be shattered due to thermal expansion.

Table 6: The temperature sensitivity of $LiNbO_3$ substrate

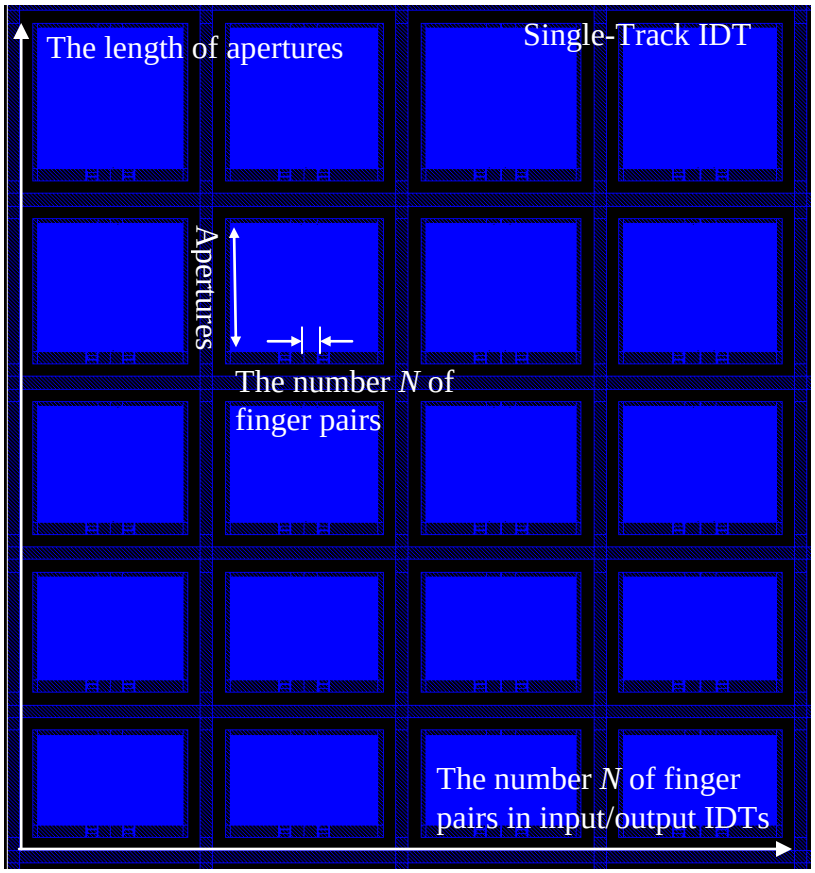

Figure 32: The layout of SAW resonators in Cadence. Different sizes of SAW resonators are designed on the 4" wafer.

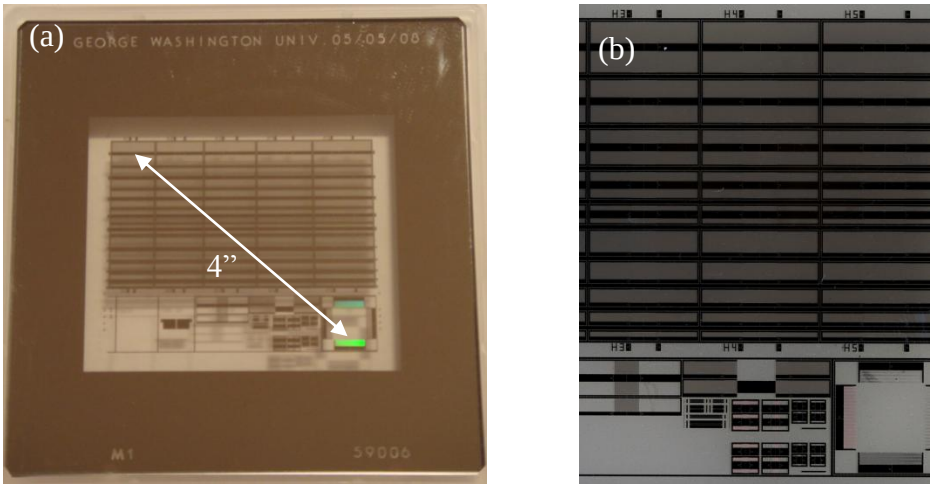

Figure 33: (a) The 5" Mask for the Lithography of 4" wafers. (b) The SAW structures on the 4" 128^0 YX-$LiNbO_3$ wafer.

Figure 34(a) shows the whole structures of the 121MHz single-track SAW resonator on the 128^0 YX-$LiNbO_3$ wafer, which has input/output IDTs and reflectors. Input/output IDTs are connected to the traces which have metal pads in the end. Measurements can be made by using probes to connect these pads directly on the wafers. The thickness of these electrodes is 2000Å and the structure of fingers is shown in Figure 34(b) and (c). Reflectors are half a wavelength away from the IDT. The wavelength λ is the distance between the two continuous electrodes and is equal to 8μm, which yield a center frequency f_o of up to 121MHz. The distance between electrodes is slightly larger than the width of the electrode. Electrodes in Figure 34(c) are slightly over etched by the wet etch process. Figure 35 shows the 121MHz SAW resonator diced from the wafer and connected to the SAW connectors.

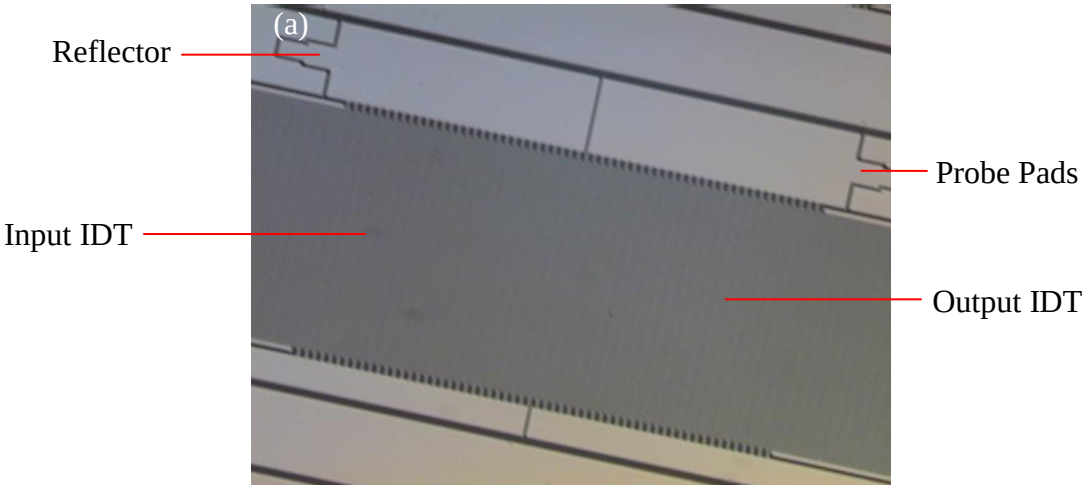

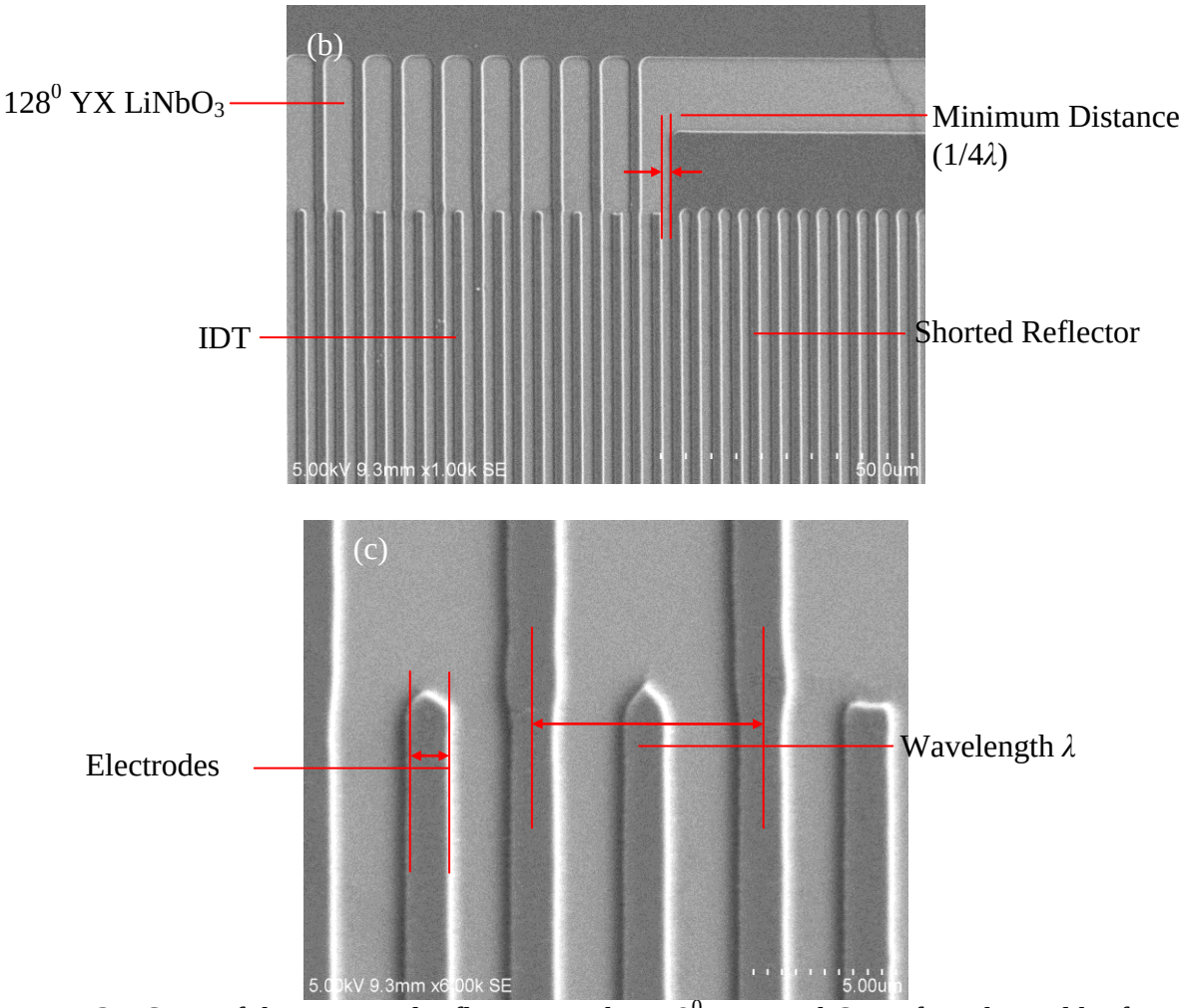

Figure 34: SEM of the IDTs and reflectors on the 128^0 YX-$LiNbO_3$ wafer. The width of electrodes is 8µm which yield a center frequency of up to 121MHz (a) Input/output IDTs with shorted reflectors (b) The minimum distance between the IDT and reflector. (c) The width of electrodes. The metallization is equal to 50%.

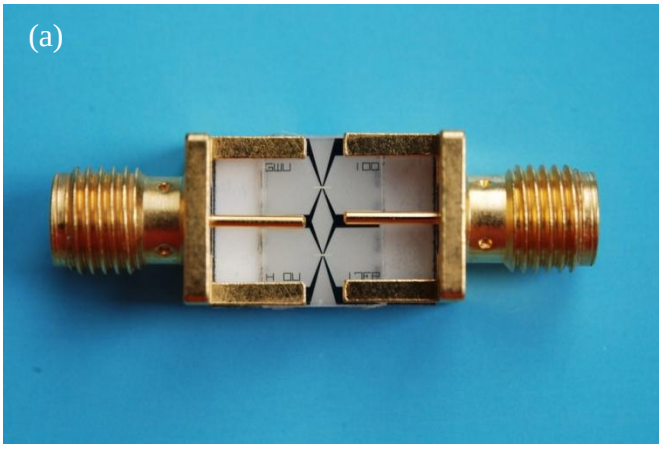

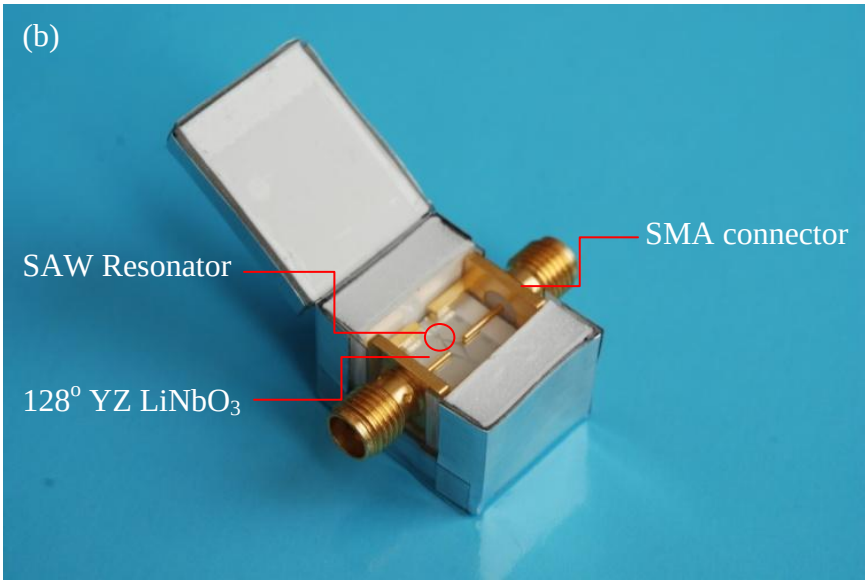

Figure 35: (a)(b)A one-pole synchronous SAW resonator with SMA connectors in the shield box.

4.2. S_{21} Measurement of 121MHz and 978MHz Resonators

Before measuring the frequency response, the network analyzer had to perform a calibration to eliminate the mismatch between the network analyzer and the chip. In order to increase measurement accuracy, the full two-port calibration had to be performed

before the measurements by using a 3.5mm broadband calibration tool kit. By using the full two-port calibration, including short, open, load and thru between input and output, mismatch and noise from the cables can be avoided. It also helps to define the Smith chart and increase the accuracy of frequency responses. The MicroTech Probe station shown in Figure 36 is used to perform the measurement directly on the wafer. The size of the contact pads on the RF Microwave Probe was about 70 um by 70 um and the separation between pads is 100um. The probe station was connected to the Network Analyzer by SMA cables. The calibration for the probe station and Network Analyzer had to be performed before the measurement by using Impedance Standard Substrates (ISS).

The measurement setup is shown in Figure 37. The through circuit was used to calibrate the parasitic effects in the transmission line. It was fabricated on the wafer with SAW resonators. As shown in Figure 38, the through circuit is designed next to the resonator in Cadence. The ground-signal-ground (GSG) probe pads for input and output probes are connected together. The distance between input and output pads is the same as the distance in the resonator.

(a)

(b)

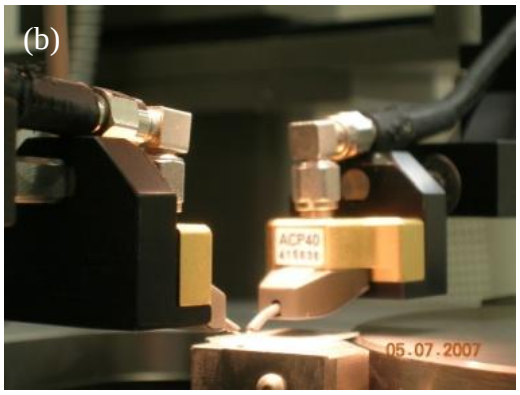

Figure 36: (a) RF Microwave Probe. (b) Calibrations for Network Analyzer through RF Microwave Probe. (c) Micro Tech Probe Station

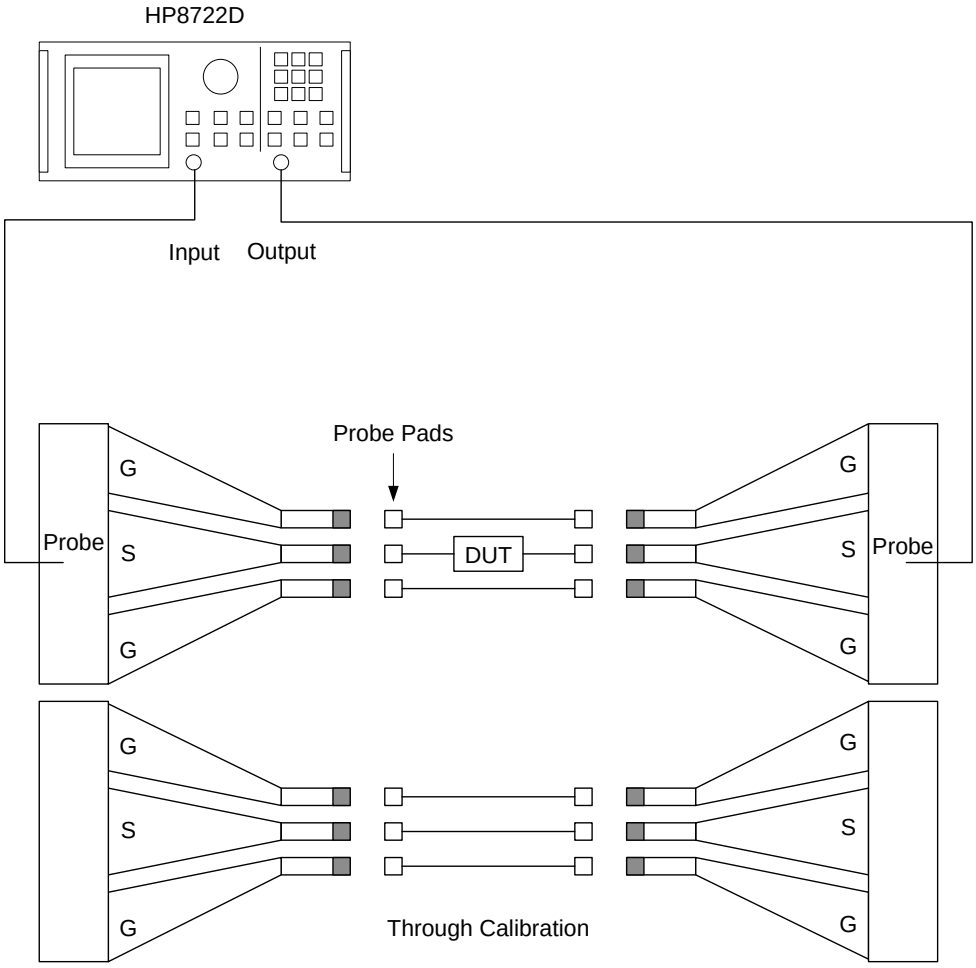

Figure 37: Measurement setup and calibration. The parasitic effects between the probe pads and network analyzer can be calibrated by the through circuit. The device under test (DUT) is a SAW resonator connecting to the probe pads.

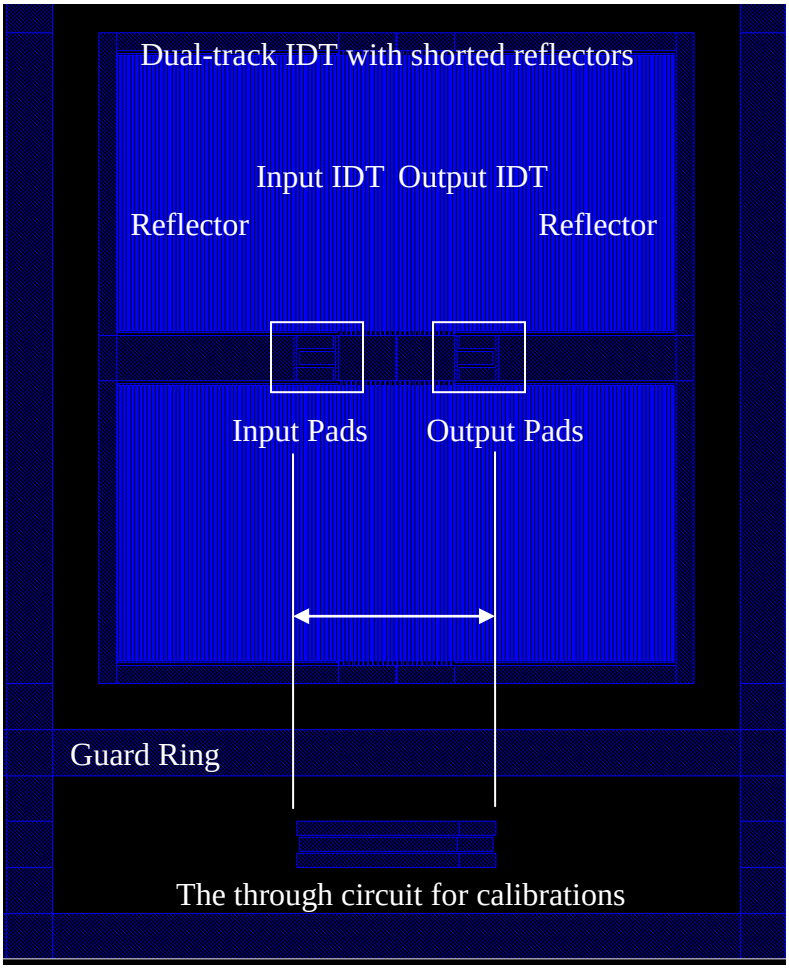

Figure 38: The layout of probe pads for the "through" calibration. The distance between input and output pads is the same as the calibration pads.

S_{11} and S_{22} are input and output reflection coefficients, and S_{12} and S_{21} are reverse and forward coefficients. The conversions from Y-parameters to S-parameters are shown in

the following equations. S_{21} represent the ratio of power received at the load to available power from the input source. It is also the insertion loss in the previous chapter.

$$S_{11} = \frac{(1-y_{11}Z_0)(1+y_{22}Z_0)+y_{12}y_{21}Z_0^2}{(1+y_{11}Z_0)(1+y_{22}Z_0)-y_{12}y_{21}Z_0^2} \quad \text{Equation 22}$$

$$S_{12} = \frac{-2y_{12}Z_0}{(1+y_{11}Z_0)(1+y_{22}Z_0)-y_{12}y_{21}Z_0^2} \quad \text{Equation 23}$$

$$S_{21} = \frac{-2y_{21}Z_0}{(1+y_{11}Z_0)(1+y_{22}Z_0)-y_{12}y_{21}Z_0^2} \quad \text{Equation 24}$$

$$S_{22} = \frac{(1+y_{11}Z_0)(1-y_{22}Z_0)+y_{12}y_{21}Z_0^2}{(1+y_{11}Z_0)(1+y_{22}Z_0)-y_{12}y_{21}Z_0^2} \quad \text{Equation 25}$$

The measurement setup is shown in Figure 39. It includes the probe station, network analyzer and 50 ohm cables. The $LiNbO_3$ wafer was placed in the center of probe station and observed through the microscope. SAW filters on the $LiNbO_3$ wafer were connected to the 8722D network analyzer by using probe tips as shown in Figure 40. After the probe tips connected to metal pads, the calibration (open, short, 50ohm and through) had to be performed to eliminate the mismatch. As shown in previous, through circuits were designed and fabricated next to the SAW structures on the wafer.

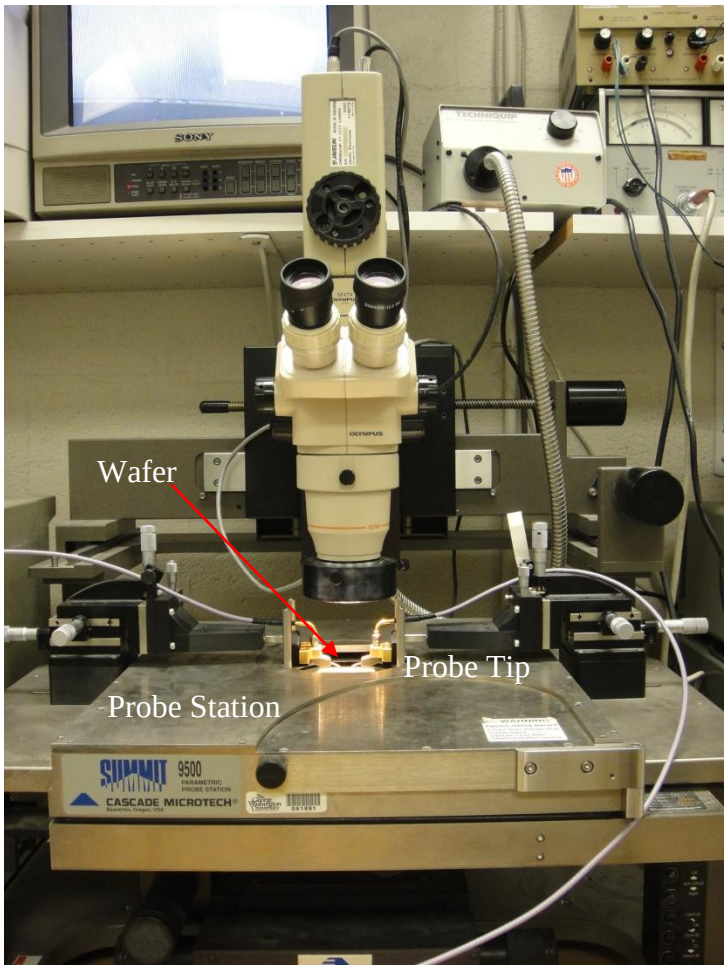

Figure 39: Direct measurement of SAW filters on the $LiNbO_3$. It shows the connections between the probe station and network analyzer. The ground-signal-ground (GSG) probe tips connect to the metal pads directly.

Figure 40: Probe tips on the $LiNbO_3$ wafer.

Figure 41 and Figure 42 show the frequency response of dual-track and single-track IDTs. The center frequencies are 121MHz and 978MHz respectively. In the absence of reflectors, the single-track IDT has wide band and two pole S21 response as shown in Figure 41 and Figure 42. With the shorted reflector included, there is an additional resonance superimposed on the center frequency. This additional resonance has 90^o phase shifts in the center frequency and a deep notch as discussed in Chapter 3. It is a one-pole response which has a higher IL and Q factor in comparison with the frequency response of the single-track IDT without shorted reflectors. The frequency response of dual-track and single-track IDTs are also shown. The out-of-band rejection is improved slightly by

connecting two single-track IDTs in parallel, as discussed in the previous chapters. The dual-track IDT also has a better insertion loss and Q factor in comparison with the single-track IDT. The insertion loss of the dual-track IDT with shorted reflectors is -3.1dB in the 121MHz center frequency and the Q factor is 192.42. The insertion loss of the dual-track IDT with shorted reflectors in 978MHz is -2.8dB and the Q factor is 412.59.

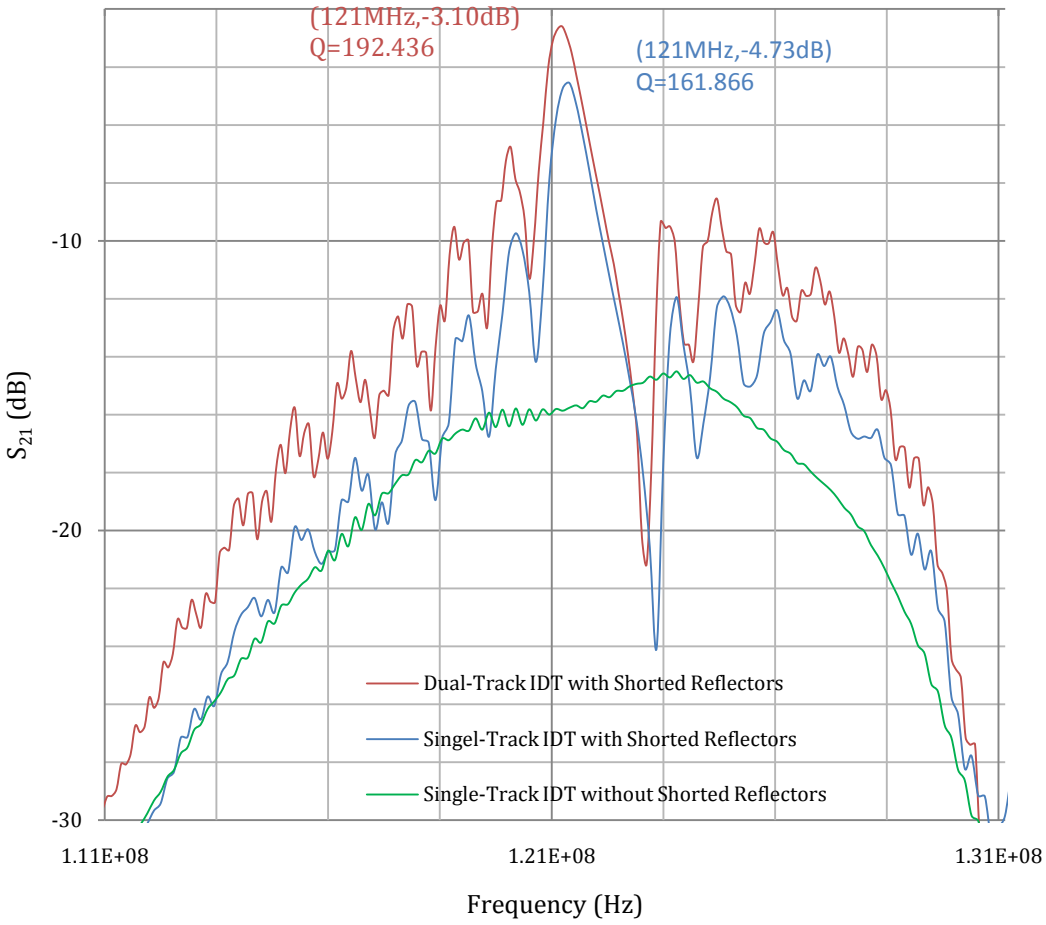

Figure 41: Frequency response of 121MHz SAW resonators. The single-track SAW resonator without shorted reflectors has a two-pole response. With shorted reflectors included, a one-pole resonance with 90^{o} phase shift is superimposed in the center frequency.

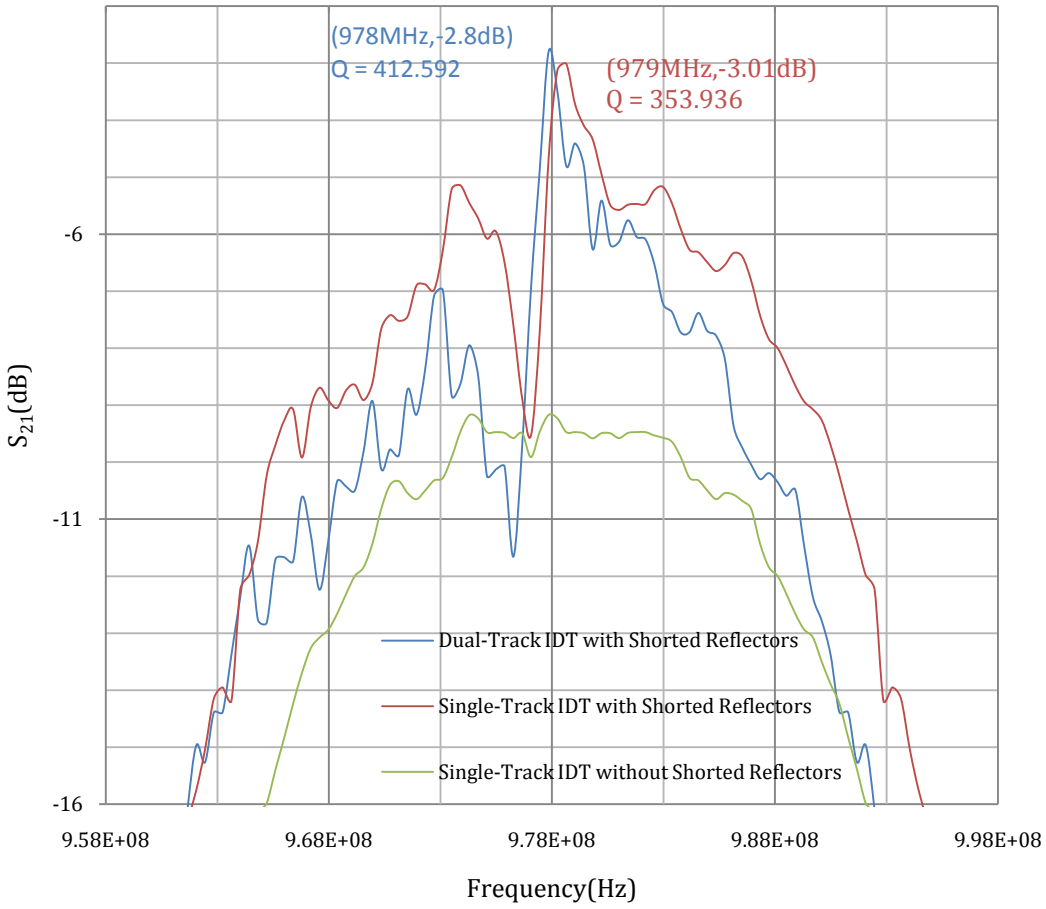

Figure 42: Frequency response of 978MHz SAW resonators. The dual-track SAW resonator has -2.8 dB insertion loss. The dual-track IDT with shorted reflectors has a better stop band rejection than the single-track IDT.

Chapter 5 - The Application of One-Pole Synchronous SAW Resonators for Mass Sensors

The purpose of this chapter is to explain the development of the low-loss single-pole SAW resonator for sensing applications. The 128^o YX LiNbO3 has the advantages of a high K^2 (5.3%) and velocity-shift coefficient K_{11m}, which is the coefficient of velocity shift due to the mass-loading effect on the electrode. The higher K_{11m} yields larger frequency shifts and mass sensitivities, which is easier to observe in the output IDT [1][2]. The high K^2 material, like 128^0 YX $LiNbO_3$, can also yield a higher IL in comparison with the same SAW structure on other piezoelectric materials. The disadvantage of the standard SAW device on 128^o $LiNbO_3$ substrate, is wide band response as shown in Figure 41 and Figure 42. The bidirectional IDTs not only has a low Q factor, but also a two-pole resonance as shown in Figure 41 and Figure 42. This two-pole resonance with the low insertion loss implies the difficulties in determining the center frequency and frequency shift. The improvement of the Q factor and one-pole response can make it easier to observe the frequency shift and increase the sensitivity for mass sensor applications. To achieve this one-pole frequency response, the SAW resonator was designed based on the distance parameters and shorted reflectors as shown in Figure 20. The reflecting acoustic waves in the output IDT result in an additional one-pole superimposed resonance as shown in Figure 41 and Figure 42. It is easier to find its center frequency and frequency shift from this one-pole frequency response which has a maximum IL in the center frequency. The Q factor and IL are also improved in comparison with the bidirectional IDTs. The One-Pole Synchronous SAW Resonators in this work have the following advantages for sensing application [39]-[43]:

(1) It has a one-pole S_{21} response with the maximum IL in the center frequency to read the signal.

(2) It has high IL so that it does not need the amplifiers or attenuators;

(3) It has a smaller size than delay line SAW sensors, because there is no quadrate sensing area between input and output IDTs.

In this work, the dual-track IDT SAW resonator is used as a mass sensor, which has a clear and repeatable frequency shifts. The frequency shift and sensitivity can be determined by its one-pole resonance where it has the maximum IL. It also has a low loss response and high mass sensitivity (1.315×10^{11} Hz·mm^2/g) in comparison with a delay-line SAW mass sensor (1.24×10^{9} Hz·mm^2/g).

5.1. The Structure of One-pole Synchronous SAW Mass Sensors

The structures of the one-pole synchronous SAW resonators are shown in Figure 43. There are two types of structures examined in this work: the single-track and dual-track IDT with synchronous reflectors. These two structures are examined and compared in the frequency response. According to the results in the previous chapter, the out-of-band rejection and shape factor can be improved by the dual-track IDT structure. The maximum insertion loss in the main lobe of resonance can have more side lobe rejection as shown in Figure 41 and Figure 42. Figure 43 also shows that the output IDT is placed with the minimum distance ($d_g = \lambda/2$) next to the input IDT. This optimal minimum distance can avoid the propagating loss in the acoustic transmission line between IDTs. The reflectors are also placed symmetrically next to the input and output IDTs. The

acoustic wave pattern in Figure 43 shows that the strips of reflectors are placed in the optimal positions outwards from the minimum close-in position ($d_r = \lambda/2$). The reflectors can have the maximum reflectivity when the strips are placed synchronously on the acoustic wave pattern. Furthermore, the strips in reflectors are connected together as "shorted reflectors." These shorted reflectors can have a lager reflection coefficient than the unshorted reflectors. The reflection coefficient is nearly 100% when there are more than 15 electrodes in reflectors.

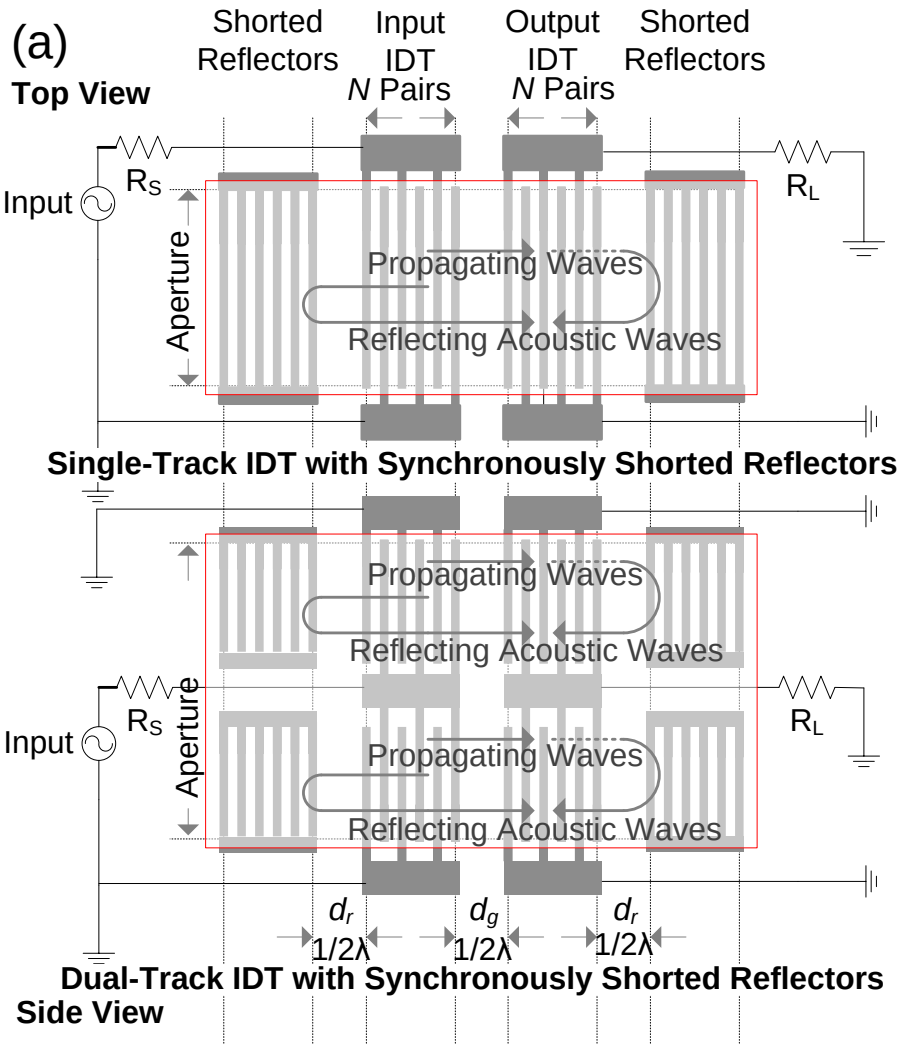

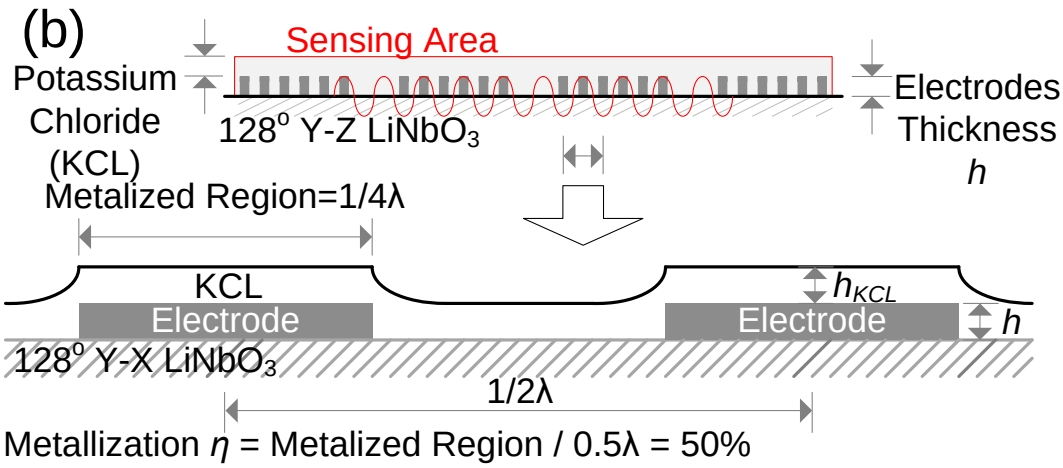

Figure 43: (a) The geometry of single-track and dual -track SAW resonators. The synchronous shorted reflection gratings are placed 1/2λ out from the IDTs symmetrically. The sensing area includes input /output IDTs and reflectors. (b) Sensing Area and metalized region of the SAW mass sensor.

The configuration of measurements is shown in Figure 44. The mass sensors are connected to the network analyzer to examine the frequency shifts. The mass is dropped on the sensing area which covers the input/output IDTs and reflectors. This additional mass affects the velocity and center frequency of acoustic waves. In order to examine the frequency shifts of mass sensors, a chemical compound potassium chloride (KCL) is deposited on the surface. The purpose of the experiment is to place small mass on the surface of SAW mass sensors. For this purpose, the potassium chloride (KCL) solution was chosen. The detail steps of measurement are in section 5.4. The KCL in Figure 45 has easily reproducible and repeatable measurable properties. The 4ul KCL solutions were dropped onto the sensing area using a pipette. After the solvent evaporates, the KCL remains on the surface with a uniform thin film. This KCL thin film has a small mass on the electrodes and causes the center frequency to shift. In this work, different

concentrations (from 3×10^{-5}M to 3×10^{-3}M) of KCL solutions were used to measure the mass sensitivity of mass sensors. According to the results, the one-pole synchronous SAW mass sensor has a high sensitivity and good linearity (1.32 e^{11} Hz·mm^2/g).

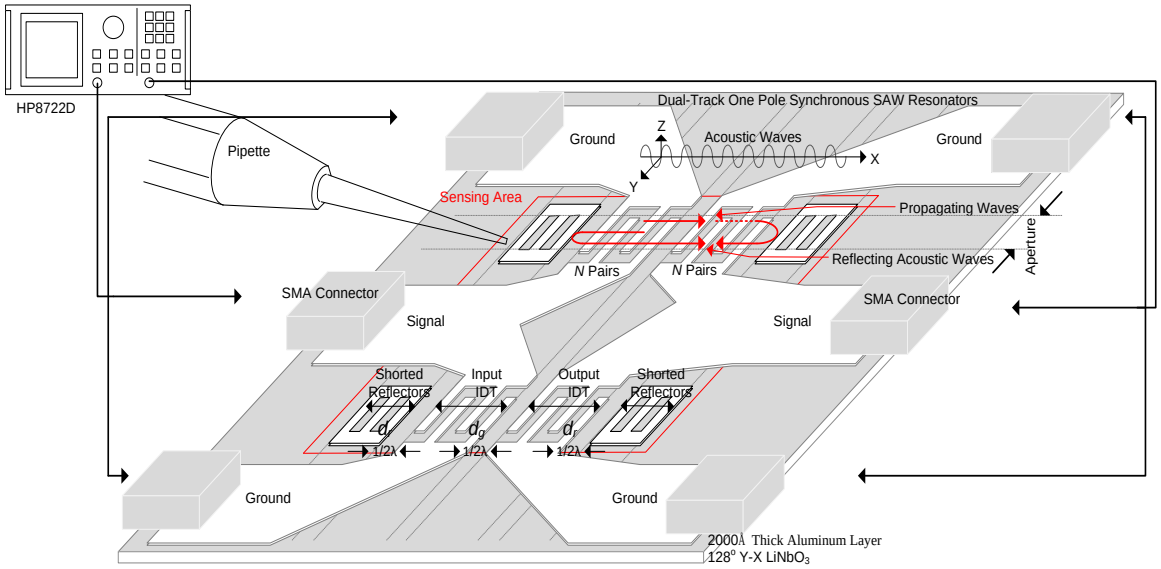

Figure 44: The configuration and measurement of mass sensors. The sensing area covers the input /output IDTs and reflectors.

Potassium Chloride (KCL)

Molecular Mass: 74.551 g/mol

Density: 1.984 g/cm^3

Crystal Structure: face centered cubic

Solubility of KCL in 100g H_2O at 25°C: 36g

Figure 45: Material properties of Potassium Chloride (KCL).

5.2. The Velocity and Frequency Shifts of Mass Sensors

The acoustic waves are excited by electrical signals in the input IDT, however, the mass of electrodes in IDTs dampen these acoustic waves. It affects the velocity and amplitude of acoustic waves. The SAW velocity on the free space can be reduced when it is under the IDT. This reduction also decrease the radiation conductance $G_a(f)$ and center frequency f_o. Both are important factors for determining the IL in the output IDT.

According to the material properties of 128° YX-$LiNbO_3$, the fractional velocity decrease $\frac{\Delta V}{V}$ can be expressed as Equation 26 in terms of $\frac{h}{\lambda}$, which represents the film-thickness ratio, where h is the thickness of electrodes and λ is the acoustic wavelength. k_{11p}, k_{11m} and k_{11s} are velocity-shift coefficients which are three important factors of velocity shifts [1][39]-[43]. This first term $\left[\frac{\Delta v}{v}\right]_p$ is the velocity shift due to the shorting piezoelectric fields in the metalized regions. In this work, the metallization is equal to 50% so that the metalized region is equal to $\frac{\lambda}{4}$. The second term $\left[\frac{\Delta v}{v}\right]_m$ is the velocity shift due to the loading mass on the metalized region. It can be expressed as k_{11m} and the film-thickness $\frac{h}{\lambda}$. When the aluminum electrodes are deposited, the mass of electrodes decreases the acoustic velocity and center frequency. When the KCL is deposited, the center frequency decreased further. The third term $\left[\frac{\Delta v}{v}\right]_s$ is related to the effective stiffness of the propagating surface when the metal electrodes are deposited on the piezoelectric substrate. The total velocity shifts are calculated from these three terms which can be expressed in term of three important parameters k_{11p}, k_{11m} and k_{11s}. The differential equation of acoustic velocity in Equation 26 is expressed in terms of the

exponential function of film-thickness ratio $\frac{h}{\lambda}$ [1][2]. If the film-thickness ratio $\frac{h}{\lambda}$ is less than 1%, the exponential function of film-thickness ratio $\frac{h}{\lambda}$ is approximate to film-thickness ratio $\frac{h}{\lambda}$ as shown in Equation 27. The frequency changes can be further derived in Equation 28. If there is additional mass deposited on the electrodes, the frequency shifts further as shown in Equation 29. However the frequency shift does not have a linear relation to the additional mass Δm on the electrodes. It can be linear only when the third term of k_{11s} is zero. According to the properties in Table 7 [1][2], 128° YX-$LiNbO_3$ has a zero k_{11s} and high $k_{11m.}$ It implies a linear equation with the large frequency shift when additional mass is on the electrodes. Based on these properties, Equation 30 shows the linear relation between the frequency shift and additional mass on 128° YX-$LiNbO_3$ substrate.

If there is additional mass deposited uniformly on the electrodes, as shown in Figure 43, this additional mass causes additional shifts in the velocity and center frequency. This chapter focuses on the applications of SAW resonators in sensing the additional mass on the surface. Equation 31 shows the frequency shift due to the additional mass on the electrodes. Δm and A_s are the total additional mass on the sensing area. If the KCL is used to examine the frequency shift, the additional mass Δm can be translated into the concentration and volume of the KCL solution($MW_{KCL} \times M \times \Delta V$). The sensitivity of mass sensors can be expressed as the frequency shifts divided by the mass density ρ $\left(\rho = \frac{\Delta m}{A_s}\right)$.

Velocity perturbation

$$\left[\frac{\Delta v}{v}\right]$$

$$= \left[\frac{\Delta v}{v}\right]_p + \left[\frac{\Delta v}{v}\right]_m \times \left(0.0158 \times \left(1 - e^{-\frac{\frac{h}{\lambda}}{0.01}}\right)\right) + \left[\frac{\Delta v}{v}\right]_s \times \left(0.0158 \times \left(1 - e^{-\frac{\frac{h}{\lambda}}{0.01}}\right)\right)^2$$

$$= k_{11p} + k_{11m} \times \left(0.0158 \times (1 - e^{-\frac{\frac{h}{\lambda}}{0.01}})\right) + k_{11s} \times \left(0.0158 \times (1 - e^{-\frac{\frac{h}{\lambda}}{0.01}})\right)^2$$

Equation 26

if $\frac{h}{\lambda} \ll 0.01$

$$\left[\frac{\Delta v}{v}\right] = k_{11p} + k_{11m} \times \left(0.0158 \times (1 - e^{-\frac{\frac{h}{\lambda}}{0.01}})\right) + k_{11s} \times \left(0.0158 \times (1 - e^{-\frac{\frac{h}{\lambda}}{0.01}})\right)^2$$

$$\approx \left[\frac{\Delta v}{v}\right]_p + \left[\frac{\Delta v}{v}\right]_m \times \left(\frac{h}{\lambda}\right) + \left[\frac{\Delta v}{v}\right]_s \times \left(\frac{h}{\lambda}\right)^2$$

$$\approx k_{11p} + k_{11m} \times \left(\frac{h}{\lambda}\right) + k_{11s} \times \left(\frac{h}{\lambda}\right)^2$$ Equation 27

$$\Delta f = \frac{v}{\lambda} \times \left[k_{11p} + k_{11m} \times \left(\frac{h}{\lambda}\right) + k_{11s} \times \left(\frac{h}{\lambda}\right)^2\right]$$ Equation 28

Frequency shifts due to electrodes and the additional mass

$$\Delta f = \frac{v}{\lambda} \times \left[k_{11p} + k_{11m} \times \left(\frac{h+h_{kcl}}{\lambda}\right) + k_{11s} \times \left(\frac{h+h_{kcl}}{\lambda}\right)^2\right]$$

$$= \frac{v}{\lambda} \times \left[k_{11p} + k_{11m} \times \left(\frac{h}{\lambda} + \frac{h_{kcl} \times A_s}{\lambda \times A_s}\right) + k_{11s} \times \left(\frac{h}{\lambda} + \frac{h_{kcl} \times A_s}{\lambda \times A_s}\right)^2\right]$$

$$= \frac{v}{\lambda} \times \left[k_{11p} + k_{11m} \times \left(\frac{h}{\lambda} + \frac{\Delta V}{\lambda \times A_s}\right) + k_{11s} \times \left(\frac{h}{\lambda} + \frac{\Delta V}{\lambda \times A_s}\right)^2\right]$$

$$= \frac{v}{\lambda} \times \left[k_{11p} + k_{11m} \times \left(\frac{h}{\lambda} + \frac{\Delta m}{\lambda \times A_s \times D_{Al}} \right) + k_{11s} \times \left(\frac{h}{\lambda} + \frac{\Delta m}{\lambda \times A_s \times D_{Al}} \right)^2 \right]$$

$$= \frac{v}{\lambda} \times \left[k_{11p} + k_{11m} \times \left(\left(\frac{h}{\lambda} \right) + \frac{1}{\lambda D_{Al}} \times \frac{\Delta m}{A_s} \right) + k_{11s} \times \left(\left(\frac{h}{\lambda} \right) + \frac{1}{\lambda D_{Al}} \times \frac{\Delta m}{A_s} \right)^2 \right]$$

Equation 29

For 128° YX-$LiNbO_3$, $k_{11p} = 0.022$, $k_{11m} = 0.091$, $k_{11s} = 0$, refer to Table 7.

$$\Delta f = \frac{v}{\lambda} \times \left[k_{11p} + k_{11m} \times \left(\left(\frac{h}{\lambda} \right) + \frac{1}{\lambda D_{Al}} \times \frac{\Delta m}{A_s} \right) \right]$$

$$= \frac{v}{\lambda} \times k_{11p} + \frac{v}{\lambda} \times k_{11m} \times \left(\frac{h}{\lambda} \right) + \frac{v}{\lambda} \times k_{11m} \times \left(\frac{1}{\lambda D_{Al}} \times \frac{\Delta m}{A_s} \right)$$

$$= constant + \ constant + \frac{v}{\lambda} \times k_{11m} \times \left(\frac{1}{\lambda D_{Al}} \times \frac{\Delta m}{A_s} \right)$$

Frequency shifts due to additional mass,

$$\Delta f = \frac{v}{\lambda} \times \frac{k_{11m}}{\lambda D_{Al}} \times \frac{\Delta m}{A_S}$$

Equation 30

Frequency shifts due to additional KCL film

$$\Delta f = \frac{v}{\lambda} \times \frac{k_{11m}}{\lambda D_{Al}} \times \frac{MW_{KCL} \times M \times \Delta V}{A_S}$$

Equation 31

Mass sensitivity

$$S_m^f = \frac{\Delta f}{\rho} = \frac{v}{\lambda} \times \frac{k_{11m}}{\lambda D_{Al}}$$

Equation 32

, where

v velocity of acoustic waves on the free space

λ wavelength of acoustic waves

h	thickness of electrodes
Δv	velocity shift
Δf	frequency shift
k_{11p}	velocity-shift coefficient due to shorted metalized region
k_{11m}	velocity-shift coefficient due to the mass
k_{11s}	velocity-shift coefficient due to stiffness
D_{Al}	density of Aluminum electrodes
Δm	mass on the electrodes
A_S	sensing area
MW_{KCL}	molecular weight of KCL
M	concentration of KCL solution
ΔV	volume of KCL solution
S_m^f	mass sensitivity
ρ	mass density

Based on Equation 26 and Equation 30, the frequency shifts are simulated in Figure 46 by using MATLAB. According to previous theoretical equations, the frequency shifts is approximately linear curves if the film-thickness ratio h/λ is less than 0.01. This ratio h/λ can also imply the linear region of frequency shifts and maximum detectable mass in this theoretical model. As shown in Figure 46, the maximum detectable mass densities are 10.8×10^{-8} g/mm^2 and 86.4×10^{-8} g/mm^2, for 978MHz SAW mass sensors and 122MHz SAW mass sensors respectively.

(a)

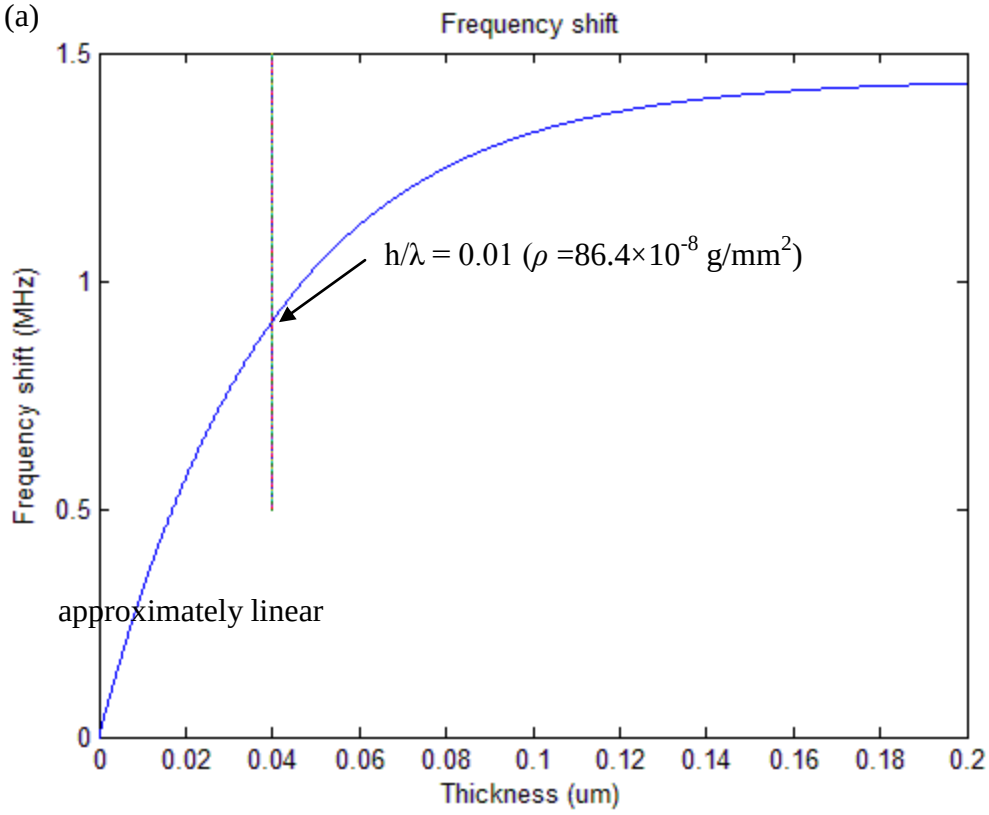
Frequency shift
Frequency shift (MHz)
Thickness (um)
h/λ = 0.01 (ρ =86.4×10^-8 g/mm^2)
approximately linear
0
0.5
1
1.5
0.02
0.04
0.06
0.08
0.1
0.12
0.14
0.16
0.18
0.2

(b)

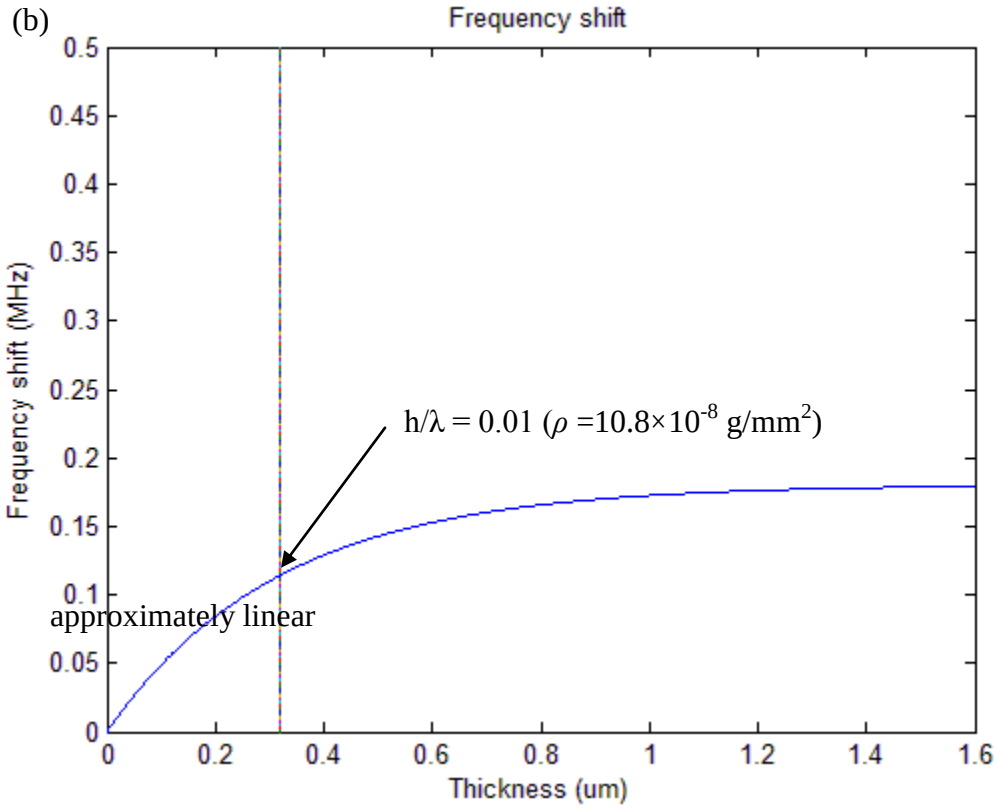
Frequency shift
Frequency shift (MHz)
Thickness (um)
h/λ = 0.01 (ρ =10.8×10^-8 g/mm^2)
approximately linear
0
0.05
0.1
0.15
0.2
0.25
0.3
0.35
0.4
0.45
0.5
0.2
0.4
0.6
0.8
1
1.2
1.4
1.6

Figure 46: The frequency shift versus different thickness of the mass on the electrodes. Base on Equation 26, the frequency shifts are linear to the thickness of mass approximately when the film-thickness ratio h/λ is less than 0.01. (a) 122MHz SAW mass sensor (b) 978MHz SAW mass sensor

Table 7 [1][2]shows the parameters of common piezoelectric materials, including their velocity-shift coefficients. 128^o YX-$LiNbO_3$ is the piezoelectric material with the highest velocity v and electromechanical coupling K^2. 128^o YX-$LiNbO_3$ also has a high k_{11m} so that it is highly sensitive in the mass. Its properties of zero k_{11s} and high k_{11m} can yield a linear relation between the mass and frequency shifts, which are important for sensing applications. The IDT structures in the previous section are used to achieve the one-pole low-loss SAW resonators for sensing applications. The characteristic of one-pole and low loss can make the center frequency to be observed easily in the output IDT. Based on Equation 31, the theoretical calculation of mass sensitivities in 121 and 978MHz are shown in Table 8

Substrate	ST-X Quartz	YX-$LiNbO_3$	128^o YX-$LiNbO_3$	64^o YX-$LiNbO_3$	36^o YX-$LiTaO_3$
SAW velocity v_o (m/s)	3158	3488	3997	4742	4212
Axis	X	Z	X	X	X
Electromechanical coupling coefficient K^2	0.0016	0.045	0.056	0.113	0.047
C_o Capacitance/ finger pair/unit length (pF/cm)	0.503	4.5	5.0	_	_
k'_{11p}	0.0004	0.018	0.022	0.052	0.0076
k'_{11m}	0.02(h/λ)	0.3(h/λ)	0.091(h/λ)	0.18(h/λ)	0.0011(h/λ)
k'_{11s}	7.9$(h/\lambda)^2$	_	_	1.4$(h/\lambda)^2$	3.6$(h/\lambda)^2$
TCD (ppm/^{o}C)	≈ 0	94	75	70	35
k'_{12p}	0.0001	0.0054	0.0064	0.0091	0.0069

k'_{12m}	0.16(h/λ)	0.08(h/λ)	0.14(h/λ)	0.48(h/λ)	0.12(h/λ)
k'_{12s}	_	_	_	_	2.8$(h/\lambda)^2$
Wave Type	Rayleigh wave	Rayleigh wave	Rayleigh wave	Leaky SAW	Leaky SAW

Table 7: The parameters of piezoelectric substrates based on the 50% Aluminum metallization and shorted reflectors. h is the thickness of electrodes and λ is the wavelength of acoustic waves.

v (m/s)	λ(m)	k_{11m}	D_{Al} (g/m^3)	S_m^f(Hz·mm^2/g)
3997	3.20e^{-5}	0.091	2.7e^6	1.32e^{11}
3997	4.00e^{-6}	0.091	2.7e^6	8.42e^{12}

Table 8: Theoretical Calculation of Mass Sensitivities (S_m^f) of 121MHz and 978MHz SAW mass sensors.

5.3. Simulation of the Mass on the Surface

The mass sensors in Figure 43 were simulated by using Coventorware. The KCL film was deposited on the sensing area which includes the input/output IDTs and reflectors. A 3D model of the mass sensors is shown in Figure 47 and the top layer is the KCL film. In the Coventorware simulation, the acoustic waves propagate between the KCL film and substrates, but the waves are affected by the mass of KCL films. These effects directly cause the center frequency of the acoustic waves to decrease. In Figure 48, the frequency shifts are simulated in related with the thickness of KCL films. The mass of KCL films is in direct proportion to the thickness of KCL films. According to the simulation results, the frequency shift increases linearly when the thickness increases.

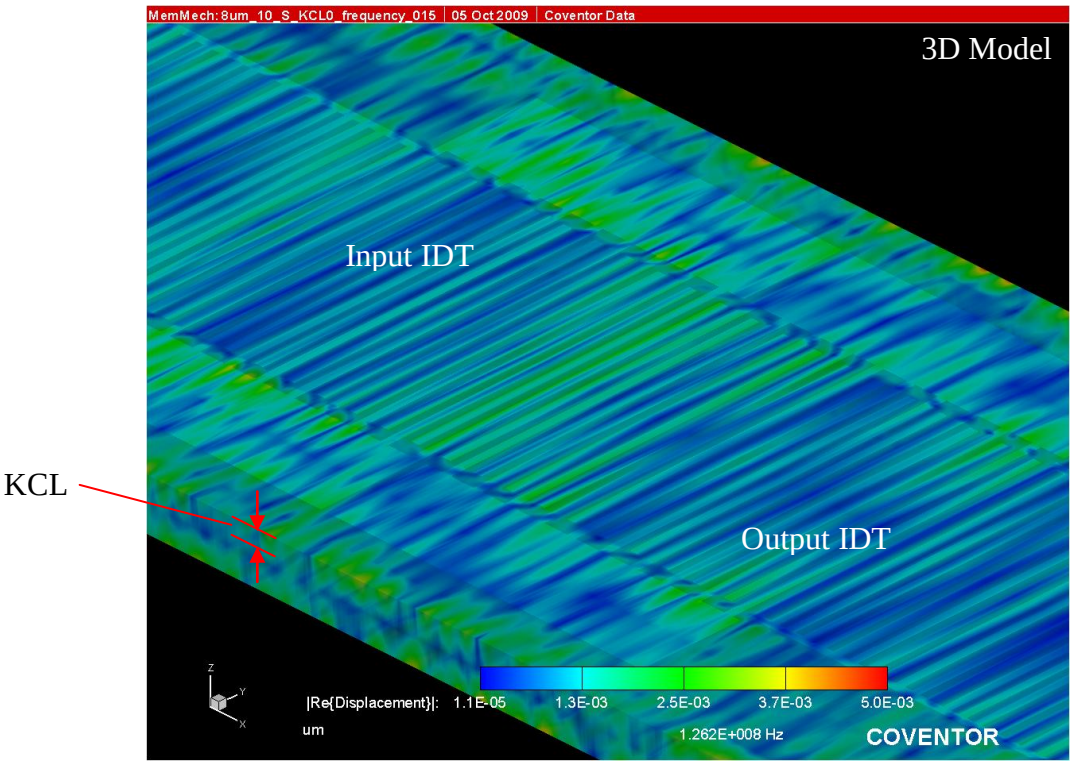

Figure 47: The 3D model of the SAW resonator in Coventorware . The displacements are shown when the acoustic waves propagate from input IDT to output IDT. The center frequency f_o changes with the different thicknesses of KCL (h_{KCL}).

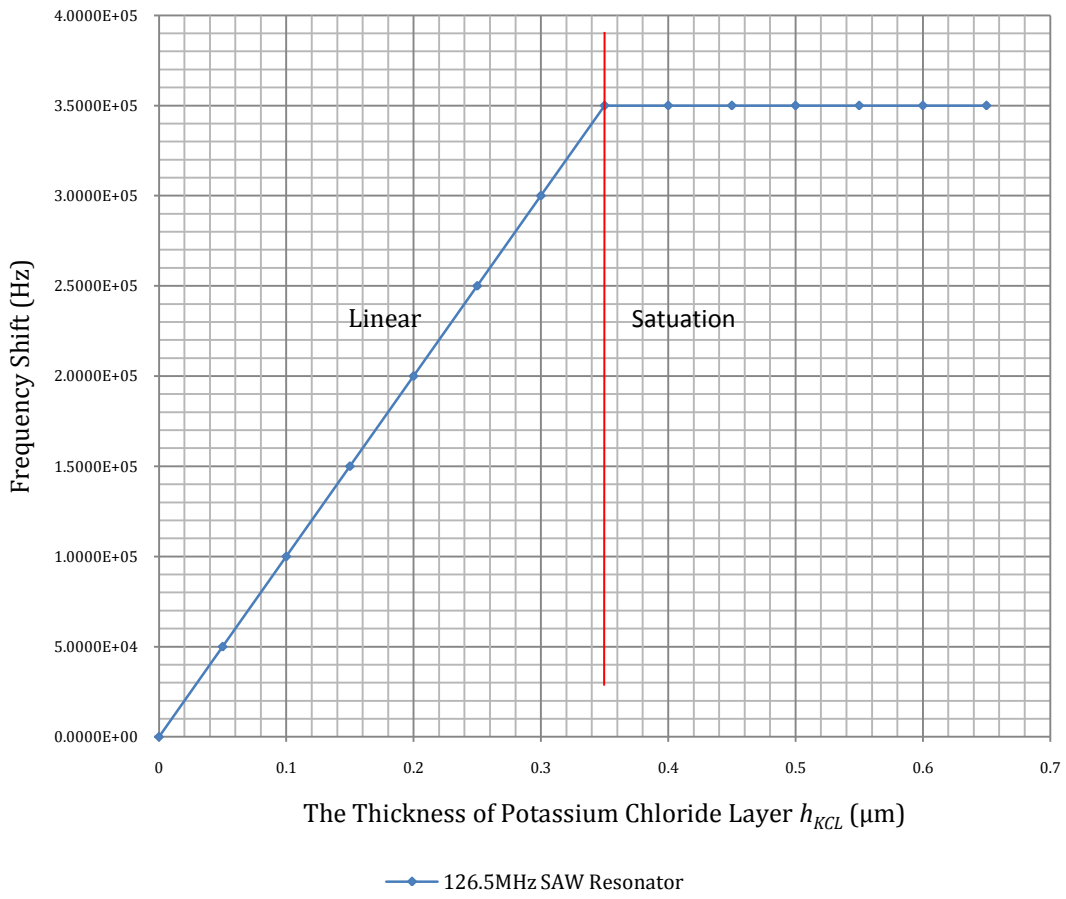

Figure 48: The Coventorware simulation of frequency shifts when the different thicknesses of KCL are deposited on the surface. It shows the linear region when the thickness of KCL is less than 0.3µm.

5.4. The Measurement of Frequency Shifts and Mass Sensitivities

The configuration of measurements is shown in Figure 44. The KCL solutions, in different concentration, were dropped in the sensing area using a pipette. The $LiNbO_3$ is sensitive to temperature variance and a 1 ^oC temperature difference can make a 9 KHz frequency shift, so it was important to keep the temperature stable during the measurement. All measurements in this work were done in room temperature and

operated in the isolated chamber as shown in Figure 49. The temperature in the chamber is monitored by using an IR thermometer. Because there were no heating or cooling processes during depositions of KCL films, the temperature variance was less than 0.1^{o}F (the minimum scale of IR thermometer). The original center frequency f_o before depositing KCL films was examined again after washing out the KCL film. The steps used in the measurement of the KCL films were as follows: (1) the SAW resonator was connected to the network analyzer to measure the center frequency; (2) the 4ul KCL solution was dropped onto the sensing area and left on the surface for 15 minutes; (3) the frequency shift due to the additional KCL film on the electrodes was measured; (4) the KCL film on the surface was washed out and the center frequency was measured again. This last step was done to verify the original center frequency in the first step. If there were influences from temperature changes, the original center frequency could not be measured in step (4). Based on these measurement steps, Figure 50 and Table 9 shows the different frequency responses when different masses of KCL films were deposited on the surface. The mass of the KCL film not only decreased the velocity, but also the amplitude of the acoustic waves. When the $2.43e^{-6}$ g/mm^2 KCL film is deposited, the center frequency f_o and IL decrease in comparison with the frequency response without the KCL film. This decrease is the frequency shift Δf due to the KCL film.

Concentration (M)	Mass density (g/mm^2)	Frequency shifts
0.0047	$1.52e^{-7}$	0.02
0.0094	$3.04e^{-7}$	0.04
0.0188	$6.08e^{-7}$	0.08
0.0375	$1.22e^{-7}$	0.15
0.075	$2.43e^{-7}$	0.245
0.15	$4.86e^{-7}$	0.305
0.3	$9.73e^{-7}$	0.305

Table 9: The mass density versus frequency of 121M Hz SAW mass sensors

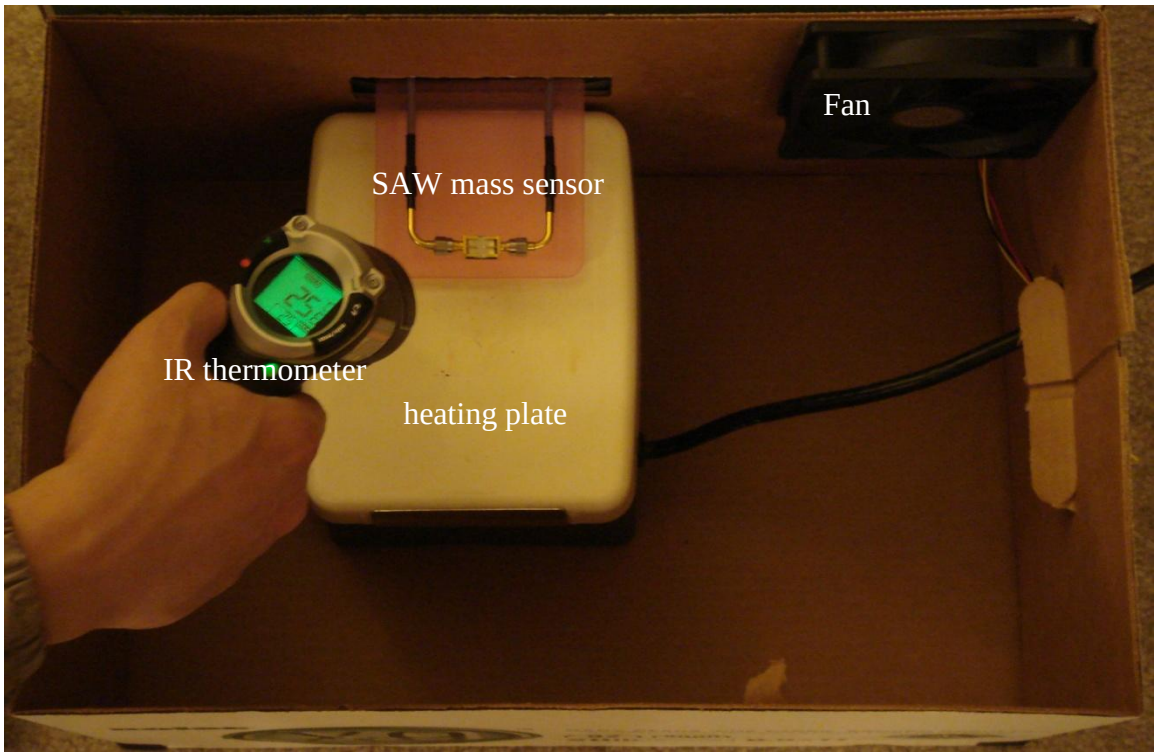

Figure 49: The measurement setup includes the heating plate and fan. The heating plate and fan are used to keep temperature stable. The temperature is monitored by the IR thermometer.

The curves of mass sensitivity in Figure 43 can be obtained by measuring the frequency shifts from low concentration to high concentration. In Figure51, there are two mass sensors which operate 121MHz and 978MHz. The minimum detectable mass of sensors in 121MHz is 152.1 ng/mm^2 with 0.02 MHz frequency shift which yields a mass sensitivity of up to 1.315e^{11} Hz·mm^2/g. The minimum detectable mass of sensors in 978MHz is 24.3 ng/mm^2 with 0.2 MHz frequency shift which yields the mass sensitivity to 8.23e^{12} Hz·mm^2/g. The mass sensitivity is the ratio of the frequency shift Δf and mass

density ρ, which is an important parameter in evaluating the mass sensors. In the previous section, the theoretical mass sensitivities of 121MHz and 978MHz mass sensors in Table 8 are 1.32 e^{11} Hz·mm^2/g and 8.42 e^{12} Hz·mm^2/g respectively. In Equation 31 of the mass sensitivity, the frequency shift Δf is inversely proportional to the wavelength λ. The sensor in 978MHz has a smaller wavelength than the sensor in 121MHz so that it has a sharper slope of the linear region in Figure 51.

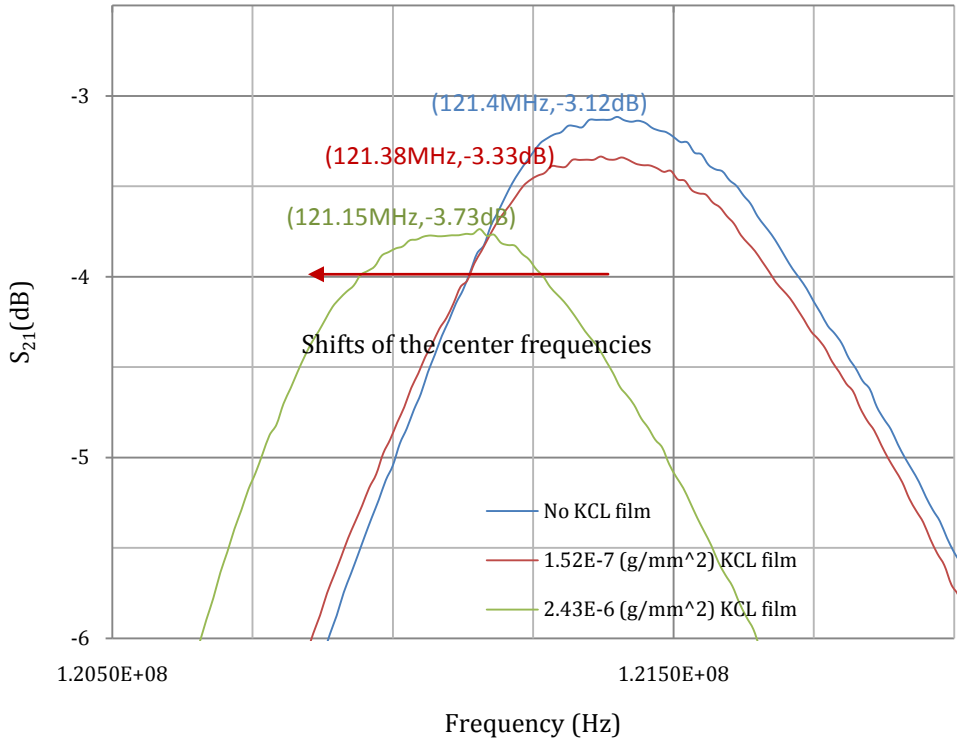

Figure 50: The 121 MHz center frequency of the dual-track SAW resonator shifts due to the KCL film on the electrodes. The center frequency decreases when the additional mass of KCL film is deposited.

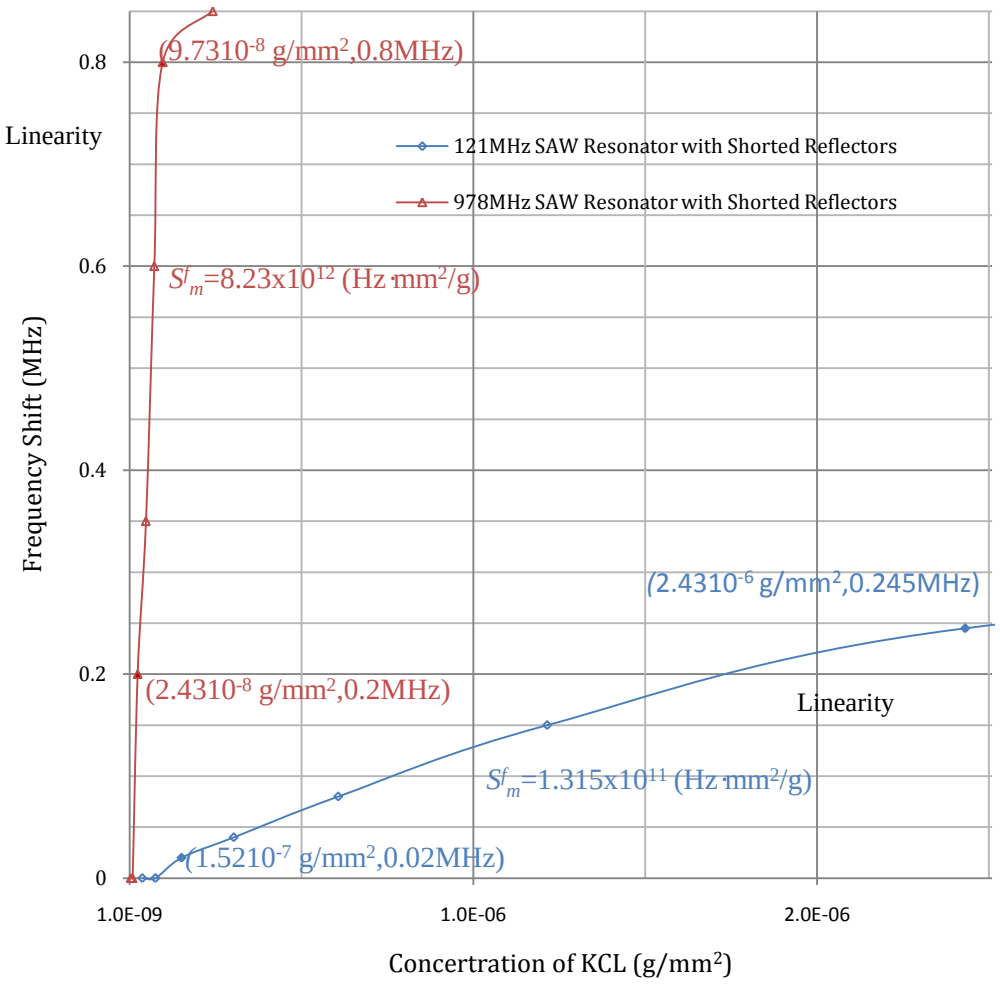

Figure 51: The frequency shifts versus the mass densities of the KCL films. According to the results of Aglient 8722D Network Analyzer, the mass sensitivities are 1.315×10^{11} Hz·mm^2/g and 8.23×10^{12} Hz·mm^2/g for 121MHz and 978 MHz SAW resonators respectively.

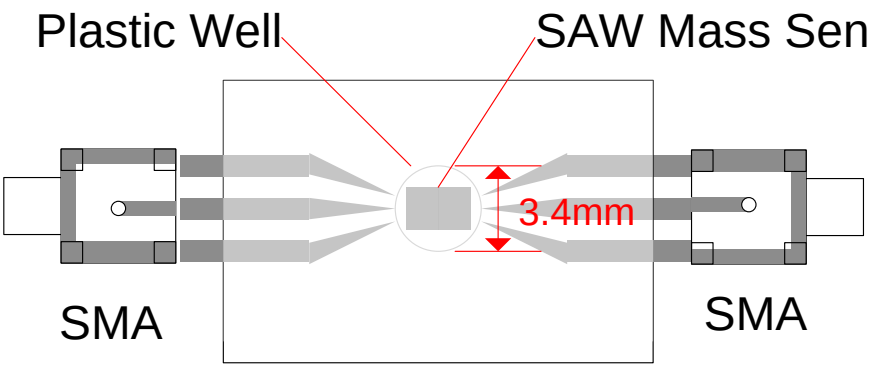

Figure 52: The illustration of a SAW mass sensor covered by a plastic well. The radius of sensing area is 3.4mm.

Figure 52 shows the configuration of the SAW mass sensor. The SAW mass sensor is covered by a 3.4mm plastic well. This plastic well gives a fixed sensing area for the KCL deposition. Figure 53 shows the structures of IDTs and KCL films. In Figure 53(a), the SAW resonator is in the center of the chip and connected directly to SMA connectors. The silver paste is put between the connectors and traces to increase the conductance. Figure 53(c) shows the KCL drops on the sensing area. The sensing area is an important factor in the measurement, which is directly proportional to the mass sensitivity. If there is a 5% difference in the area, there will be a 5% in the sensitivity. In order to measure the precise frequency shift, it is necessary to define the sensing area. In this work, the plastic well was used to define the size of the KCL drops. The diameter of the plastic well is 3.4mm which makes the sensing area A_s to 9.0746mm^2. The KCL drop fills the area of the well shown in Figure 53(c). Figure 53(d) shows the SEM picture of the KCL film and the smoothness and uniform surface of the films. The mass density of the film is 9.73

ng/mm^2 and its thickness is about 1000Å . The roughness of the KCL films is less than 100Å .

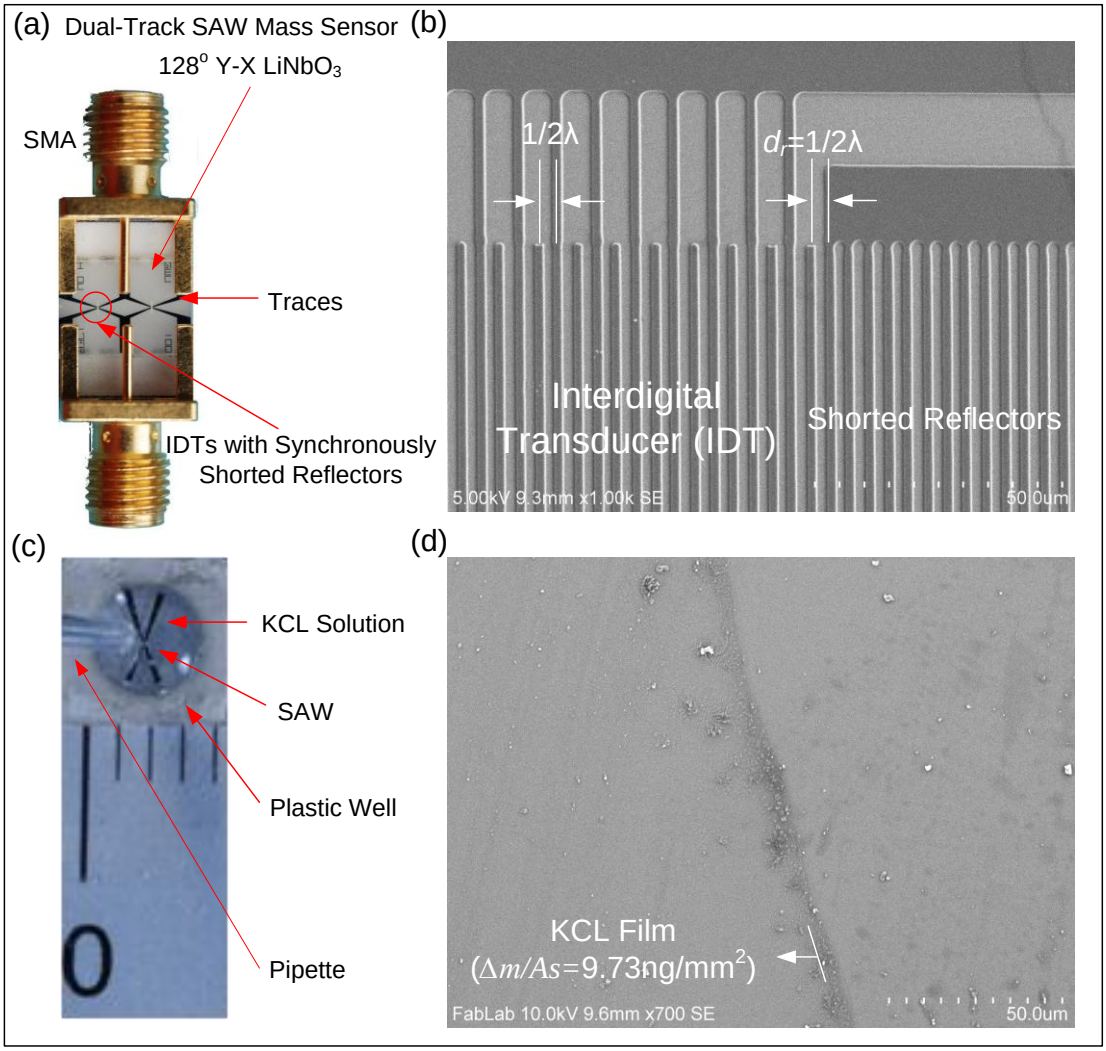

Figure 53: (a) the dual-track one-pole synchronous SAW sensor. The sensing area of the 121 MHz SAW resonator is 1.6 mm x 2.0 mm and the sensing area of the 978 MHz SAW resonator is 0.4 mm x 0.2 mm. (b) Its input and output IDTs have 12 finger pairs (N=12). The length of apertures is equal to 50λ. (c) The KCL drops on the sensing area. The plastic well is used to define the sensing area, which has a radius of 1.7mm. (d) The KCL film (mass density=9.73ng/mm^2) remained on the surface when the solvent is evaporated.

In this chapter, we used two single-pole low-loss SAW devices at 122MHz and 978MHz. According to Equation 26, the maximum linear mess densities ρ are 10.8×10^{-8} g/mm^2 and 86.4×10^{-8} g/mm^2, for 978MHz SAW mass sensors and 122MHz SAW mass sensors respectively, when h/λ is less than 0.01. Theoretical Calculation of Mass Sensitivities (S_m^f) of 121MHz and 978MHz SAW mass sensors are 1.32e^{11} Hz·mm^2/g and 8.42e^{12} Hz·mm^2/g respectively. The experimental measurement verifies the theoretical results and indicates the mass sensitivities are 1.315×10^{11} Hz·mm^2/g and 8.23×10^{12} Hz·mm^2/g, for 122MHz and 978 MHz SAW resonators respectively.

Chapter 6 - Polymer-coated SAW Mass Sensors for the Liquid-phase Environment

The SAW mass sensor has a high sensitivity and good linearity for sensing applications. In the previous chapter, the frequency shifts and mass sensitivities were examined by the additional KCL films. The additional KCL films are directly deposited on the electrodes which affects the velocity of acoustic waves. Based on the previous experimental results, the minimum detectable mass at the frequency of 121MHz SAW is 131.5 ng/mm^2. The signal shows a high sensitivity and low-loss response for sensing application. In order to use the SAW mass sensors for bio-sensing in liquid environment, it is necessary to isolate the electrodes from the molecules on the surface. This isolation can prevent the molecules to short the electrodes. In this work, the Polyvinyl Chloride (PVC) layer is used to cover the devices and isolate electrodes. Although the 121MHz SAW mass sensor is covered by PVC, it still can detect the small mass ($1.11x10^{-7}$g /mm^2) on the surface and operate in the liquid-phase environment. The 121MHz polymer-coated SAW mass sensor, with mass sensitivity is $1.037e^{11}$ Hz·mm^2/g, can be used as biosensors and operate in the liquid-phase environment. Figure 54 shows the configuration and measurement of the polymer-coated SAW mass sensor. The mass sensor is placed in center of the microscope slide. This slide is able to be placed into housing device which was designed specifically for this mass sensor and connected to the Network Analyzer. This housing device is made from PCB board and shown in Figure 57. As the measurement in the previous chapter, the standard KCL solutions, with concentration from 3×10^{-5}M to 3×10^{-3}M, are deposited into the sensing area (5.664 mm^2) to examine the frequency shifts and mass sensitivities.

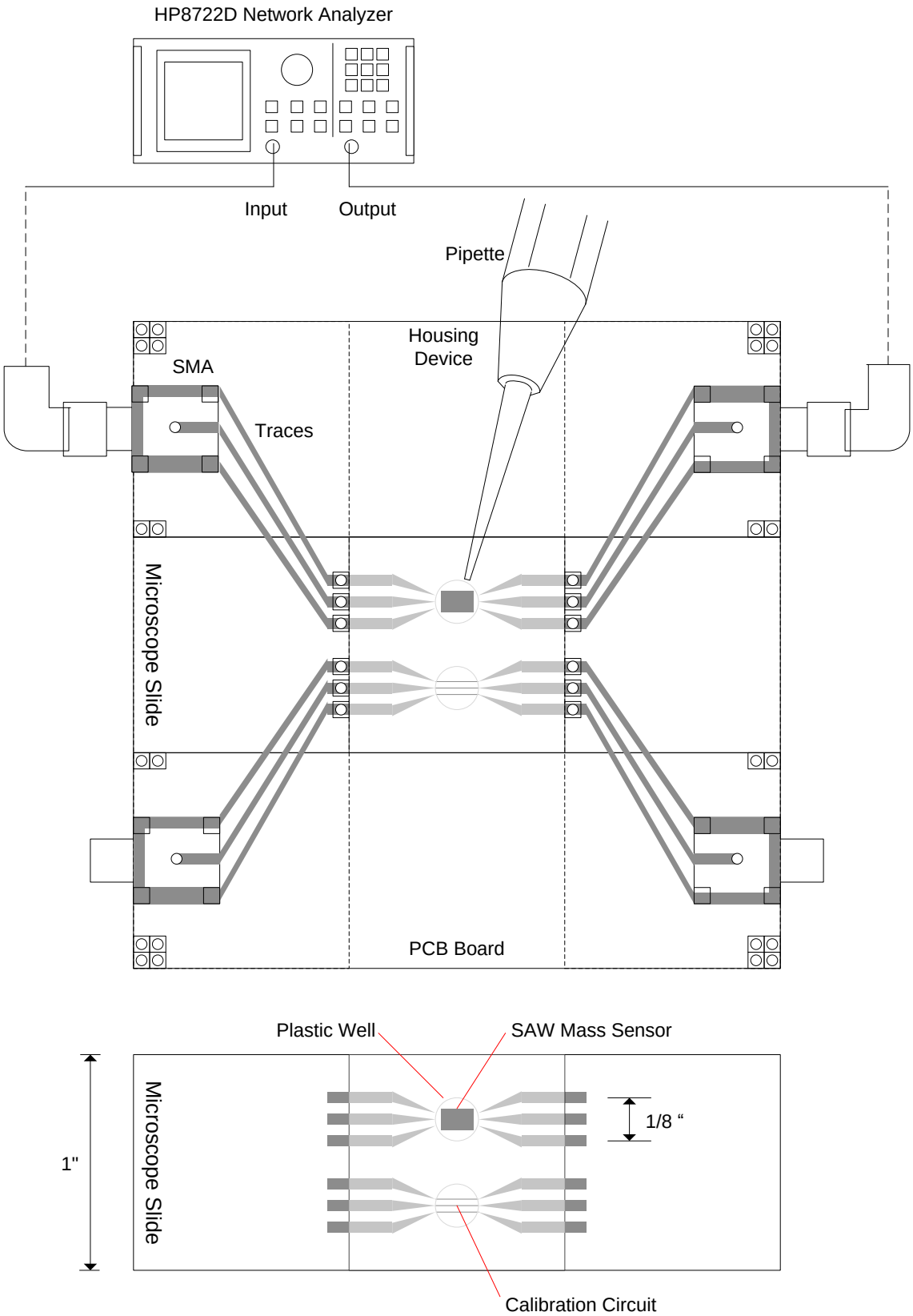
HP8722D Network Analyzer
Input
Output
Pipette
Housing
Device
SMA
Traces
Microscope Slide
PCB Board
Plastic Well
SAW Mass Sensor
1/8 “
1"
Microscope Slide
Calibration Circuit

Figure 54: The configuration of the SAW mass sensor and measurement. The plastic well is placed on the mass sensor to define the sensing area. The portable SAW mass sensor is on the microscope slide and connected to Network Analyzer by the sensor housing.

6.1. The Synthesis of the Polyvinyl Chloride Layer

Polyvinyl Chloride (PVC) is the third common plastic products. It has a chemical chain which has repeated vinyl groups and a chloride in each group. It also has advantages in cheap price, durable and easy to assemble. The PVC products include the flexible hoses, tubing, roofing, flooring membranes and electrical cable insulation. The property and molecule's structure are shown in Table 10. In this work, PVC is selected to synthesize the thin film and isolates the electrodes. In order to synthesize PVC thin film, it is necessary to use proper solvent to dissolve the PVC powers. The candidate solvent must have a low viscosity, easy evaporation and high solubility of PVC. From the previous research, Tetrahydrofuran (THF) is selected as a solvent of PVC powder. THF is water-miscible and low-viscosity organic liquid in the standard temperature and pressure. The PVC powder can be dissolved in THF easily and formed a thin film after THF solvent evaporates. The property and molecule's structure are also shown in Table 10. The chemical formula $(CH_2)_4O$ of THF has a heterocyclic compound structure. It is a useful solvent because of the polar ether and wide liquid range. The PVC powder can be easily dissolved in the THF solvent. In this work, 0.1 mg of PVC powder is dissolved in the 100 ml THF solvent which yields PVC-THF concentration to 1 g/l. The 20ml of 1g/l PVC-THF solution is dropped on the sensing area with radius is 2.38125 mm. The PVC-

THF solution is covered the whole SAW mass sensor. The PVC film is formed after THF is evaporated. The THF solvent is evaporated in 2 minutes so that the PVC film can be fabricated easily. The mass of PVC film on the surface is $1.12e^{-9}$ g/mm^2 and the thickness is about 1000Å that is measured by profilometer.

Chemistry	Property
Polyvinyl chloride (PVC) 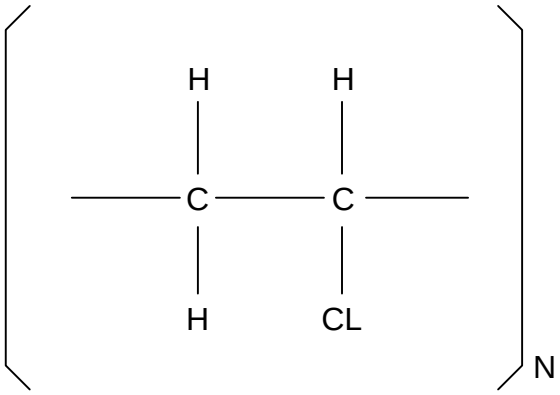 	Density 1390 kg/m3[1] Young's modulus (E) 2900-3300 MPa Tensile strength(σt) 50-80 MPa Elongation at break 20-40% Notch test 2-5 kJ/m2 Glass temperature 82 ℃[1] Melting point 100–260 ℃[1] Heat transfer coefficient (λ) 0.16 W/(m·K) Effective heat of combustion 17.95 MJ/kg Linear expansion coefficient (α) 8 10−5/K Specific heat (c) 0.9 kJ/(kg·K) Water absorption (ASTM) 0.04-0.4
Tetrahydrofuran (THF) 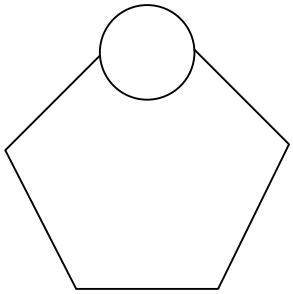	Molecular formula C_4H_8O Molar mass 72.11 g/mol Appearance colorless liquid Density 0.8892 g/cm3 (g/mL) at 20 ℃, liquid Melting point −108.4 ℃ (164.75 K) Boiling point 66 ℃ (339.15 K) Solubility in water Miscible Viscosity 0.48 cP at 25 ℃ Structure Molecular shape envelope

Table 10: The properties of Polyvinyl Chloride (PVC) and Tetrahydrofuran (THF).

To make the PVC solution, we use 0.1 g PVC powder, which molecular weight is 10000, melt in 100 ml THF solvent in room temperature. The concentration of PVC solution is equal to 1 g/L. Figure 55 shows the THF solvent and PVC solution. The PVC layer can be synthesized after THF solvent evaporates. Figure 56 shows the PVC layer under microscope, which has a relative smooth and uniform surface.

Figure 55: the THF solvent and PVC solution. The concentration of PVC solution is 1g/L.

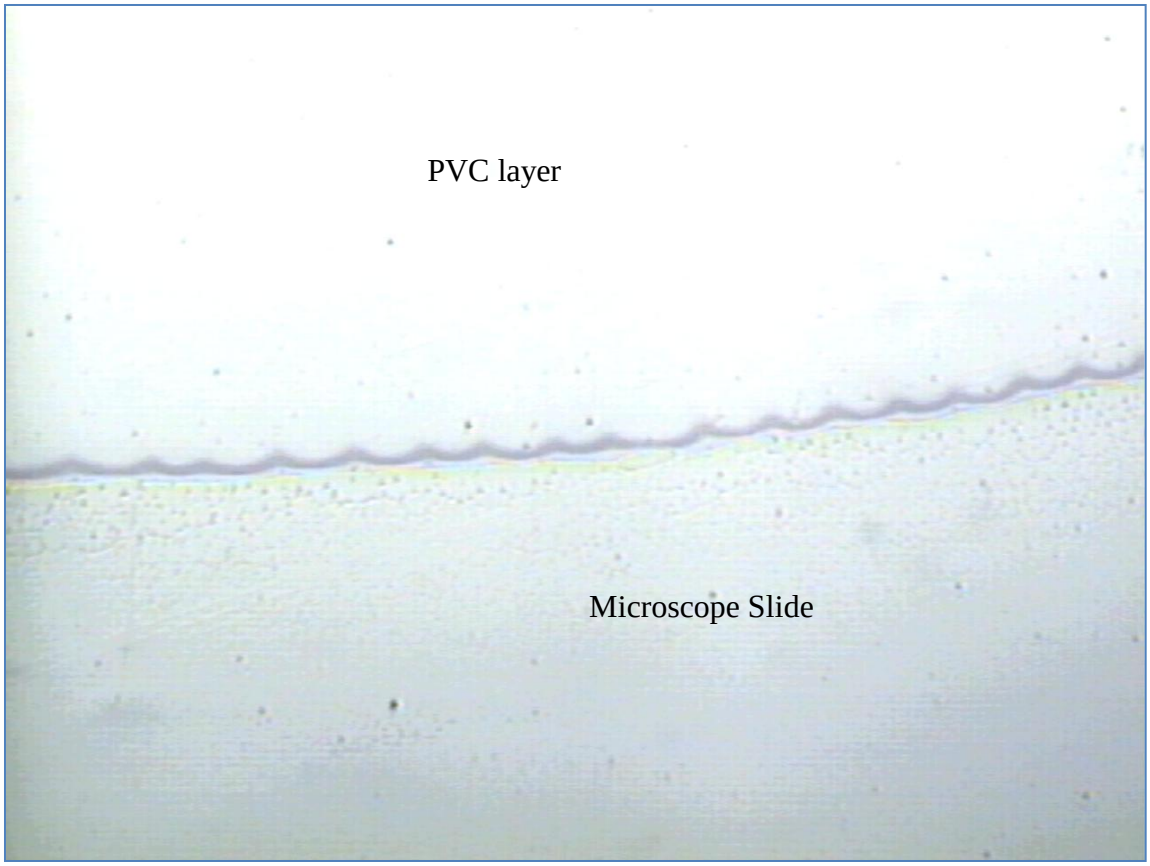

Figure 56: The PVC layer under Microscope. PVC polymer layer can be synthesized in few seconds, after THF is evaporated. It shows smooth and uniform surface under microscope.

6.2. The Velocity and Frequency shifts

Although the polymer can isolate the electrodes, the mass of polymer also cause the additional mass on the surface. Equation 33 shows the frequency shift in terms of the film-thickness ratio ($\frac{h}{\lambda}$) and velocity-shift coefficients (k_{11p}, k_{11m} and k_{11s}).When the PVC polymer is coated on the electrodes, the mass of polymer effects the amplitudes and velocity of acoustic waves as shown in Equation 34. The KCL films are also deposited on

the top of polymer to examine the mass sensitivities. The total frequency from the additional PVC polymer layer and KCL film is shown in Equation 34. The frequency shift is only varied by the mass of KCL film. The concentration of KCL film is from 3×10^{-5}M to 3×10^{-3}M. There are 18ul KCL solutions dropped into the sensing area in measurements. Equation 35 shows the frequency shifts from the variable KCL films. It also shows the linear relation between the frequency shift and total mass on the electrodes. This is important for sensing applications. The mass sensitivity of the polymer-coated SAW mass sensor can be express as Equation 36 in terms of the mass density ρ ($\rho = \frac{\Delta m}{A_S}$).

Frequency shifts due to electrodes

$$\Delta f = \frac{v}{\lambda} \times \left[k_{11p} + k_{11m} \times \left(\frac{h}{\lambda}\right) + k_{11s} \times \left(\frac{h}{\lambda}\right)^2 \right] \qquad \text{Equation 33}$$

Frequency shifts due to electrodes, polymer and KCL

$$\Delta f = \frac{v}{\lambda} \times \left[k_{11p} + k_{11m} \times \left(\left(\frac{h}{\lambda}\right) + \frac{1}{\lambda D_{Al}} \times \frac{\Delta m_{polymer+\Delta m_{KCL}}}{A_s} \right) + k_{11s} \times \left(\frac{h}{\lambda}\right)^2 \right]$$

$$= \frac{v \times k_{11p}}{\lambda} + \frac{v}{\lambda} \times \frac{k_{11m}}{\lambda D_{Al}} \times \frac{\Delta m_{polymer}}{A_S} + \frac{v}{\lambda} \times \frac{k_{11m}}{\lambda D_{Al}} \times \frac{MW_{KCL} \times M \times \Delta V}{A_S} + \frac{v \times k_{11s}}{\lambda} \times \left(\frac{h}{\lambda}\right)^2$$

$$= \frac{v \times k_{11p}}{\lambda} + \frac{v}{\lambda} \times \frac{k_{11m}}{\lambda D_{Al}} \times \frac{\Delta m_{polymer}}{A_S} + Constant + \frac{v \times k_{11s}}{\lambda} \times \left(\frac{h}{\lambda}\right)^2 \qquad \text{Equation 34}$$

If the mass of polymer layer $\Delta m_{polymer}$ is constant, the equation of frequency shifts due to additional KCL film is as following.

$$\Delta f = \frac{v}{\lambda} \times \frac{k_{11m}}{\lambda D_{Al}} \times \frac{\Delta m}{A_S} = \frac{v}{\lambda} \times \frac{k_{11m}}{\lambda D_{Al}} \times \frac{MW_{KCL} \times M \times \Delta V}{A_S} \qquad \text{Equation 35}$$

Mass sensitivity

$$S_m^f = \frac{\Delta f}{\rho} = \frac{v}{\lambda} \times \frac{k_{11m}}{\lambda D_{Al}} \quad \text{Equation 36}$$

6.3. Experimental Results

Figure 57 shows the polymer-coated SAW mass sensor and housing device. As shown in schematic, the SAW mass sensor is fabricated and placed in the center of microscope slides. It is placed into the housing device and connected to the network analyzer by SMA connectors and cables. The through circuit for calibration is also designed and placed next to the SAW mass sensor. The calibrations are performed before measurement to eliminate the mismatch from cables and housing device. The plastic well, as shown in Figure 57 and 58, is used to define the sensing area. The sensing area includes the input/output IDTs and reflectors.

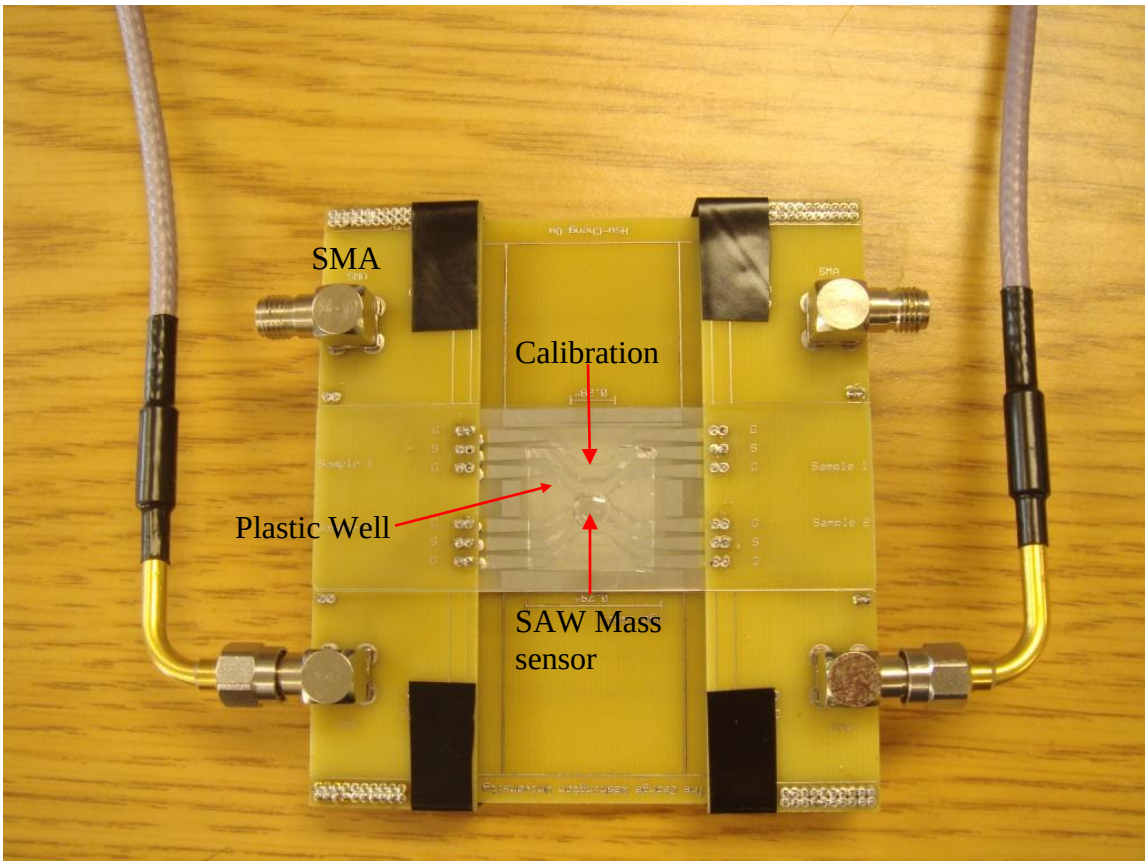

Figure 57: The polymer-coated SAW mass sensor and sensor housing device.

The plastic wells, made by the 3M fabric cubicle Grip, are able to adhere on the mass sensors. This plastic well has a 3/16" diameter circle and sensing area is 17.814 mm^2. After putting the plastic well on the surface, 20ml of 1g/l PVC-THF solution is dropped in the well to deposit PVC thin film. The PVC thin film can be formed after the THF evaporates. This process is usually less than 2 minutes. Figure 58 shows the 3/16" plastic well on the SAW mass sensor. The mass sensor is also covered with PVC film to isolate electrodes and liquid. In order to examine the mass sensitivity, The KCL solution is used to deposit a KCL thin film on the PVC layer. Figure 58 shows the 18ul KCL solution in the plastic well. As the same measurement in the previous chapter, different

concentrations of KCL solutions are deposited on the surface to examine the frequency shifts. The KCL film remains on the top of PVC layer after the water evaporates. This process takes 30 minutes to dry the KCL solution.

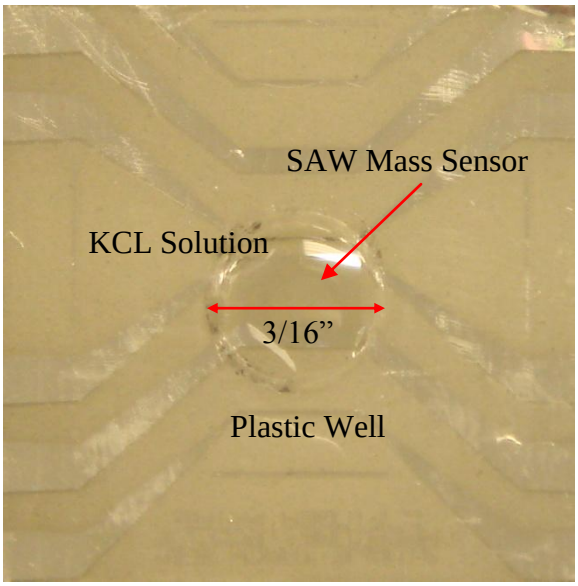

Figure 58: The 3/16” plastic well on the 121MHz SAW mass sensor. The 18ul KCL solution is dropped into the well and covered with the whole sensor. The KCL remains on the surface of the polymer layer after the solvent evaporates.

Figure 59 shows the mass sensitivities of 121MHz SAW mass sensor. The mass sensitivity of SAW mass sensors without PVC layers is $1.315e^{11}$ (Hz·mm^2/g) and the minimum detectable mass is $1.52e^{-7}$ g. The theoretical sensitivity of 121MHz SAW sensor is $1.32e^{11}$ (Hz·mm^2/g). According to Figure 59, the experimental result matches the theoretical model and the error is 3.78%. The mass sensitivity of polymer-coated SAW mass sensors is $1.037e^{11}$ (Hz·mm^2/g) and the minimum detectable mass is $1.11e^{-7}$ g. Besides, the frequency shifts of polymer-coated SAW mass sensors are less than SAW

mass sensors without polymer. Although the PVC layer causes the less sensitivity and frequency shifts, the advantage is to be able to sense bimedical material in the liquid enviroment.

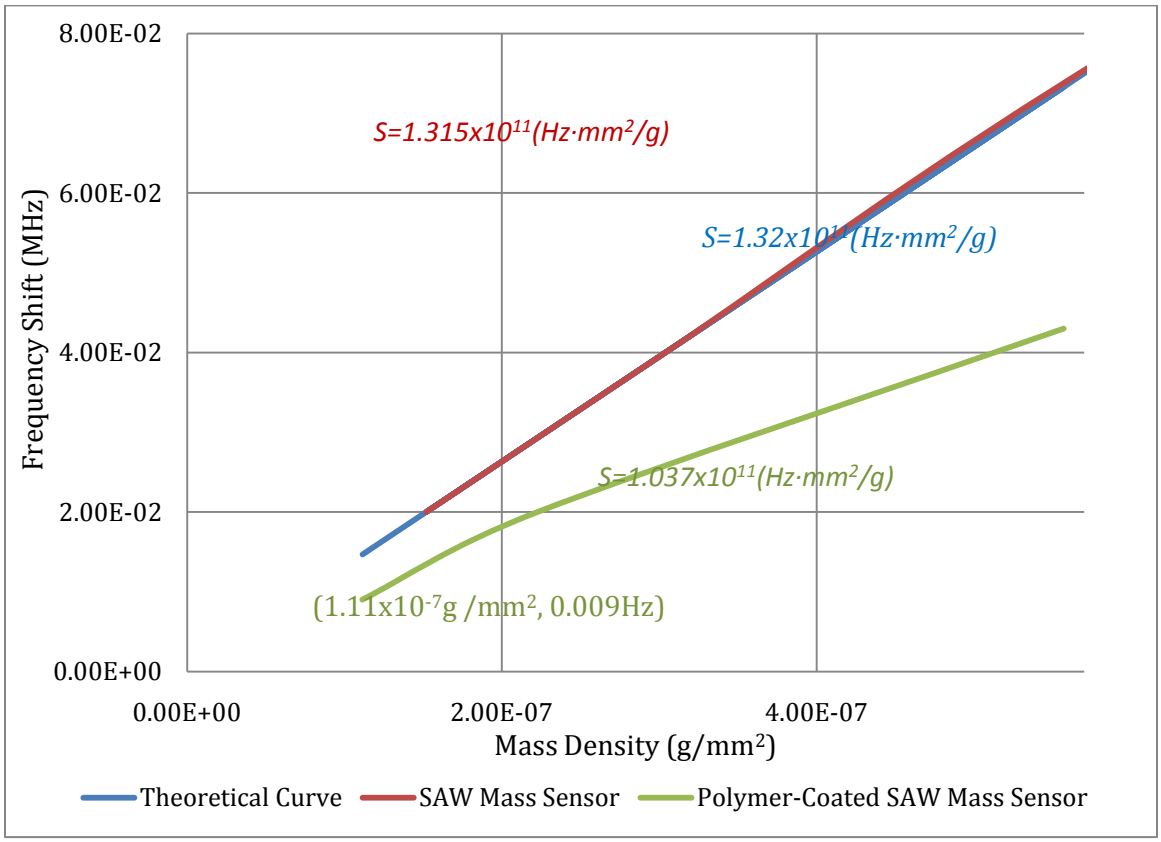

Figure 59: The mass sensitivity of SAW Mass Sensors. The 121MHz polymer-coated SAW mass sensor has slightly less sensitivity than the SAW mass sensor.

Chapter 7 - Conclusion and Future Research Opportunity

7.1. Conclusion

There are three objectives studied in this work: (1) Develop a synchronous low-loss one-pole SAW resonator (2) Use the SAW resonator as a mass sensor to sense the additional mass on the surface (3) Improve the SAW mass sensor in the liquid by coating polymer on the surface. These three objectives are shown by developing the equivalent circuit/equations, FEM simulation, fabrication and measurement. The accomplishments of this work can be summarized as following: (1) improve the SAW insertion loss and obtain the higher Q factor (2) design a one-pole response for sensing applications (3) develop high sensitive mass sensors (4) use a polymer layer in liquid phase to detect the mass. In this work, the synchronous low-loss one-pole SAW resonator and polymer-coated SAW mass sensor are designed and fabricated to achieve these three goals.

The first objective in this work is to develop a synchronous low-loss one-pole SAW resonator on the 128^{o} YX $LiNbO_3$ piezoelectric substrate. In order to achieve the low loss response, the reflectors are designed and fabricated synchronously next to input and output IDTs. These reflectors limit the acoustic waves propagating between input and output IDTs, which also limit the energy transfer between IDTs. The geometries of IDT structures are described in the Chapter 3. A resonance due to the synchronous reflectors is superimposed in the center frequency. This superimposed resonance not only increase insertion loss but also increase the Q factor in the frequency response. In this work, there are two synchronous low-loss one-pole SAW resonators fabricated on the 128^{o} YX $LiNbO_3$ substrate. The 121MHz SAW resonator has a 121MHz center frequency and -

3.1dB insertion loss in the frequency response. The Q factor is improved up to 192.4 in comparison with the bidirectional SAW resonator. SAW resonators at frequency of 978MHz center frequency and -2.8dB insertion loss was designed. The fabrication processes and measurement steps are described in Chapter 4.

The second objective is to use synchronous low-loss one-pole SAW resonators as mass sensors. The synchronous low-loss one-pole SAW resonators, or SAW mass sensors, have many advantages for sensing application in comparison with bidirectional SAW mass sensor. They can be summarized in following points: (a) It has one-pole S21 response which has the maximum insertion loss in the center frequency. (b) It has high IL so that it doesn't need the amplifiers or attenuators. (c) It has smaller size than delay line SAW sensor because there is no quadrate sensing area between input and output IDTs. The molecules are placed on the electrodes directly, which causes the velocity and center frequency of acoustic waves decrease. The details are described in Chapter 5, including of theoretical equations, simulations, fabrication and measurement. In this work, there are two mass sensors which were designed at 121MHz and 978MHz. The minimum detectable mass of sensors in 121MHz is 152.1 ng/mm^2 with 0.02 MHz frequency shift which yields the mass sensitivity to 1.315e^{11} Hz·mm^2/g. The minimum detectable mass of sensors in 978MHz is 24.3 ng/mm^2 with 0.2 MHz frequency shift which yields the mass sensitivity to 8.23e^{12} Hz·mm^2/g. the mass sensitivities of 121MHz and 978MHz mass sensors in are 1.32 e^{11} Hz·mm^2/g and 8.42 e^{12} Hz·mm^2/g respectively. According to experimental results, the SAW mass sensor has good linearity and high sensitivity for sensing applications.

The third objective is to develop a polymer-coated SAW mass sensor for liquid environment. Although the mass sensor has good sensitivity, the applications for SAW mass sensors are limited due to the direct deposition on the electrodes. The molecules on the sensing area must be in a dry and nonconductive condition. In order to use the SAW mass sensors for biosensors, it is necessary to isolate the electrodes from the molecules on the surface. This isolation is important to prevent molecules from shorting the electrodes. A novel PVC layer is used to cover the devices and isolate the electrodes. Although the SAW mass sensor is covered by PVC, it still can detect the small mass on the surface and operate in the liquid-phase environment. The mass on the PVC layer still affects velocity and center frequency of acoustic waves. This polymer-coated SAW mass sensor can be used as biosensors and operate in the liquid-phase environment. The mass sensitivity of 121MHz SAW mass sensors without PVC layers is $1.315e^{11}$ (Hz·mm^2/g) and the minimum detectable mass is $1.52e^{-7}$ g. The theoretical sensitivity of 121MHz SAW sensor is $1.32e^{11}$ (Hz·mm^2/g). The experimental result matches the theoretical model and the error is 3.78%. The mass sensitivity of polymer-coated SAW mass sensors is $1.037e^{11}$ (Hz·mm^2/g) and the minimum detectable mass is $1.11e^{-7}$ g.

7.2. Future Research Opportunity

The future work is to develop the polymer-coated SAW mass sensors as the biosensor. The steps of polymer-coated SAW mass sensors for biomedical applications are illustrated in Figure 60. The electrodes covered by polymer are isolated from the liquid environment. The polymer can prevent the signals on the electrodes to be shorted.

The plastic well is used to define the sensing area and hold the samples. The acoustic waves propagate between the polymer layer and $LiNbO_3$ substrate. The antibodies are attached on the surface of polymer and used to catch antigens. In Figure 60(b), it shows a complete antibody-antigen reaction on the polymer layer. Table 11 shows that the smaller feature size of SAW mass sensor can have higher frequency shifts when 20 pg/mm^2 mass is on the electrodes. We can design the nano-scale SAW (λ=40) device which will have high sensitivity (0.11fg/Hz) and be able to detect small mass (20 pg/mm^2).

Width of electrodes (nm)	Wavelength λ (nm)	Center frequency (GHz)	frequency shift Δf (KHz)	volectiy shift Δv (m/s)
10	40	99.925	171.424078	0.00598376
20	80	49.9625	42.8560195	0.00299188
30	120	33.30833333	19.04711978	0.001994587
40	160	24.98125	10.71400488	0.00149594
50	200	19.985	6.85696312	0.001196752
60	240	16.65416667	4.761779945	0.000997293
70	280	14.275	3.498450572	0.000854823
80	320	12.490625	2.678501219	0.00074797
90	360	11.10277778	2.116346642	0.000664862
100	400	9.9925	1.71424078	0.000598376
110	440	9.084090909	1.416727917	0.000543978
120	480	8.327083333	1.190444986	0.000498647
130	520	7.686538462	1.014343657	0.000460289

Table 11: The frequency shifts when 20 pg/mm^2 mass is on the electrodes. The smaller width of electrodes yields to the higher frequency shift and mass sensitivity.

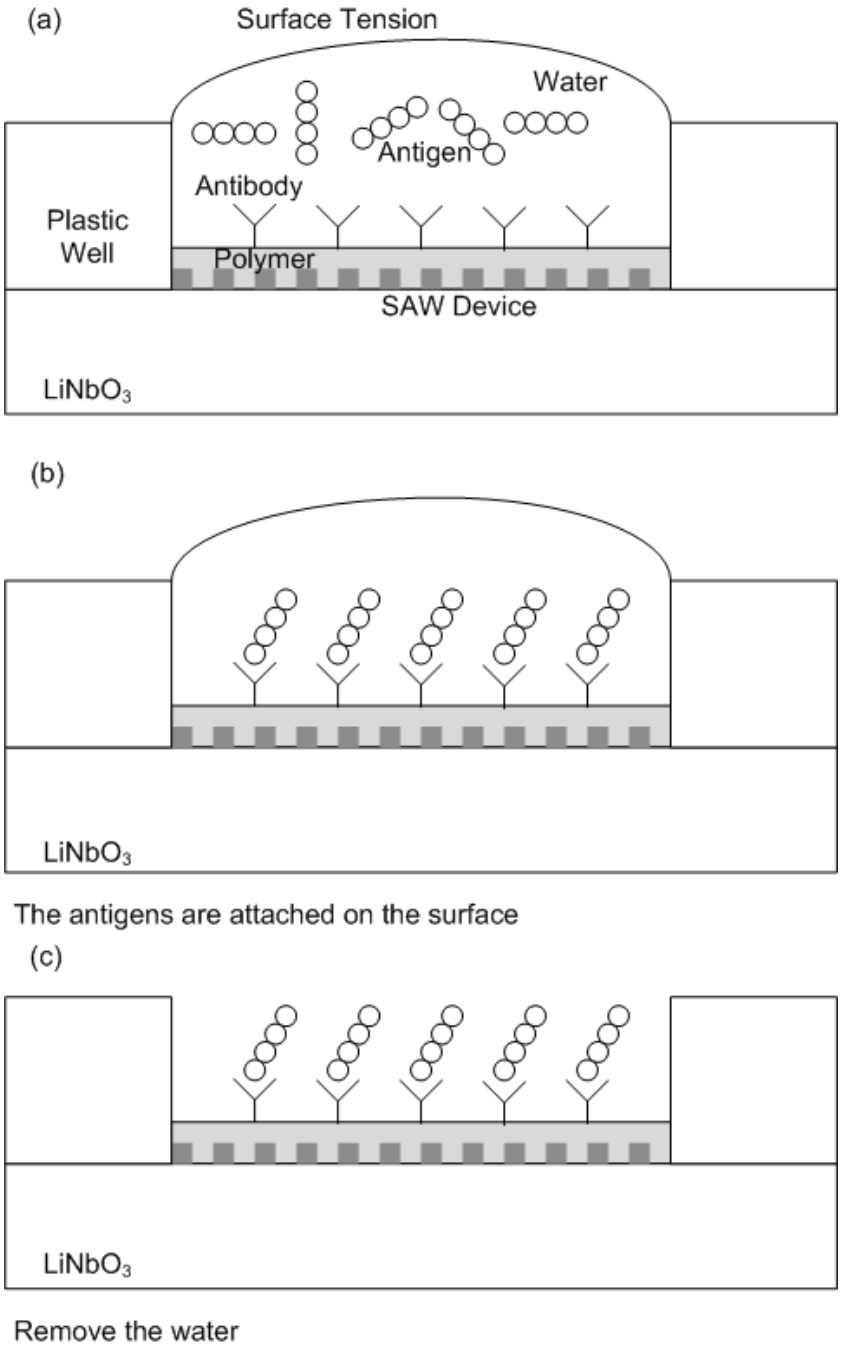

Figure 60: The illustration of the antibody-antigen reactions on the polymer-coated SAW mass sensor. The polymer layer can prevent the short circuit of electrodes in the liquid-phase environment. The antibodies are attached on the surface of polymer to catch the antigen.

References

[1] C. K. Campbell, “Surface acoustic wave devices,” in *Mobile and Wireless Communications*. New York: Academic, 1998. pp. 231-237

[2] K.K Wong, Properties of Lithium Niobate, United Kingdom: INSPEC, pp.58-103, 2002

[3] Campbell, C.K.; , "Applications of surface acoustic and shallow bulk acoustic wave devices," *Proceedings of the IEEE* , vol.77, no.10, pp.1453-1484, Oct 1989

[4] Asai, K.; Isobe, I.; Tada, T.; Hikita, M.; , "SAW timing-extraction filter and investigation of submicron process technology for Gb/s optical communications system," *Ultrasonics Symposium, 1995. Proceedings., 1995 IEEE* , vol.1, no., pp.131-135 vol.1, 7-10 Nov 1995

[5] Saw, J.; Suthers, M.; Dai, J.; Xu, Y.; Leroux, R.; Nisbet, J.; Rabjohn, G.; Chen, Z.; , "SAW technology in RF multichip modules for cellular systems," *Ultrasonics Symposium, 1995. Proceedings., 1995 IEEE* , vol.1, no., pp.171-175 vol.1, 7-10 Nov 1995

[6] Williamson, R.C.; , "Case Studies of Successful Surface-Acoustic-Wave Devices," *Ultrasonics Symposium, 1977* , vol., no., pp. 460- 468, 1977

[7] Yatsuda, H.; Horishima, T.; Eimura, T.; Ooiwa, T.; , "Miniaturized SAW filters using a flip-chip technique," *Ultrasonics Symposium, 1994. Proceedings., 1994 IEEE* , vol.1, no., pp.159-162 vol.1, 1-4 Nov 1994

[8] Ruppel, C.C.W.; Dill, R.; Fischerauer, A.; Fischerauer, G.; Gawlik, A.; Machui, J.; Muller, F.; Reindl, L.; Ruile, W.; Scholl, G.; Schropp, I.; Wagner, K.C.; , "SAW devices for consumer communication applications," *Ultrasonics,*

Ferroelectrics and Frequency Control, IEEE Transactions on , vol.40, no.5, pp.438-452, Sep 1993

[9] Yamamoto, Y.; Kajihara, R.; , "SAW composite longitudinal mode resonator (CLMR) filters and their application to new synthesized resonator filters," *Ultrasonics Symposium, 1993. Proceedings., IEEE 1993* , vol., no., pp.47-51 vol.1, 31 Oct-3 Nov 1993

[10] Hays, R.M.; Hartmann, C.S.; , "Surface-acoustic-wave devices for communications," *Proceedings of the IEEE* , vol.64, no.5, pp. 652- 671, May 1976

[11] Padgett, J.E.; Gunther, C.G.; Hattori, T.; , "Overview of wireless personal communications," *Communications Magazine, IEEE* , vol.33, no.1, pp.28-41, Jan 1995

[12] Machui, J.; Bauregger, J.; Riha, G.; Schropp, I.; , "SAW devices in cellular and cordless phones," *Ultrasonics Symposium, 1995. Proceedings., 1995 IEEE* , vol.1, no., pp.121-130 vol.1, 7-10 Nov 1995

[13] Wakino, K.; Nishikawa, T.; Matsumoto, H.; Ishikawa, Y.; , "Quarter Wave Dielectric Transmission Line Diplexer for Land Mobile Communications," *Microwave Symposium Digest, MTT-S International* , vol.79, no.1, pp. 278- 280, Apr 1979

[14] Campbell, C.K.; , "Applications of surface acoustic and shallow bulk acoustic wave devices," *Proceedings of the IEEE* , vol.77, no.10, pp.1453-1484, Oct 1989

[15] Tancrell, R.H.; Holland, M.G.; , "Acoustic surface wave filters," *Proceedings of the IEEE* , vol.59, no.3, pp. 393- 409, March 1971

[16] Smith, W.R.; Gerard, H.M.; Collins, J.H.; Reeder, T.M.; Shaw, H.J.; , "Analysis of Interdigital Surface Wave Transducers by Use of an Equivalent Circuit Model," *Microwave Theory and Techniques, IEEE Transactions on* , vol.17, no.11, pp. 856- 864, Nov 1969

[17] Smith, W.R.; Gerard, H.M.; Collins, J.H.; Reeder, T.M.; Shaw, H.J.; , "Design of Surface Wave Delay Lines with Interdigital Transducers," *Microwave Theory and Techniques, IEEE Transactions on* , vol.17, no.11, pp. 865- 873, Nov 1969

[18] Hartmann, C.S., Jr.; Bell, D.T.; Rosenfeld, R.C.; , "Impulse Model Design of Acoustic Surface-Wave Filters," *Microwave Theory and Techniques, IEEE Transactions on* , vol.21, no.4, pp. 162- 175, Apr 1973

[19] Campbell, C.K.; , "Longitudinal-mode leaky SAW resonator filters on 64° Y-X lithium niobate," *Ultrasonics, Ferroelectrics and Frequency Control, IEEE Transactions on* , vol.42, no.5, pp.883-888, Sep 1995

[20] Yamanouchi, K.; Takeuchi, M.; , "Applications for piezoelectric leaky surface waves," *Ultrasonics Symposium, 1990. Proceedings., IEEE 1990* , vol., no., pp.11-18 vol.1, 4-7 Dec 1990

[21] Isobe, A.; Hikita, M.; Asai, K.; , "Large k^2 and good temperature stability for SAW on new double-rotated cut of α-quartz with gold film," *Ultrasonics Symposium, 1993. Proceedings., IEEE 1993* , vol., no., pp.323-326 vol.1, 31 Oct-3 Nov 1993

[22] Hashimoto, K.Y.; Yamaguchi, M.; Kogo, H.; , "Experimental Verification of SSBW and Leaky SAW Propagating on Rotated Y-Cuts of LiNbO3and LiTaO3," *1983 Ultrasonics Symposium* , vol., no., pp. 345- 349, 1983

[23] Campbell, C.K.; Saw, C.B.; , "Analysis and Design of Low-Loss SAW Filters Using Single-Phase Unidirectional Transducers," *Ultrasonics, Ferroelectrics and Frequency Control, IEEE Transactions on* , vol.34, no.3, pp. 357- 367, May 1987

[24] Saw, C.B.; Campbell, C.K.; , "Improved Design of Single-Phase Unidirectional Transducers for Low-Loss SAW Filters," *IEEE 1987 Ultrasonics Symposium* , vol., no., pp. 169- 172, 1987

[25] Campbell, C.K.; Smith, P.M.; Edmonson, P.J.; , "Aspects of modeling the frequency response of a two-port waveguide-coupled SAW resonator-filter," *Ultrasonics, Ferroelectrics and Frequency Control, IEEE Transactions on* , vol.39, no.6, pp.768-773, Nov 1992

[26] Hartmann, C.S.; Wright, P.V.; Kansy, R.J.; Garber, E.M.; , "An Analysis of SAW Interdigital Transducers with Internal Reflections and the Application to the Design of Single-Phase Unidirectional Transducers," *1982 Ultrasonics Symposium* , vol., no., pp. 40- 45, 1982

[27] Flory, C.; Tan, M.; , "Diffraction minimization in SAW devices using wide aperture compensation," *Ultrasonics, Ferroelectrics and Frequency Control, IEEE Transactions on* , vol.35, no.4, pp.498-502, Jul 1988

[28] Hartmann, C.S.; Abbott, B.P.; , "Overview of design challenges for single phase unidirectional SAW filters," *Ultrasonics Symposium, 1989. Proceedings., IEEE 1989* , vol., no., pp.79-89 vol.1, 3-6 Oct 1989

[29] Lehtonen, S.; Plessky, V.P.; Hartmann, C.S.; Salomaa, M.M.; , "Unidirectional SAW transducer for GHz frequencies," *Ultrasonics, 2003 IEEE Symposium on* , vol.1, no., pp. 817- 820 Vol.1, 5-8 Oct. 2003

[30] Lehtonen, S.; Plessky, V.P.; Hartmann, C.S.; Salomaa, M.M.; , "Unidirectional SAW transducer for gigahertz frequencies," *Ultrasonics, Ferroelectrics and Frequency Control, IEEE Transactions on* , vol.50, no.11, pp. 1404- 1406, Nov 2003

[31] P.M. Naraine; C.K. Campbell; , "Gigahertz SAW Filters on YZ-Lithium Niobate Without the Use of Sub-Micron Line Widths," *IEEE 1984 Ultrasonics Symposium* , vol., no., pp.93-96, 1984

[32] Dong-Pei Chen; Haus, H.A.; , "Analysis of Metal-Strip SAW Gratings and Transducers," *Sonics and Ultrasonics, IEEE Transactions on* , vol.32, no.3, pp. 395- 408, May 1985

[33] Campbell, C.K.; , "Scattering and transmission matrix analysis of SAW resonator filters with long-pair IDTs and triple composite longitudinal modes on quartz," *Ultrasonics Symposium, 1994. Proceedings., 1994 IEEE* , vol.1, no., pp.309-312 vol.1, 1-4 Nov 1994

[34] Paige, E.G.S.; Stove, A.G.; Woods, R.C.; , "SAW Reflection from Aluminium Strips on LiNbO3," *1981 Ultrasonics Symposium* , vol., no., pp. 144- 147, 1981

[35] Dong-Pei Chen; Haus, H.A.; , "Analysis of Metal-Strip SAW Gratings and Transducers," *Sonics and Ultrasonics, IEEE Transactions on* , vol.32, no.3, pp. 395- 408, May 1985

[36] Cross, P.S.; Shreve, W.R.; Tun Sein Tan; , "Synchronous IDT SAW Resonators with Q Above 10,000," *1979 Ultrasonics Symposium* , vol., no., pp. 824- 829, 1979

[37] Campbell, C.K.; , "Narrow-Band Filter Design Using a Staggered Multimode SAW Resonator," *Sonics and Ultrasonics, IEEE Transactions on* , vol.32, no.1, pp. 65- 70, Jan 1985

[38] Campbell, C.K.; Saw, C.B.; , "Analysis and Design of Low-Loss SAW Filters Using Single-Phase Unidirectional Transducers," *Ultrasonics, Ferroelectrics and Frequency Control, IEEE Transactions on* , vol.34, no.3, pp. 357- 367, May 1987

[39] Hietala, S.L.; Hietala, V.M.; Brinker, C.J., "Dual SAW sensor technique for determining mass and modulus changes ," *Ultrasonics, Ferroelectrics and Frequency Control, IEEE Transactions on* , vol.48, no.1, pp.262-267, Jan 2001

[40] Bender, F.; Dahint, R.; Josse, F., "Acoustic wave-based sensors using mode conversion in periodic gratings," *Ultrasonics, Ferroelectrics and Frequency Control, IEEE Transactions on* , vol.46, no.6, pp.1497-1503, Nov 1999

[41] Zheng Zhang; Dazhong Zhu; Zhelong Huang, "A mass-loading effect $LiNbO_3$ SAW sensor," *Solid-State and Integrated-Circuit Technology, 2001. Proceedings. 6th International Conference on* , vol.2, no., pp. 781-784 vol.2, 22-25 Oct. 2001

[42] Nomura, T.; Saitoh, A.; Koyama, K., "Mass Flow Sensor Using Dual SAW Device," *Frequency Control Symposium, 2007 Joint with the 21st European Frequency and Time Forum. IEEE International* , vol., no., pp.25-30, May 29 2007-June 1 2007

[43] Xu, J.; Hu, G.; Auner, G.W.; Ying, H., "Mass sensitivity of dual mode SAW delay lines on AlN/sapphire structure," *Electronics Letters* , vol.41, no.22, pp. 1254-1255, 27 Oct. 2005